Mineralogical characterisation, fluid inclusions and formation conditions of aplite, pegmatite and quartz-tourmaline rich veins, Elba (Italy).

MASTER THESIS

Montanuniversitaet Leoben
Department of Applied Geosciences and Geophysics
Chair of Resource Mineralogy

Sebastian E. Schilli, BSc.

Advisor: Bakker, Ronald J., Ao.Univ.-Prof. Dr.

Leoben, February 2015

AFFIDAVIT

I declare in lieu of oath, that I wrote this thesis and performed the associated research myself, using only literature cited in this volume.

Date

Signature

Acknowledgments

First of all, I would like to thank my advisor, Prof. Ronald J. Bakker, for the great scientific support as well as the guidance throughout my master thesis. Furthermore, I would like to express my sincerest gratitude to Dr. Federica Zaccarini for her brilliant scientific support and her encouragement.

Many thanks also go to Helmut Mühlhans for sample preparation, to Judith Bergthaler for bureaucratic work and also to the whole Chair of Resource Mineralogy for their support.

Last but not least, I want to thank my parents and my brother for their love, their financial aid and great support throughout this part of my life. I also want to thank all my good friends I have met here in Leoben!

> “Geology gave us the immensity of time and taught us how little of it
> our own species has occupied.”
>
> — Stephen Jay Gould, *Ever Since Darwin: Reflections on Natural History*

Index of contents

Abstract 5

Kurzfassung 7

1. Introduction and motivation 9

  1.1. Introduction 9

  1.2. Scope of work 9

  1.3. Geographical setting 10

2. Geologic and Tectonic Setting 11

  2.1. Regional geology 11

  2.2. Tectonic complexes of Elba Island 14

3. The Late Miocene magmatic evolution 19

4. Pegmatites 24

  4.1. An Introduction to Pegmatites 24

  4.2. The pegmatites of Elba Island 26

5. Field Data 29

  5.1. Eastern part of Monte Capanne 29

  5.2. North-eastern part of Monte Capanne 31

  5.3. Western part of Monte Capanne 32

  5.4. Mt. Calamita Formation 33

6. Petrography and mineral chemistry 36

  6.1. Basic principles of the used methods 36

    6.1.1. Raman Spectroscopy 36

    6.1.2. Microthermometry 38

    6.1.3. Electron microprobe analyser (EPMA) 39

  6.2. Results and description of the petrography and mineral chemistry 41

    6.2.1. Sample 57 A 42

    6.2.2. Sample 59 B 44

    6.2.3. Sample 60 A 47

    6.2.4. Sample 64 A 48

    6.2.5. Sample 65 C 50

    6.2.6. Sample 67 E 51

    6.2.7. Sample 72 C 52

    6.2.8. Sample 75 D 54

    6.2.9. Sample 85 A 56

- 6.2.10. Sample 0 A ... 57
- 6.2.11. Sample 1 J ... 60
- 6.2.12. Sample 3 A ... 62
- 6.2.13. Sample 5 B ... 64
- 6.2.14. Sample 9 C ... 65
- 6.2.15. Sample 15 A ... 68
- 6.2.16. Sample 17 A ... 70
- 6.2.17. Sample 23 F ... 71
- 6.2.18. Sample 25 A ... 73
- 6.2.19. Sample 29 D ... 76
- 6.2.20. Sample 35 B ... 78

6.3. Fluid Inclusion Research ... 81
- 6.3.1. Sample 67E – QTZ3 ... 81
- 6.3.2. Sample 85A – QTZ1 ... 85
- 6.3.3. Sample 85A – QTZ2 ... 86
- 6.3.4. Sample 85A – TUR1 ... 88
- 6.3.5. Example of the combination of Raman spectroscopy and microthermometry ... 90

7. Discussion and conclusions ... 92
- 7.1. Tourmaline analyses ... 92
- 7.2. Geothermometry with garnet and biotite ... 96
- 7.3. Cordierite analyses ... 98
- 7.4. Andalusite analyses ... 99
- 7.5. Oxide analyses ... 99
- 7.6. Nb-Ta oxide analyses ... 100
- 7.7. Discussion of the results of the fluid inclusion research ... 102

8. References ... 104

9. Appendix ... 108

Abstract

Aplitic-pegmatitic veins, usually present as dykes, sills and irregular shaped bodies were investigated around the Monte Capanne Pluton and the Calamita peninsula (Elba, Italy). These veins consist of aplitic-pegmatitic bodies in the eastern part and a porphyric dyke (Orano porphyry) in the western part of the Monte Capanne Pluton.

Samples were collected in the field to determine the local geological context of these veins by describing in detail the relationship between host rock and veins.

Thin sections were prepared from these samples to investigate the mineralogy and textures in detail. In addition, several thick sections (about 100 µm thickness) were prepared for fluid inclusion research. Both minerals and fluid inclusions were analysed by optical microscopy, Raman spectroscopy, electron microprobe analyses and microthermometry.

The aplitic/pegmatitic veins consist mainly of quartz, plagioclase, K-feldspar with abundant immiscibility features, and locally mica, tourmaline and andalusite. The porphyry contains phenocrysts (up to 8 mm in size) of plagioclase, biotite and anhedric rounded quartz grains within a fine-grained matrix. Accessory minerals in the aplitic/pegmatitic veins are zircon, xenotime, monazite, rutile/brookite/anatase, apatite, garnet, cordierite, allanite, titanite, columbite, cassiterite, hematite, magnetite, biotite, hedenbergite, sillimanite and pyrite. Tourmaline and andalusite crystals are brittly deformed (boudins) due to magmatic flow.

Tourmaline is strongly zoned, which is visualized by green, brown, blue and colourless pleochroic colours under the optical microscope with transmitted light. The composition ranges from schorlitic to foitic tourmaline and dravitic tourmaline in pegmatites around the Monte Capanne Pluton. The colourless tourmaline of the schorlitic group is a Mn-rich elbaitic tourmaline. At the Calamita peninsula, the tourmalines display two compositional groups of schorlitic and dravitic tourmaline. The pink colour of andalusite is directly related to the Fe-content (up to 2.9 mass% FeO). The Mg/Fe ratio of coexisting garnet and biotite (sample 57A) were used to estimate a temperature of approximately 600 ˚C. Rutile contains up to 7.0 mass% Nb_2O_5, 4.3 mass% SnO_2, 3.9 mass% Ta_2O_5 and 11.5 mass % FeO. Columbite contains 48.0-56.1 mass% Nb_2O_5, 9.3-15.7 mass% Ta_2O_5, 11.9-16.3 mass% FeO, 7.9-11.7 mass% WO_3 and 0.4-5.0 mass% Sc_2O_3. Some columbites are extremely enriched in HREE (heavy rare earth elements), and contain additionally up to 22 mass% Y_2O_3 and 11.8 mass% UO_2.

The aplitic/pegmatitic veins contain abundant fluid inclusions of primary origin. The inclusions occur mainly in quartz, but tourmaline, andalusite, plagioclase, allanite and garnet also contain large fluid inclusions. Quartz in pegmatites in the ophiolitic unit at the eastern border of the Monte Capanne Pluton contains large inclusions (up to 20 µm in diameter) with approximately 42 vol% vapour phase. This phase is a mixture of CO_2 and CH_4 with minor amounts of N_2 and H_2. The liquid phase contains sassolite (H_3BO_3) daughter crystals, occasionally arsenolite (As_2O_3) and mica. Total homogenization occurs around 365˚C. A second type occurs in trails and contains CH_4-H_2 gas mixture in a relative small bubble (15 vol.%, $T_H \approx 200$˚C). Tourmaline contains two types of fluid inclusions: 1) CH_4-rich vapour phase (± CO_2), 2) no gas in vapour bubble and sassolite (±arsenolite) in liquid phase. Both types have relative large vapour bubbles (40-60 vol%). Homogenization temperatures are about 370˚C.

Kurzfassung

Aplitisch-pegmatitische Gänge, welche meistens als steilstehende Gänge, Lagergänge und unregelmäßige Körper auftreten, wurden im Gebiet um den Monte Capanne Pluton und der Calamita Halbinsel (Elba, Italien) untersucht. Diese Gänge umfassen aplitisch-pegmatitische Körper östlich und einen porphyrischen Gang (Orano Porphyr) westlich des Monte Capanne Plutons.

Um den lokalen geologischen Zusammenhang und die Beziehung der Gänge mit den Nebengesteinen im Detail zu beschreiben wurden Proben genommen, aus denen Dünnschliffe präpariert wurden, um die mineralogischen und texturellen Merkmale detailliert zu untersuchen.

Zusätzlich wurden Dickschliffe (etwa 100 µm dick) für die Untersuchungen der Flüssigkeitseinschlüsse angefertigt. Sowohl Minerale als auch Flüssigkeitseinschlüsse wurden mittels optischer Mikroskopie, Raman Spektroskopie, Elektronenstrahlmikroanalyse und Mikrothermometrie untersucht.

Die aplitisch/pegmatitischen Gänge bestehen hauptsächlich aus Quarz, Plagioklas, Kalifeldspat mit starkem Entmischungscharakter, und lokal aus Glimmer, Turmalin und Andalusit. Der Porphyr beinhaltet Plagioklas-, Biotit- und xenomorphe, gerundete Quarz-Phänokristalle innerhalb einer feinkörnigen Matrix. Akzessorische Minerale in den aplitisch/pegmatitischen Gängen sind Zirkon, Xenotim, Monazit, Rutil/Brookit/Anatas, Apatit, Granat, Cordierit, Allanit, Titanit, Kolumbit, Kassiterit, Hämatit, Magnetit, Biotit, Hedenbergit, Sillimanit und Pyrit. Turmalin- und Andalusitkristalle werden durch magmatische Fließ-Strömung spröde deformiert (Boudins).

Turmalin ist stark zoniert, was sich durch grüne, braune, blaue und farblose pleochroitische Farben unter dem Mikroskop zeigt. Bei den Turmalinen in den Pegmatiten um den Monte Capanne Pluton handelt es sich um Schörl-Foitit Mischkristalle sowie Dravit-reiche Turmaline. Der farblose Turmalin der Schörl-Gruppe ist ein Mn-reicher Elbait. In Pegmatiten der Calamita Halbinsel treten zwei chemisch unterschiedliche Gruppen von Turmalinen auf, die aufgrund ihrer Zusammensetzung in einen Schörl-reichen und einen Dravit-reichen Turmalin gegliedert werden können. Die pinke Farbe des Andalusites hängt direkt mit dem Fe-Gehalt zusammen (bis zu 2,9 mass% FeO). Basierend auf dem Mg/Fe Verhältnis koexistierender Granat-Biotit Paare (Probe 57A) wurde eine Gleichgewichts-Temperatur von circa 600 °C berechnet. Rutil beinhaltet bis zu 7,0 mass% Nb_2O_5, 4,3 mass% SnO_2, 3,9 mass% Ta_2O_5 und 11,4 mass% FeO. Kolumbit beinhaltet 48,0-56,1 mass% Nb_2O_5, 9,3-15,7 mass% Ta_2O_5, 11,9-16,3 mass% FeO, 7,9-11,7 mass% WO_3 und 0,4-5,0 mass% Sc_2O_3. Einzelne Columbite weisen hohe Konzentrationen an schweren Seltenen Erden und Yttrium (22,0 mass% Y_2O_3) sowie Uran auf (11.8 mass% UO_2).

Die aplitisch/pegmatitischen Gänge enthalten eine große Anzahl an primärer Flüssigkeitseinschlüsse, die vorwiegend in Quarz auftreten. Zudem weisen auch Turmalin, Andalusit, Plagioklas, Allanit und Granat Flüssigkeitseinschlüsse auf. Quarze in Pegmatiten der ophiolithischen Einheit am Rand des Monte Capanne Plutons sind durch Einschlüsse (Durchmesser < 20 µm) mit einer ungefähren 42 vol-% Gasphase charakterisiert. Diese Phase besteht aus einer Mischung von CO_2 und CH_4 mit geringeren Gehalten an N_2 und H_2. Die Flüssigphase beinhaltet Sassolit (H_3BO_3) Tochterkristalle, gelegentlich auch Arsenolit (As_2O_3) und Glimmer. Die vollständige Homogenisierung der Einschlüsse findet bei ungefähr 365°C statt. Ein zweiter Typ von Flüssigkeitseinschlüssen tritt entlang von Spuren auf und beinhaltet eine CH4- H2 Gasmischung in einer relativ kleinen Blase (15 vol-%, $T_H \approx 200°C$). Turmalin beinhaltet zwei verschiedene Typen von Flüssigkeitseinschlüssen: 1) CH_4- reiche Gasphasen (± CO_2), 2) Gasblasen ohne CO_2, CH_4, N_2 und H_2 und Sassolit (± Arsenolit) in der Flüssigphase. Beide Typen weisen relativ große Gasblasen (40-60 vol-%) auf und homogenisieren bei ungefähr 370°C.

1. Introduction and motivation

1.1. Introduction

According to mythology, the island of Elba is the largest of the seven pearls, which the Goddess of love, Venus, has lost after she rose from the sea. Therefore, Elba is the largest island of the Tuscan Archipelago with an area of 223 km². About 50,000 years ago, the first inhabitants of Elba were Musterian, Neanderthal men. 2,000 years ago, people started to exploit the copper ores from ophiolitic sequences of western, central and eastern Elba. At around 650 B.C., the Etruscan mines of Elba and southern Tuscany became the major producers of iron and other metals such as copper, lead, zinc and silver. Aristotle refers to Elba when he speaks about a little island in the Etruscan region where metals were mined, and he calls this island "Aethalia" (sooty) owing to the smoke from smelting furnaces. After World War II and the destruction of Portoferraio, the smelting and the mining was concluded. Nowadays tourism and especially the collection of the famous minerals from Elba are economic forces.

In the course of this thesis, the complexity of the geology and the tectonic setting of Elba is once more shown, but via detection of the mineralogical characterisation and the formation conditions of aplite, pegmatite and quartz-tourmaline rich veins, a new perception of the studied area with the emplacement of the Monte Capanne pluton and the Eastern Elba pluton is given.

1.2. Scope of work

The topic of this thesis is the formation and the development of the aplites, pegmatites and quartz-tourmaline rich veins, which is due to the intrusion of magmatic bodies in the stratification of Elba over a period of 2.5 Ma. This magmatism led to numerous laccolithic or dyke intrusions as well as the Monte Capanne pluton in western Elba and the pluton in eastern Elba. The main pluton, which wasn't yet entire solidified, is cut by several late felsic units, identified by their field characteristics as the Cotoncello dyke, the leucogranite dykes and the aplite-pegmatite veins and dykes.

These aplite-pegmatite veins are not yet investigated very well in papers and in journals. The formation conditions, the thickness, the length as well as the mineralogy, the inclination and the appearance of these veins are still open to debate. Therefore, the aim of this thesis is not only to do ordinary analyses but also to combine newest fluid inclusion research (Microthermometry, Raman spectroscopy and electron microprobe analysis) and software calculation to increase knowledge on the formation conditions.

1.3. Geographical setting

The island of Elba is located at the northern end of the Tyrrhenian Sea at midway between Tuscany (Northern Apennines Chain) and Corsica (Alpine Corsica structural pile) and is 10 km away from the western coast of land-based Italy. Elba belongs to the Tuscan Archipelago, which contains seven islands (Fig. 1).

Fig. 1: Location of Elba in the Tyrrhenian Sea (OpenStreetMap 2014)

2. Geologic and Tectonic Setting

2.1. Regional geology

The island of Elba belongs to the Northern Apennines which is a fold-thrust belt formed during the Paleogene and Neogene by thrusting from W to E of the Ligurian units onto the external Tuscan-Umbria domain (Carmignani and Kligfield 1990). This belt or chain originated from Late Cretaceous-Eocene convergence of the European (Corsica-Sardinia block) and African (Adria microplate) continental margins as a consequence of the subduction of the interposed Jurassic Ligurian-Piedmontese oceanic domain of the western Tethys, succeeded by Oligocene-Early Miocene collision and Middle Miocene extension (Fig. 2) (Abbate et al. 1994; Bortolotti et al. 2001).

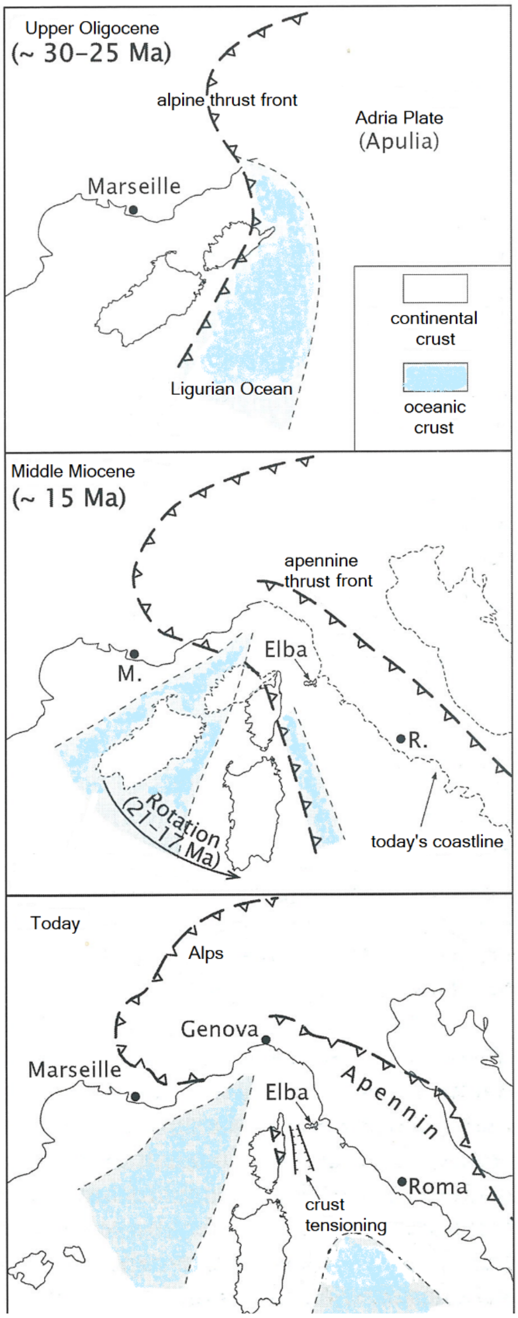

Fig. 2: Paleogeography of the Tyrrhenian Sea, after Frisch and Meschede (2011) *and* Frisch et al. (2008), *modified*

The lower Tuscan-Umbria domain represents the deformed and wedged margin of the Adria (Apulia) microplate (Tuscan Metamorphic Units and the Tuscan-Umbrian sedimentary Units like the Tuscan Nappe) and is formed by an Hercynian basement with its Mesozoic-Tertiary cover. This cover is first terrestrial, before continuing on a shallow sea and so it reflects the depression of a Jurassic passive margin. The rocks experienced a low-grade regional metamorphism due to the Early Miocene alpine orogenesis.

The Ligurian units are characterized by the presence of ophiolithe covered by Jurassic –Paleogene deep-water sediments and represent part of the Ligurian-Piedmontese Ocean. The youngest formation is flysch and the Ligurids are unmetamorphic units.

In Eocene eastward migrating of the Briançonnais microcontinent formerly belonging to the European plate, led to collision and deformation in the Apulia margin in the Upper Oligocene. During the Oligocene-Miocene evolution of the Northern

Apennines, subduction of the Apulia lithosphere occurred below the Corsica-Sardinia block (Briançonnais) (Fig. 2). Later, back-arc rifting due to slab retreat led to oceanic crust formation, first in the Algero-Provencal basin and then in the Tyrrhenian Sea, simultaneous with eastward migration of subduction, collision zone and deformation. This orogenic system evolved diachronously as the regime of extension migrated from west to east, trailing the retreat of the compressive regime (Fig. 3) (Boccaletti et al. 1997) and generated the nappe stack of Elba. Structural piling in the ophiolitic unit with eastward direction in the more external areas was coeval with the west directed backthrusts because of the shortening and thickening in the inner sectors. This means that the movement of the thrust fronts to two opposite directions happened during the same event and was caused by the same tectonic process. Soon after the collision, extensional collapse started to affect the wedge to result in a more stable configuration (Minelli and Keller 2003).

According to most authors, extensional tectonics began during the Miocene time interval in the inner sectors of the chain (like the area of Elba) through low-angle faulting, later followed by a high-angle faulting (Lavecchia 1988; Carmignani and Kligfield 1990; Bertini et al. 1994; Keller et al. 1994; Decandia et al. 2001) that progressively shifted to the east, trailing the Adriatic-vergent migration of the orogenic front. These extension events produced a crustal thinning in Western Tuscany, the formation of the Northern Tyrrhenian Sea with the eastwardly rotation of Corsica-Sardinia and the mainly NW/SE-trending tectonic basins with continental and marine clastic sedimentation.

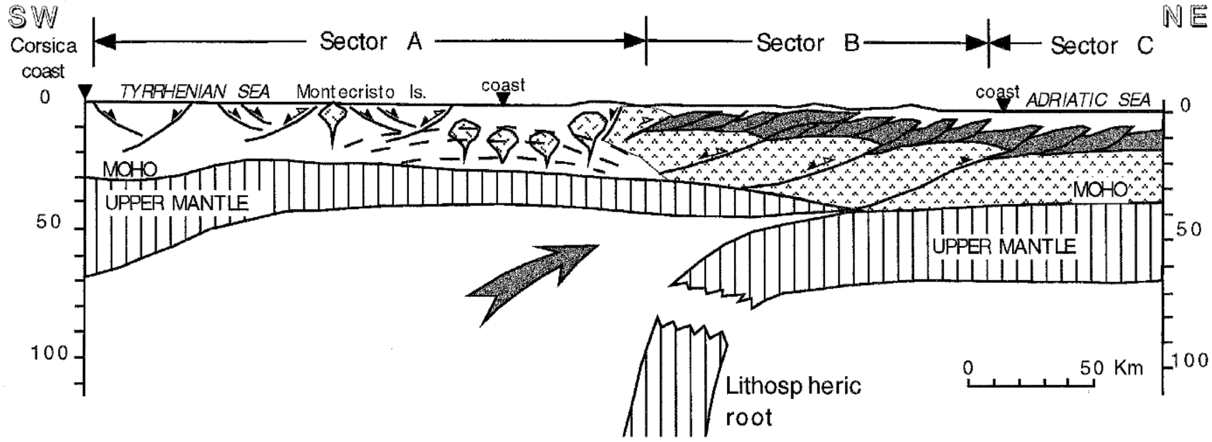

Fig. 3: Schematic profile from Corsica to the Adriatic Sea illustrating the deep structure in the Northern Apennines. Sector A is affected by extensional tectonics, sector C is affected by compressive tectonics and sector B is in-between, after Boccaletti et al. (1997)

(1) The slab rollback of the lithospheric mantle due to the slowdown of the subduction, (2) the extensional tectonics and connected to that (3) the astenospheric rise with partial melting led to the development of crustal- and mantle-derived magmatism in the Late Miocene (Fig. 3)

(Serri et al. 1993). So the variety of the so-called Tuscan Magmatic Province (TMP) of acidic to mafic intrusive and extrusive products exposed over about 30,000 km² of southern Tuscany and the northern Tyrrhenian Sea in four magmatic phases (Fig. 4) and generated heat flow anomalies, skarn and hydrothermal mineralisation (Poli 1992; Innocenti et al. 1997). This igneous activity migrated from west (14 Ma) to east (0.2 Ma) in an extensional ensialic back-arc setting as the west-dipping Adriatic plate delaminated and rolled back to the east (Serri et al. 1993; Dini et al. 2002).

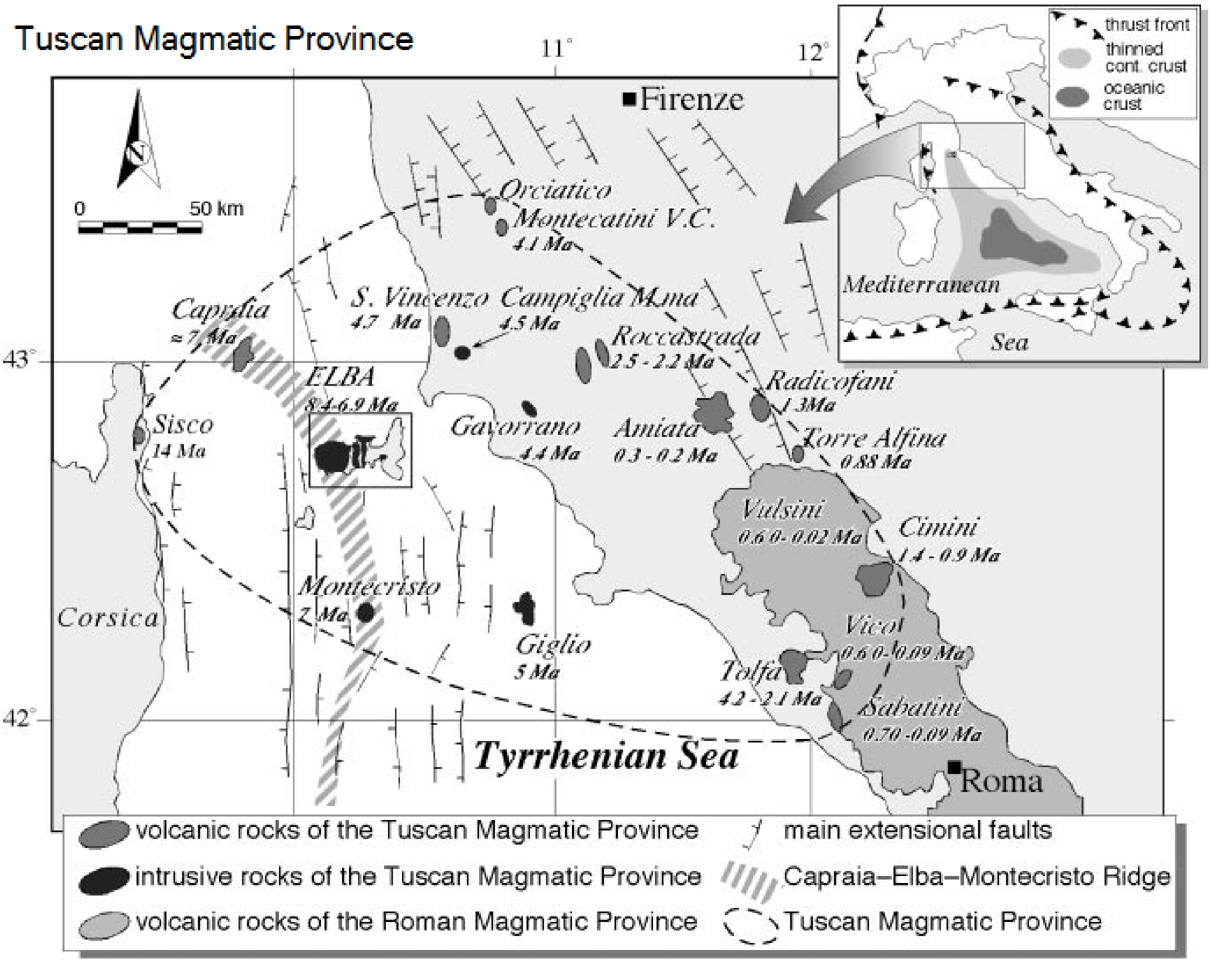

Fig. 4: Distribution map of the eastward-migrated magmatic bodies of the Tuscan Magmatic Province. The younger (ultra)potassic volcanic rocks of the Roman Magmatic Province are also reported , after Dini et al. (2002)

On the island of Elba, several laccoliths, two plutons with the intrusion of the Monte Capanne monzogranite, the covered Eastern Elba (Porto Azzurro) monzogranite and an extensive dyke swarm were emplaced within stacked tectonic complexes. Finally, the emplacement of the plutons produced local uplifts.

2.2. Tectonic complexes of Elba Island

Elba Island is constructed from five tectonic complexes (Fig. 5) that were thrust onto each other in the Early Miocene (about 20 Ma). The lower three complexes have continental features (the Tuscan Units) and the upper two (the Ligurids) are oceanic in character and contain several late Miocene intrusive bodies of variable size (Trevisan 1950; Marinelli and Trevisan 1967; Bortolotti et al. 2001). Frisch et al. (2008) refer to a new concept consisting of five Units. *Complex I* and *II* belong to *Unit 1*, whereas *Unit 2* (Rio Marina sliver) corresponds to the Ligurids. It attained to this position between two Tuscan Units by two overthrusts (Fig. 6).

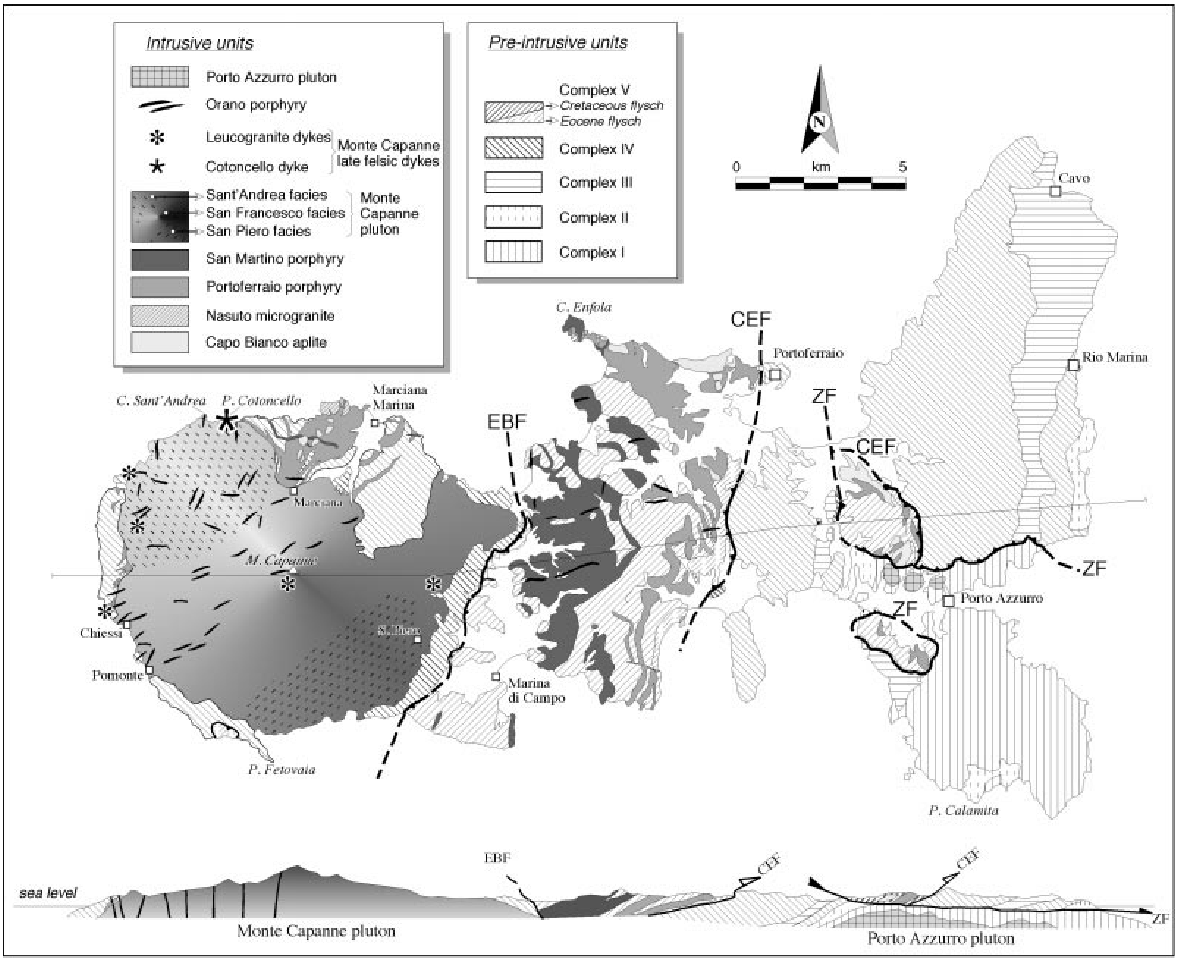

Fig. 5: Geological sketch map and generalized cross-section of Elba. EBF - Eastern Border Fault; CEF - Central Elba Fault; ZF - Zuccale Fault, after Dini et al. (2002), *modified after* Marinelli and Trevisan (1967)

Successive tectonic processes are directly related to the stacking of these complexes: Accretion and underplating of oceanic material occurred probably during the Middle Cretaceous and went on until the Middle Eocene. During Oligocene-Miocene, collision of the tectonic wedge with the continental margin of Tuscany occurred and the latter was overthrusted by oceanic crust. During this collisional stage, low-grade metamorphic conditions were generated and affected terrains like the *Complex II* in Elba, while shortening caused an out-of-sequence thrust to place *Complex III* on top of a sliver of serpentinites (*Unit 2*) that already overlaid *Complex II*. This resulted in the complex nappe stacking of Elba. In the third stage, due to the orogenic collapse, extensional tectonics overprinted the stacked structures and finally the hybrid magmas intruded the thinned continental crust with pluton emplacement were causing gravitational tectonics and led to the present geological setting of the area (Minelli and Keller 2003; Keller et al. 1994). See also the geological map Fig. 7. From bottom to top of the tectonic pile (Fig. 6), the units are:

Complex I and *II* or *Unit 1* after Frisch et al. (2008)(Fig. 5 + Fig. 7) include the Variscan (Hercynian) basement (the Porto Azzurro Unit with the Monte Calamita Formation), the cover (the Ortano Unit) and the Aquadolce Unit.

The rocks of the ***Porto Azzurro Unit (PU)*** outcrop in the southeasternmost portion of the island covering the entire Calamita peninsula. They consist of muscovite-biotite schists with a metamorphic greenschist facies, which are topped by quartzites and dolomitic carbonate rocks. The age of the uppermost part of the basement schists is supposed to be Palaeozoic. Because of the emplacement of the covered Eastern Elba or (La Serra -) Porto Azzurro Pluton, the Calamita Schists experienced contact metamorphism and an extremely complicated intrusive array of late **tourmaline-rich aplitic and granitic veins and dykes**. Therefore, there are several schists with related porphyroblasts such as andalusite, biotite, muscovite, plagioclase and corundum. The post-Variscan cover is influenced by Alpine Epi-Metamorphism. It crops out on the eastern part of Elba around the town of Rio Marina and in the valley of Ortano and is described as the ***Ortano Unit (UO)***. The Rio Marina Formation or formerly the Capo d'Arco Schists consists of phyllites, quartzites and serizitic schists and is analogue to the formation in *Complex III*. In the hanging wall of the Ortano Unit, there are Porphyroids (metavolcanites) that have been correlated with the Tuscan Metamorphic sequences in the Apuane Alps ("Scisti porfirici"), as well as rocks similar to the Verrucano Formation. The age of this Unit has been referred to be Permian (Babbini et al. 2001). It is locally intruded by aplitic dykes (Musumeci et al. 2011). The ***Acquadolce Unit (AU)*** is composed of the Valdana marbles, a grey dolomitic limestone, grading upwards into calcschists and the Cipollino marbles with its onion ("cipolla") skin weathering and their Jurassic age. Finally, there are phyllites, metasiltstones with intercalations of calcschists, which contain fossils of Early Cretaceous age (Pandeli et al. 2006).

Unit 2 after Frisch et al. (2008) also belongs to *Complex II* (Fig. 6 + Fig. 7) and is a sliver of serpentinites (Rio Marina sliver) which separates *Unit 1* and *3*. It corresponds to the Ligurids and attained to this position by two overthrusts. This complicated tectonic setting is also visualized by the highly deformed metaserpentinite as well as abundant slickensides and faults.

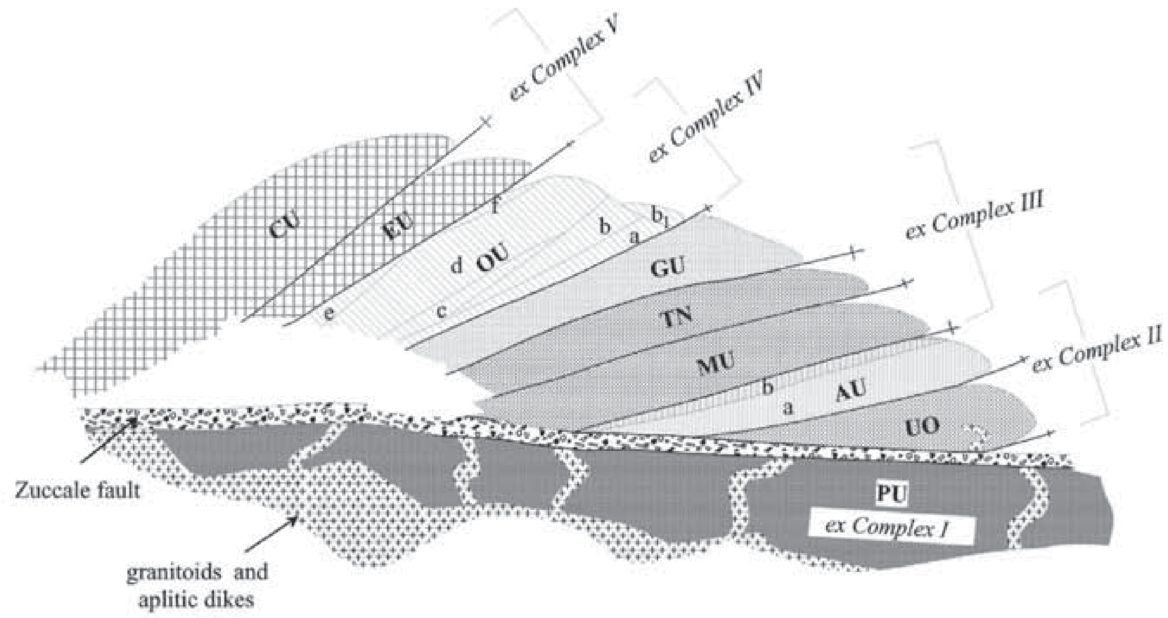

Fig. 6: The central and eastern Elba tectonic pile, PU - Porto Azzurro Unit; UO - Ortano Unit; AU - Aquadolce Unit (b. Rio Marina sliver); MU - Monticiano-Roccastrada Unit; TN - Tuscan Nappe; GU – Gràssera Unit; OU – Ophiolitic Unit; EU – Paleogene Flysch Unit; CU – Cretaceous Flysch Unit, after Bortolotti et al. (2001)

Complex III or *Unit 3* after Frisch et al. (2008)(Fig. 5 + Fig. 7) crops out along a narrow N-S trending area along the northeast side of Elba from Cavo to Mte. Arco and includes the Monticiano – Roccastrada Unit (with the Rio Marina Formation), the Tuscan Nappe and the Gràssera Unit. It consists of a phyllitic basement of Carboniferous age and of a sedimentary cover sequence with an age that encompasses all the Mesozoic going until the Oligocene and includes most of the iron ore deposits between Porto Azzurro and Cavo. The ***Monticiano – Roccastrada Unit (MU)*** and its Rio Marina Formation is analogue to the Porto Azzurro cover (*Unit 1*) and is composed of dark, graphitic phyllites with quartzitic parts, which experienced an Early Miocene regional metamorphism. The first formation of the cover is the Verrucano with a Middle-Upper Triassic age, classically consisting of purple, greenish or white quartzites and shists, and of pink conglomerates that in Elba form a series of cliffs to the north of the town of Rio Marina. The Verrucano Formation is a terrestrial sediment that deposited in an arid climate. Therefore, it has a reddish colour caused by finely dispersed hematite and is the primary source for iron in the deposits. The ***Tuscan Nappe (TN)*** consists in lower levels of evaporitic calcareous-dolomitic, cataclastic breccias known as Calcare Cavernoso ("cellular" limestone) of Norian age, which can be found south of the locality La Parata. The sequence is topped with Rhaetian to Hettangian shallow water limestones, which contain the mussel Rhaetavicula Contorta as well as white micritic massive limestones related to the Calcare Massicio of Lower Liassic age. The upper formations are (1) pelagic nodular and cherty limestones from the Middle-Upper Liassic and (2) red, brownish, micritic, pelagic limestones with relics of ammonites ("Rosso Ammonitico"). Peak metamorphic conditions do not exceed the anchizone/subgreenschist facies conditions. The anchimetamorphic ***Gràssera Unit (GU)***, possibly of Cretaceous age, mostly consists of varicoloured slates with rare carbonate-siliceous and radiolarian cherts intercalations (Cavo Fm.). At Capo Castello and south of Capo Pero, there are also coloured basal Calcschists. In addition, horizons of turbiditic sandstones equivalent to the Macigno formation of Oligocene age were found (Bortolotti et al. 2001; Minelli and Keller 2003; Frisch et al. 2008; Pandeli et al. 2006).

Complex IV or *Unit 4* after Frisch et al. (2008)(Fig. 6 + Fig. 7) comprises of the ophiolitic sequence that has been correlated to the ophiolites of the Early-Middle Jurassic Ligurian domain of the Northern Apennines. The ***Ophiolitic Unit (OU)*** is composed of seven tectonic subunits including a basement of anchimetamorphic lherzolitic-harzburgitic serpentinites, cataclastic ophicalcites, Mg-gabbros with diorites and tholeiitic basalts (mostly pillow basalts) that are overlain by a volcanic-sedimentary cover. The cover consists of red radiolarites (Volterraio Fm.), argillite interbedded with siliceous brownish limestones (Nisportino Fm.) and massive bright Calpionella limestones whose age is respectively Malm and Upper Jurassic-Lower Cretaceous. Classically in the Northern Apennines Ligurian ophiolites, the uppermost formation is represented by the siliceous or cherty shales of the Argille a Palombini (from the Lower-Middle Cretaceous) that rest on the Calpionella limestones. In contrast, both in central and eastern Elba, this sequence is not present as the Palombini shales are always overthrust by the basal serpentinites. Hence, the entire ophiolitic unit overlies the Palombini shales. A **shoshonitic dike** (Mt. Castello Dike: 5.8 Ma) fills ENE-WSW – trending normal faults within this Unit. Similar dikes were also present in the Capo Stella promontory (Mt. Capo Stella dikes) (Conticelli et al. 2001).

Complex V or *Unit 5* after Frisch et al. (2008)(Fig. 5 + Fig. 7) comprises of the turbiditic Flysch formations with the best exposures being found in the Central part of Elba. The ***Paleogene Flysch Unit (EU)*** is constituted by an Eocene succession including clay and shales with calcareous-marly, calcarenitic and arenaceous intercalations and, locally, by ophiolitic-carbonate breccias (Colle Reciso Fm.). **Acidic dikes and laccoliths** intrude into the two Flysch Units (Dini et al. 2002): Aplites (Capo Bianco Aplites: 7.9 Ma), locally sericitised (the so-called “Eurite”: Maineri et al. 2003), and porphyries (Portoferraio Porphyries: 8.2 Ma and San Martino Porphyries: 7.4 – 7.2 Ma) intrude the sedimentary succession, but do not crosscut the basal contact with the underlying Ophiolitic Unit. The ***Cretaceous Flysch Unit (CU)*** consists of a basal tectonised part with sandstones and granites (in Elba defined with the name Ghiaieto Sandstones after Bortolotti et al. (2001)), where the top part consists of calcareous marls (calcareous turbidites and calcarenites), shales and thin sandstone beds, representing turbiditic sands (the Marina di Campo Fm.) of Late Cretaceous Age. Similarly to the ***EU***, this Unit is frequently intruded by locally thick **acidic dikes and laccoliths**.

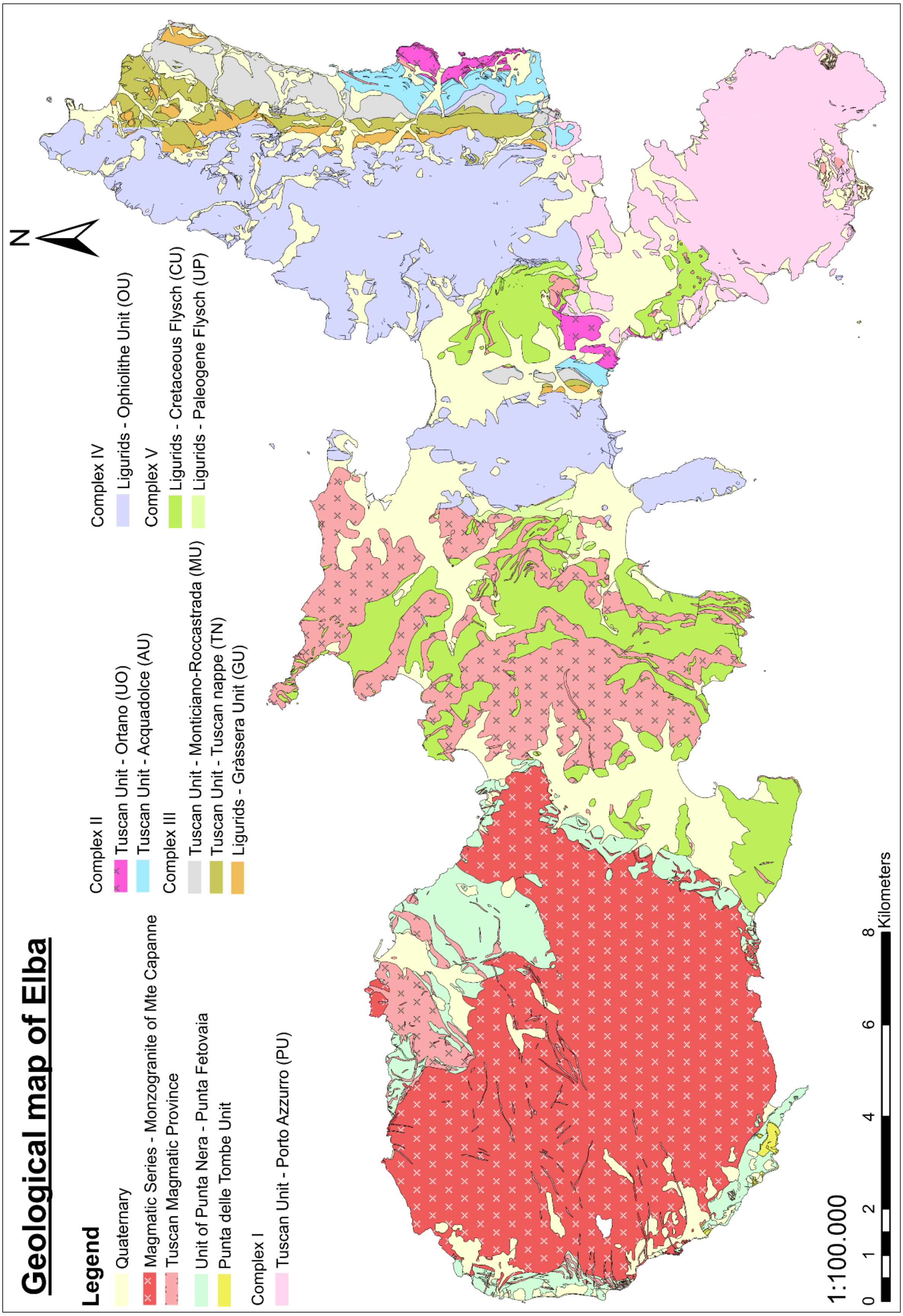

Fig. 7: Geological map of Elba, modified after Marinelli and Trevisan (1967) *and* Babbini et al. (2001). *Website:* Regione Toscana 2014

3. The Late Miocene magmatic evolution

The Late Miocene magmatism of Elba Island belongs to the Tuscan Magmatic Province (TMP) (Fig. 4) and reflects the eastward migration as the west-dipping Adriatic plate delaminated and rolled back to the east (see Chapter 2.1). From about 8.5 to 6.8 Ma, this igneous activity occurred at western Elba. Due to the emplacement of the Monte Capanne pluton (6.5 Ma) and consequentially due to local uplifts, the overlying rocks and flysch slipped eastward along the low-angle *Central Elba fault* (CEF) (Fig. 5 + Fig. 8), which also separated central Elba from eastern Elba expressed as a tectonic mélange of rocks from *Complex IV* and *V* (Trevisan 1950). In addition, the displacement of the CEF by 7-8 km allowed a hydrothermal circulation of fluids. Later on at an unknown date, the CEF was cut by a moderately to steeply eastward dipping fault, the *Eastern Border fault* (EBF), which separated western Elba from central Elba and roughly parallels the east side of the Monte Capanne pluton, truncating its contact aureole (Fig. 5 + Fig. 8). The igneous activity of Eastern Elba started 5.9 Ma ago with the intrusion of the covered Eastern Elba (Porto Azzurro) pluton. Due to the emplacement of this pluton, fluid circulation led to the iron skarn and iron ore deposits. At the end of the iron ore generation 5.4 Ma ago and because of the emplacement of both plutons, eastern Elba was displaced eastward by 5-6 km along the new *Zuccale fault* (ZF), whose activity is geometrically and kinematically similar to that inferred for the CEF (Fig. 8) (Dini et al. 2002).

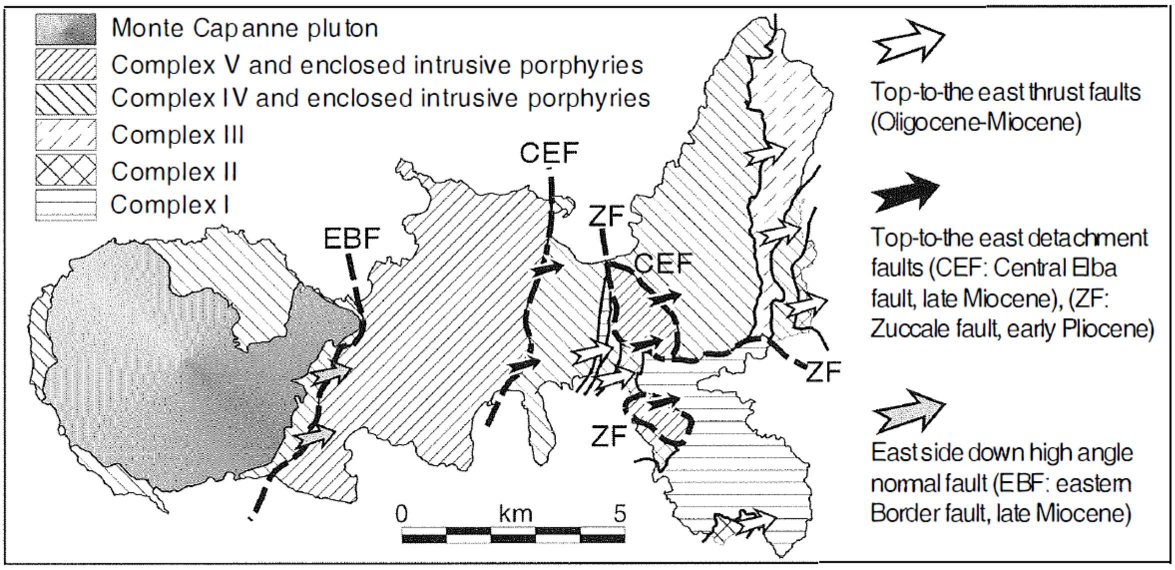

Fig. 8: The large-scale faults of Elba Island, after Rocchi et al. (2003)

The evolution of the igneous products is influenced by following processes (Fig. 9): (1) Melting due to subduction and interaction between subducted lithosphere and asthenosphere, the water content in the subducted plate resulted in a lowering of the melting point of the peridotites. Moreover, metasomatism developed via carried ions in the watery fluids. (2) As a result of the eastward rollback of the Adriatic plate, hot asthenospheric rose with another partial melting of the mantle material (high-K melts). (3) Extensional tectonics and mantle-derived magma led to heating and melting of the continental crust (with melting temperatures about 1200°C).

All the different igneous products and their mixing, volumes and ages are shown in Fig. 9.

0.4	low	28	**volume (km^3)**	24	~ 200	low	very low	low
no	no	no	**mafic enclaves**	common	common. variable %	no	small	common
1.42	1.29	1.18	**average ASI**	1.22	1.11	1.15	1.16	0.94 (min)
0.7115-0.7133	0.7146	0.7144	**$^{87}Sr/^{86}Sr(t)$**	0.7162	0.7145 - 0.7147	0.7145	0.7228	0.7115 (min)
-9.6	-9.9	-10.0	**$\varepsilon_{Nd}(t)$**	-8.8	-8.1 - -8.8	-8.6	-9.7	-7.0 (max)

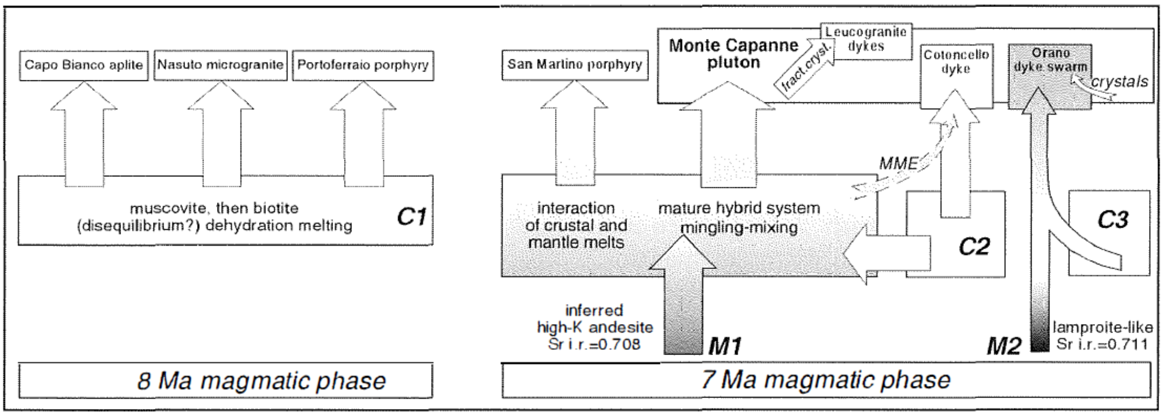

Fig. 9: Schematic model for the genesis of Elba igneous products throughout the time. M1, M2 and C1, C2, C3 are different mantle and crustal melts. MME: mafic microgranular enclaves. Modified after Dini et al. (2002)

The so-called Tuscan Magmatic Province Rocks or the intrusive units and sequence of Elba Island are (Fig. 5):

1.a. Capo Bianco porphyritic aplites – These rock bodies (ca. 8 Ma) are white porphyritic rocks with alkali-feldspar granite compositions and crop out in the north coast of the central and western part of Elba within *Complex V* as four adjacent but isolated caps on a ridge and in central Elba as a structurally higher tourmaline-rich laccolith layer (Fig. 10)(Westerman et al. 2004). They were earlier described as "Eurite" (Maineri et al. 2003) and are characterised by a fine-grained, homogeneous texture with scarce millimetric phenocrysts of quartz, K-feldspar, oligoclase and muscovite which was affected by hydrothermal recrystallization of the acidic plagioclase and of the K-feldspar into sericite in minor outcrops and by fine-grained aggregates (up to 3 mm in size) of blue tourmaline (Dini et al. 2002).

1.b. Nasuto microgranite – With a syenogranitic composition, the Nasuto microgranite crops out over a small area along the northern shore of western Elba and it is entirely surrounded and intruded by the younger Portoferraio porphyry.

1.c. Portoferraio porphyry – This porphyry (ca. 8.2 Ma) has dominantly monzogranitic compositions and occurs as major laccolith layers up to 700 m thick with minor syenogranitic inclusions, commonly interconnected was well as numerous dykes (Fig. 10). The rocks are well exposed in the western and central part of Elba within the Flysch Units. Close to the contact with the Monte Capanne pluton, the Portoferraio porphyry exhibits a strong mylonitic foliation in the groundmass, with quartz phenocrysts having subgrain boundaries, plagioclase cracks cemented by micrographic quartz plus K-feldspar, and biotite as oriented polycrystalline (Dini et al. 2002).

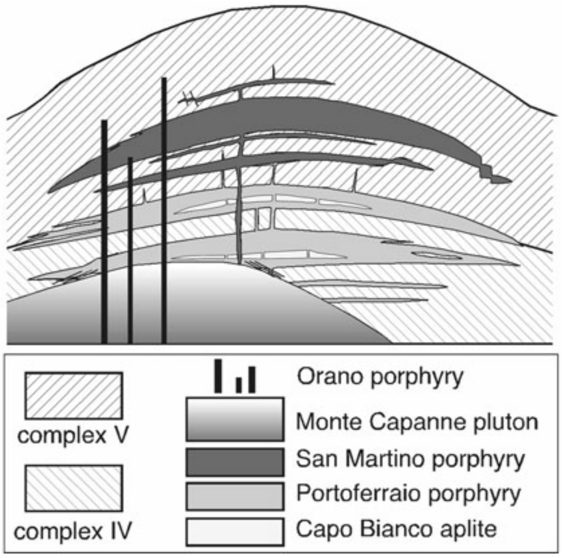

Fig. 10: Sketch of the geometrical relationships between the magmatic bodies of central and western Elba Island at 6.8 Ma, after Pandeli et al. (2010)

2.a. San Martino porphyry – This rock body (ca. 7.4 Ma) has monzogranitic compositions and is characterized by prominent K-feldspar megacrysts (up to 15 cm in size), biotite and local granodioritic-tonalitic mafic enclaves. This unit occurs in western Elba as dykes cutting the Capo Bianco aplite and Portoferraio porphyry, whereas in central Elba, it occurs as three main laccolith layers up to 400 m thick and as minor cross-cutting dykes (Fig. 10)(Westerman et al. 2004).

2.b. Monte Capanne pluton – The Monte Capanne monzogranitic pluton (ca. 6.8 – 7.0 Ma) is the largest of those exposed in the TMP (Poli 1992). It is roughly circular and is bordered along two-thirds of its perimeter by contact-metamorphosed rocks mainly after *Complex IV* protoliths (Fig. 10). The whole intrusive mass is characterized by the widespread occurrence of mafic microgranular enclaves of strongly variable size and composition (tonalite to monzogranite). Several types of late felsic products are also present.

2.c. Late felsic products associated with the Monte Capanne pluton – The main pluton is cut by several felsic units, identified by their field characteristics as the Cotoncello dyke (north-west Elba), the leucogranite dykes and the aplite-pegmatite veins and dykes. At Punta del Cotoncello, the syenogranitic Cotoncello dyke exhibits a modest K-feldspar megacryst content and a distinctively finer-grained matrix than the main pluton which it cuts. The leucogranite dykes also have syenogranitic compositions, and they occur mainly close to the pluton's contact, within both the pluton and its thermometamorphic aureole. They commonly have thicknesses up to tens of metres. These dykes were emplaced late in the crystallization sequence of the Monte Capanne pluton, and are locally cut by dykes of the Orano porphyry. Aplite-pegmatite veins and dykes occur commonly as thin (0.1 to 2 m) masses, in some places cross-cutting the leucogranite dykes (Dini et al. 2002). These felsic units represent one of the studied localities near the Monte Capanne pluton (Fig. 24).

3.a. Orano porphyry – This unit is an E-W trending swarm of nearly 100 darkly coloured dykes that cross-cut all the other intrusive units of the sequence (Fig. 10). They are restricted in western Elba to the northwestern portion of the Monte Capanne pluton and its contact aureole. In central Elba, the Orano dykes crop out only in the northern part of the area. Dyke thicknesses range from less than a metre up to a maximum of 50 m and contacts with host rocks are sharp and planar. Both zoned and unzoned dykes are recognized. Outer border zones are typically a few tens of centimetres thick and are distinguished from the inner zones by (1) finer grained groundmass, (2) lower content of K-feldspar and quartz xenocrysts, mafic microgranular enclaves and xenoliths and (3) higher ferromagnesian mineral concentrations. The inner portions of zoned dykes have monzogranitic compositions and the borders of zoned dykes have granodiorite to quartz-monzodiorite compositions. Finally, the unzoned Orano dykes show evidence of early magma mingling including for example three populations of plagioclase phenocrysts having strong differences in composition and texture and coexisting quartz and olivine plus clinopyroxene phenocrysts. The Orano porphyry is the youngest intrusive unit in both western and central Elba. Initial isotopic ratios were corrected to 6.85 Ma, accounting for a cooling age for Orano dykes that is essentially the same as that of the Monte Capanne pluton (Dini et al. 2002; Rocchi et al. 2003). Sample 15A represents this unit, which was also studied near the Monte Capanne pluton (Fig. 24).

4.a. (La Serra-) Porto Azzurro pluton – Only small outcrops of this covered eastern Elba monzogranitic body (after Serri et al. 1993) can be found in the Porto Azzurro area (Fig. 5). The composition is similar to the most acidic portions of the Monte Capanne pluton and the emplacement is constrained at 5.9 Ma (Maineri et al. 2003). Because of the emplacement, many aplites intruded in the Calamita Schists and the younger Monte Castello dyke cross-cut some of these aplites.

4.b. Monte Castello mafic dyke – A grey-brownish porphyritic dyke is found in eastern Elba. The rock is quite altered and the original phenocryst assemblage was constituted of plagioclase, clinopyroxene, olivine and scattered K-feldspar megacrysts. The dyke had an original shoshonite composition and an emplacement age of 5.8 Ma (Conticelli et al. 2001). Its petrographic and geochemical feature resemble those between the Orano dykes and also the close age relations to the Porto Azzurro pluton resemble those between the Orano dyke swarm and the Monte Capanne pluton. Thus, similar pluton-mafic dykes history occurred in western Elba at 6.9 – 6.8 Ma, and in eastern Elba 1 myr later.

4.c. Acidic dykes of eastern Elba – These whitish rocks constitute the locally intricate dyke swarms of the (La Serra-) Porto Azzurro pluton, intruded in the Mt. Calamita Formation and in the Capo d'Arco Schists. Their size is centimetric to metric and the composition granitic to aplitic. They consist of orthoclase (sometimes perthitic), quartz, plagioclase and minor amounts of biotite, black tourmaline, andalusite or cordierite and muscovite. Apatite and zircon are accessory minerals. **Veins of quartz+tourmaline can be locally associated to the aplitic rocks.** The K-Ar radiometric age of the aplites are in the range of those obtained from the (La Serra-) Porto Azzurro monzogranite (5.4-5.1 Ma)(Bortolotti et al. 2001). These dykes represent the other studied locality at the Calamita peninsula (Fig. 24).

The *Mt. Capo Stella dykes* (grey-greenish porphyritic dykes), the *Casa Carpini lamprophyries* (porphyritic, grey-whitish rocks with a more alkaline composition) and the *Skarns* (metasomatic FeCa silicates and Fe ores) are additional rocks of the TMP.

4. Pegmatites

4.1. An Introduction to Pegmatites

Pegmatite is an essentially igneous rock, usually of granitic composition, that is distinguished from other igneous rocks by its extremely coarse but variable grain-size or by an abundance of crystals with skeletal, graphic, or other directional growth-habits (Fig. 11). Pegmatites occur as sharply bounded homogeneous to zoned bodies within igneous or metamorphic host-rocks. Granitic bulk-compositions are the most common and are also associated with hydrothermal systems. Pegmatites also are derived from plutonic bodies of mafic and alkaline rocks and carbonatites. Although the common igneous rocks consist of quartz, K-feldspar and mica, elements including lithium, beryllium, rubidium, cesium, niobium, tantalum, tin, the rare-earth elements, boron, phosphorus and fluorine can become enriched to weight-percent levels within granitic pegmatites (London 2008).

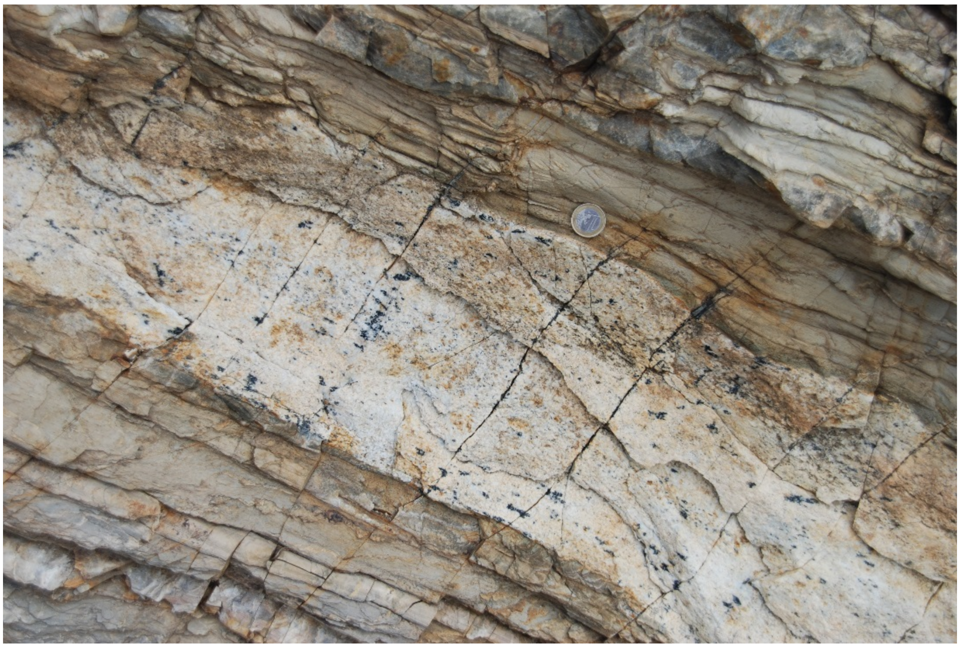

Fig. 11: A pegmatite dyke with black tourmaline crystals,
Elba Island (photo by R.J. Bakker, October 2013)

Černý (1991) regarded the pegmatite group as the basic genetic unit of association among pegmatite bodies. A pegmatite group can consist of tens to thousands of individual exposed pegmatites, which may or may not be traceable to a specific source pluton. Conversely, all pegmatites found in a single terrane may not have the same source and hence are not part of a single group. Due to improved petrological, paragenetic and geochemical criteria, the five geological classes (abyssal, muscovite, muscovite–rare-element, rare-element and miarolitic) are revised by a separate concept of three petrogenetic families (NYF, LCT and mixed). The following scheme, as modified by Černý (1991) and revised by Černý and Ercit (2005), is widely used today (Fig. 12):

The abyssal class – Abyssal pegmatites encompas pegmatites of intermediate depth but in largely dehydrated high-temperature host terranes. They most commonly correspond to products of partial melting or metamorphic re-equilibration and are defined by their amphibolite- to granulite-facies hosts. Migmatitic rocks can possess domains of leucosome that are very coarse-grained.

The muscovite class – Pegmatites of this class are largely conformable to host rocks of high-pressure amphibolite facies and are in part deformed with them. They are characterized by the kyanite– sillimanite progression and are generated directly by partial melting or by differentiation.

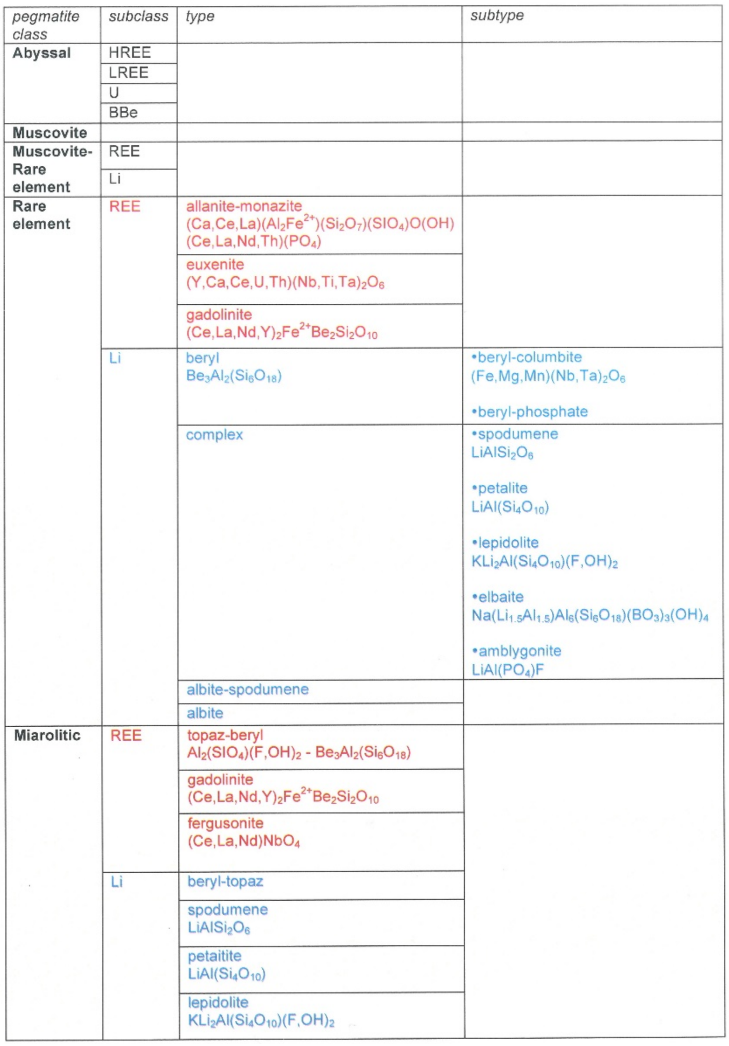

pegmatite class	*subclass*	*type*	*subtype*
Abyssal	HREE		
	LREE		
	U		
	BBe		
Muscovite			
Muscovite-Rare element	REE		
	Li		
Rare element	REE	allanite-monazite $(Ca,Ce,La)(Al_2Fe^{2+})(Si_2O_7)(SIO_4)O(OH)$ $(Ce,La,Nd,Th)(PO_4)$	
		euxenite $(Y,Ca,Ce,U,Th)(Nb,Ti,Ta)_2O_6$	
		gadolinite $(Ce,La,Nd,Y)_2Fe^{2+}Be_2Si_2O_{10}$	
	Li	beryl $Be_3Al_2(Si_6O_{18})$	•beryl-columbite $(Fe,Mg,Mn)(Nb,Ta)_2O_6$ •beryl-phosphate
		complex	•spodumene $LiAlSi_2O_6$ •petalite $LiAl(Si_4O_{10})$ •lepidolite $KLi_2Al(Si_4O_{10})(F,OH)_2$ •elbaite $Na(Li_{1.5}Al_{1.5})Al_6(Si_6O_{18})(BO_3)_3(OH)_4$ •amblygonite $LiAl(PO_4)F$
		albite-spodumene	
		albite	
Miarolitic	REE	topaz-beryl $Al_2(SIO_4)(F,OH)_2$ - $Be_3Al_2(Si_6O_{18})$	
		gadolinite $(Ce,La,Nd,Y)_2Fe^{2+}Be_2Si_2O_{10}$	
		fergusonite $(Ce,La,Nd)NbO_4$	
	Li	beryl-topaz	
		spodumene $LiAlSi_2O_6$	
		petaitite $LiAl(Si_4O_{10})$	
		lepidolite $KLi_2Al(Si_4O_{10})(F,OH)_2$	

Fig. 12: The pegmatite classification scheme, the blue types belong to the LCT and the red types belong to the NYF pegmatite family, modified after Černý and Ercit (2005)

The muscovite – rare-element class – This class represents intrusive bodies that form part of a continuum from granite to rare-element pegmatite. Pegmatites that have intruded mica-rich host rocks can have a pronounced enrichment of very coarse-grained muscovite or biotite at their margins.

The rare-element class – This class encompasses pegmatites generated by differentiation from granitic plutons, emplaced largely at intermediate to relatively shallow depth, and marked by a tendency to accumulate economic concentration of lithophile rare elements in the more fractionated pegmatite bodies. These pegmatites mostly intrude hosts that record conditions of peak metamorphism appropriate for the lower-pressure portions of the greenschist and amphibolite metamorphic facies.

The miarolitic class – These pegmatites are distinguished by an abundance of open- or clay-filled and crystal-lined cavities called miaroles. The primary cavities result from trapping bubbles (aqueous or carbonic vapour) of an exsolved gas phase inside the parent pegmatite body. Low-pressure environments favour the exsolution of dissolved gases and the creation of large cavities frozen into the pegmatite because the solubility of volatiles in melt decreases with decreasing pressure and the volume that the vapour occupies increases with decreasing pressure. The miarolitic class pegmatites occur as numerous small segregations within shallowly emplaced granitic plutons. A wholly different type of miarolitic pegmatite forms intrusive pegmatites, from concentrically zoned vertical bodies to shallowly dipping layered dykes. Miarolitic pegmatites are the principal pegmatitic sources of gem materials and fine mineral specimens.

Pegmatite families – Černý (1991) proposed two petrogenetic families, abbreviated as “LCT” and “NYF” (sometimes there is a mixed type as well), that correspond to the most distinctive enrichment of elements produced by fractionation within chemically distinct pegmatite groups. *LCT* stands for lithium, cesium, tantalum, a characteristic enrichment found mostly, but perhaps not exclusively, in S-type granites that originate from metasedimentary rocks rich in muscovite. Their peraluminous nature is expressed by the presence of muscovite, tourmaline, spessartine-rich garnet and rarely gahnite, topaz or andalusite. Their parent melts form by anatexis of undepleted upper- to middle-crust metasedimentary and metavolcanic protoliths or low-percentage anatexis of igneous rocks of the basement. *NYF* represents niobium, yttrium and REE and fluorine, a characteristic suite of elements in the granites and pegmatites that are normally labelled as A-type or “within plate” granites. The NYF pegmatites are associated with granite magmatism that is thought to originate by deep melting of crust within continental rift zones, usually with some chemical input from mantle sources.

4.2. The pegmatites of Elba Island

The aplite-pegmatite intrusions of the Monte Capanne pluton in the western part of the Elba Island and the intrusions of the (La Serra-) Porto Azzurro pluton of the eastern part are known for their excellent pocket collectibles and rare accessory minerals. Moreover, these intrusions are the only representatives of Li-bearing pegmatites in Italy. One approach to the study of zoned pegmatites is the use of minerals with variable compositions and textures (e.g. tourmaline, beryl, micas, and feldspars) as recorders of petrogenetic information. The chemistry of tourmalines (and in some respects the colour) may be used to reveal the fractionation trends and relative degree of evolution of the host rocks. Distinct types of textures of many minerals also evidence the evolution of the physicochemical conditions of crystallisation (Pezzotta 2000).

The miarolitic Li-bearing aplite-pegmatite dykes and the associated aplite dyke swarms (Pezzotta 2000) are widespread along the eastern contact of the Monte Capanne pluton in its peripheral parts and in the surrounding thermometamorphic rocks (e.g. S. Piero in Campo and S. Ilario in Campo). They consist of outer portions with a typically aplitic texture, which sometimes form most of the dyke, and a central pegmatitic core. The aplitic portions are characterized by a variable grain size and are principally made up of quartz, K-feldspar, plagioclase (albite to oligoclase), tourmaline, muscovite and ± biotite. The pegmatitic zone mainly consists of K-feldspar, quartz and tourmaline. In the central parts of this zone, miarolitic cavities and pockets of several tens of mineral species may occur. Two main stages of paragenetic sequence have already been recognised: first an "aplitic-pegmatitic" stage, consisting of K-feldspar, albite, quartz, tourmaline (variously coloured), beryl, lepidolite, petalite, pollucite and garnet. And second, a "hydrothermal stage" responsible for crystallization of several zeolites, pink tourmaline (elbaite) and calcite and the alteration of K-feldspar into kaolinite and zeolites. Ruggieri and Lattanzi (1992) described these pegmatites as "miarolitic (shallow depth) pegmatites" in the classification scheme of Černý (see Chapter 4.1). The same authors, studying fluid inclusions, calculated the upper pressure limit for pegmatitic crystallization at ~ 2 kbar. Fracture fillings in the granodiorite of the eastern margin of the Monte Capanne pluton, associated with quartz and black tourmaline crystallization and local hydrothermal alterations, are also present. These brittle structures, with negligible vertical movement slip, locally crosscut the miarolitic pegmatites (Aurisicchio et al. 1999).

The aplite-pegmatite dykes were classified into four categories, but dykes with characteristics transitional between those are not uncommon (Pezzotta 2000): *1.* dykes without Li minerals, *2.* Li-bearing dykes with complex asymmetric zoning, *3.* Li-bearing dykes with simple asymmetric zoning and 4. irregularly zoned to unzoned Li-bearing dykes.

1. Dykes without Li minerals – These dykes are characterized by lack of Li-Cs minerals and by the presence of tourmaline crystals of exclusively black colour. These intrusions are abundant and are hosted by the monzogranite. They do not display significant textural or mineralogical zoning and are mainly aplitic, with the pegmatitic portions dispersed as irregular pods and veins. The main components of the aplitic rock are quartz, K-feldspar, plagioclase and biotite. Black tourmaline is irregularly distributed. Tourmaline occurs as primary, zoned, prismatic, euhedral crystals in aplite and pegmatite as well as radiating crystal groups and graphic intergrowths with quartz, albitic plagioclase and perthitic-graphic K-feldspar in pegmatite. A second generation of intergranular tourmaline is common. The mineralogy of miarolitic cavities reflects the primitive nature of these pegmatites. Only tourmaline and zoned garnet are locally abundant. Tourmaline needles and plumose aggregates are associated with the second generation of tourmaline. Other accessory phases are rare and the pocket paragenesis is very simple. No significant hydrothermal process of mineral alteration is developed.

2. Li-bearing dykes with complex asymmetric zoning – These dykes are characterized by Li-bearing accessory phases and a complex three-dimensional asymmetric zonation. They display a marked variation in grain size, in abundance and in textures of rock forming minerals. Pocket parageneses range from primitive to highly evolved types. The dykes belonging to this category are hosted by the porphyritic monzogranite and, exceptionally, along the contact of the leucogranite with basic thermometamorphic rocks. Usually, the rock consists of abundant plagioclase and quartz, K-feldspar and sparsely distributed biotite. Tourmaline is normally present as a rare accessory phase. It is concentrated in anhedral fracture-filling grains, preferentially associated with K-feldspar. The succession of colours in the polychrome tourmaline (from black, to green, yellow and pink) indicates a high degree of evolution in some pockets of the peripheral zones.

3. Li-bearing dykes with simple asymmetric zoning – These dykes are characterized by Li-bearing accessory phases and by a simple asymmetric zoning. The grain size, the abundance and the textures of rock-forming minerals change in the direction perpendicular to the walls. Usually, the pocket parageneses and the tourmaline colours are highly evolved. The dykes are hosted in the porphyritic monzogranite close to the contact with the country rocks.

4. Irregularly zoned to unzoned Li-bearing dykes – The dykes of this category are irregularly zoned to unzoned and have a random distribution of accessory phases. The host rocks are the hydrothermally altered mafic rocks and the hydrometamorphic rocks. Black tourmaline and white micas can occur along the exocontacts together with hydrothermal alteration products. The internal structure of these dykes ranges from irregularly distributed masses of aplitic and pegmatitic rocks with local concentrations of tourmaline and micas to a medium-grained rock with homogenous distribution of minerals. Miarolitic cavities are rare and even absent in some dykes.

5. Field Data

In the course of this thesis, 81 localities of aplite-pegmatite veins and dykes in different country rocks were visited (Fig. 24 + Tab. A1/Tab. A2 in the appendices). Altogether 159 samples were collected during a field trip between the 23th and 28th of October 2013. At the Chair of Resource Mineralogy, of the Montanuniversitaet Leoben, 27 thin sections and 9 thick sections were prepared for the petrographical and fluid inclusions research.

The studied outcrops, which are located near the Monte Capanne pluton's contact, belong to the late felsic products associated with the Monte Capanne pluton (see 2.c. Chapter 3 and Fig. 24).

5.1. Eastern part of Monte Capanne

The area around San Piero in Campo and Grotta d'Oggia is characterized by monzogranite, metasediment and serpentinite as country rocks. The aplite-pegmatite veins occur generally thin (0.1 to 1 m) (Fig. 13). Samples 57A, 59B, 60A, 64A, 65C and 67E refer to this area.

Fig. 13: Thin dykes within monzogranite at a quarry near San Piero in Campo (GPS: N 42°44'48.3'' E 10°12'31.7'')
(photos by R.J. Bakker, October 2013)

The dykes within metasediment are weathered and often washed-out (Fig. 14). At Grotta d'Oggia, some miarolitic dykes are rich in tourmaline and rich in minerals with gemstone quality, which is why mineral collectors excavated these dykes (Fig. 15).

Fig. 14: A pegmatitic dyke within metasediment (GPS: N 42°44'46.5'' E 10°12'44.4'')
(photo by R.J. Bakker, October 2013)

Fig. 15: Excavated dyke within monzogranite at Grotta d'Oggia (GPS: N 42°45'20.8'' E 10°12'55.2'')
(photo by R.J. Bakker, October 2013)

The studied locations near La Pila, Catri and San Illario are dominated by weathered monzogranite, serpentinite and by eroded magnesite as country rocks. Different thicknesses (0.5 to 200 cm) and zoning of different grain sizes are common (Fig. 16). Sample 72C, 75D, 85A and 0A are references in this area.

Fig. 16: Left photo: Dykes with different thicknesses and a tourmaline-rich vein in the centre within weathered monzogranite (GPS: N 42°46'20.4'' E 10°13'26.7''). Right photo: An unsymmetrical zoned dyke (GPS: N 42°46'04.9'' E 10°13'25.4'') (photos by R.J Bakker, October 2013)

5.2. North-eastern part of Monte Capanne

The north coast near Procchio is characterized by radiolarite and by a skarn. Therefore, marble and metamorphic lime with vesuvianite, wollastonite and diopside are common (Fig. 17). Samples 1J, 3A and 5B were collected in this area.

Fig. 17: A large aplitic dyke (on top) in contact with folded marble (left photo) and several dykes, which cut the folded marble (right photo) at Spiaggia Spartaia (photos by R.J. Bakker, October 2013)

5.3. Western part of Monte Capanne

The west coast of Elba Island near Pomonte and Chiessi is dominated by metasediment and serpentinite as country rocks (Fig. 18 + Fig. 19). The dykes occur in different thicknesses (0.5 to 20 m) and often display a weathering and a folding. Samples 9C and 17A are references and 15A displays an example of the often darkly Orano porphyry (see 3.a. Chapter 3 and Fig. 24) (Fig. 19).

Fig. 18: Left photo: The west coast of Elba with dykes (GPS: N 42°44'41.0'' E 10°07'19.7''). Right photo: An intersection of different generations of dykes within metasediment (GPS: N 42°44'40.3'' E 10°07'20.2'') (photos by R.J Bakker, October 2013)

Fig. 19: Right photo: A dyke within serpentinite (GPS: N 42°44'43.6'' E 10°07'11.1''). Right photo: Aplitic dyke on top, which belong to the Orano porphyry (GPS: N 42°45'52.8'' E 10°06'23.6'') (photos by R.J. Bakker, October 2013)

5.4. Mt. Calamita Formation

The studied outcrops, which are located in the eastern part of Elba Island in the Mt. Calamita Formation, namely in the Porto Azzurro Unit, are affected by the mostly covered (La Serra-) Porto Azzurro pluton. They belong to the acidic dykes of eastern Elba (see 4.c. Chapter 3 and Fig. 24) and consist of whitish dyke swarms, centimetric to metric in size (Fig. 20), and sometimes of blackish tourmaline-rich veins, up to 2 m in size (Fig. 21). Samples 23F, 25A, 29D and 35B are references of these dyke swarms, which intruded in the Mt. Calamita schists.

Fig. 20: Left photo: Parallel, whitish dyke swarms (GPS: N 42°16’09.5’’ E 10°24’31.8’’). Right photo: Dyke swarms at Spiaggia Istia (GPS: N 42°44’37.1’’ E 10°24’52.6’’) (photos by R.J. Bakker, October 2013)

Fig. 21: Tourmaline rich veins, with close-up (right photo) at Spiaggia Barbarossa (GPS: N 42°16'07.3'' E 10°24'23.8'') (photos by R.J. Bakker, October 2013)

Generally, the dykes and veins at the northern part of the Calamita peninsula are deformed and folded or show thinning, because of the transition zone near the Zuccale Fault (ZF) (Fig. 22).

Fig. 22: Right photo: Thrust of the hanging wall at the contact with the Zuccale Fault (ZF) (GPS: N 42°46'22.5'' E 10°25'07.7''). Left photo: Pegmatite at the contact with highly folded Calamita schist (GPS: N 42°43'50.5'' E 10°25'55.0'') (photos by R.J. Bakker, October 2013)

At the south-western part of the Calamita peninsula, dykes with coarse-grained, columnar, pink andalusite and dykes with magmatic flow textures and complicated zoning can be observed (Fig. 23).

Fig. 23: Left photo: Columnar pink andalusite enclosed in a white dyke near Ginepro. Right photo: Pegmatite with a magmatic flow texture, also near Ginepro (GPS: N 42°43'30.9'' E 10°26'03.6'') (photos by R.J. Bakker, October 2013)

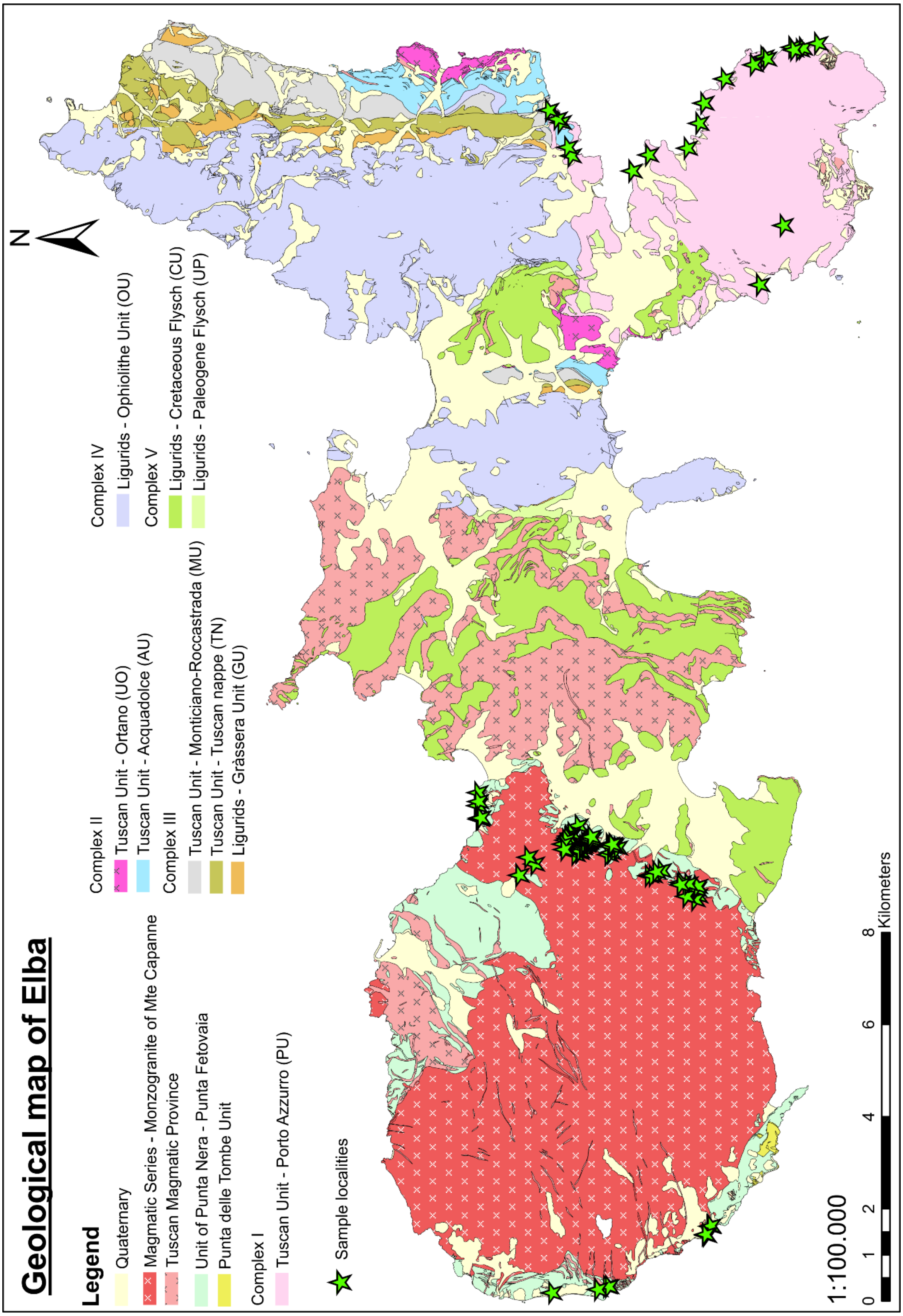

Fig. 24: Geological map of Elba with the localities of the studied samples, modified after Marinelli and Trevisan (1967) *and* Babbini et al. (2001). *Website:* Regione Toscana 2014

6. Petrography and mineral chemistry

6.1. Basic principles of the used methods

6.1.1. Raman Spectroscopy

The Raman spectroscopy uses the inelastic scattering of light to analyse vibrational and rotational modes of molecules (Raman scattering). According to the bonding of the sample and the primary light source, in this case a green laser beam with a specific wavelength of λ=532.02 nm and enough energy to shake molecules, the monochromatic light gains or loses energy (Fig. 25). For the loss, the light gives a pulse of energy to the molecule that starts to vibrate (Stokes scattering). If the light receives energy from an already vibrating molecule, it subsequently stops shaking (Anti-Stokes scattering). The energy-loss is most probable. The vibration modes depend on the symmetry of the molecules and is therefore specific and characteristic, and they cause a change in polarizability. The main effect is the Rayleigh scattering, while photons which are not absorbed by the sample are scattered back in an elastic way and do not change their wavelengths. A Stokes Raman spectrum is a plot of the intensity of the scattering vs. the energy loss, expressed in wavenumbers relative to the source ($\Delta\upsilon$ in cm^{-1}, the Raman shift), i.e. the changes in wavenumber compared to the incident light, which is only a very weak effect (Burke, E. A. J. 2001).

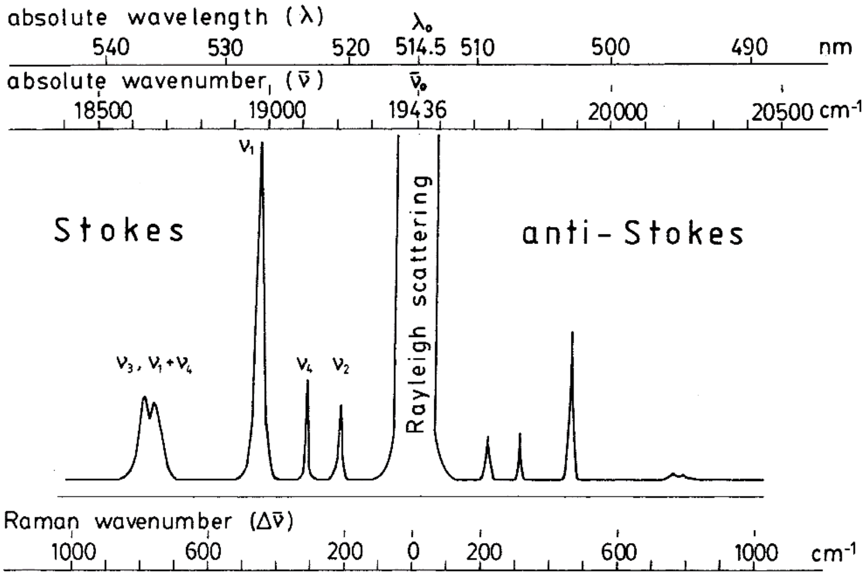

Fig. 25: The Raman effect of CCl_4, excited with 514.5 nm laser. Most photons of the incident light are elastically scattered, without energy change. Some photons gain or lose a small amount of energy by inelastic scattering (Stokes / Anti-Stokes); after Burke, E. A. J. (2001)

The measurements in this thesis were performed with a Jobin-Yvon LabRAM, combined with an Olympus BX40 microscope. The analyses were handled with the program LabSpec on a connected computer. The used Nd-YAG green laser had a wavelength of 532.02 nm and a power of 2 mW. Calibration of the Raman spectrometer was done by a silicon standard and polyethylene. The precision reproducibility of Raman analyses of fluid inclusions is usually better than 5%.

The minimum size of fluid inclusions for Raman analysis depends on many factors: the optical properties, the quality of the microscope system, the available laser power, the type of detector in the spectrometer, the density molar volume of the fluids, the depth of the inclusions within the sample and the background signal of the matrix. Even very broad and long inclusions may have a short third dimension, they can be very flat. Because of the relatively large vertical dimension of the laser focus up to several tens of micrometers, most of it will excite the matrix of the inclusion, not the inclusion itself. The Raman signal will be weak. For the same reason, all Raman peaks of the fluid components of all inclusions were measured without changing the location or the focus depth of the laser beam. Smaller inclusions near the surface of a sample will generally give a stronger Raman signal than larger inclusions at greater depths. For the N_2-bearing fluids, an optimum depth was chosen and a comparison measurement of the background was carried out for obtaining the maximum intensity of Raman peaks and avoiding contamination from the nitrogen in the air between objective and sample. Finally, the weak Raman scattering can be completely masked by fluorescence, which is several orders of magnitude stronger. Three features may cause fluorescence: the surface, the matrix mineral and/or the fluid inclusions. Several minerals are well known for their fluorescence, not only fluorite and tourmaline, but also plagioclase feldspar and sometimes even quartz. Cracks and fractures may prevent analysis altogether (Burke, E. A. J. 2001).

For the qualitative analysis with Raman in fluid inclusions, only the Δυ values of the characteristic peaks are necessary. Quantitative analysis of gaseous or supercritical inclusions is only possible if the spectral efficiency of the spectrometer (=instrumental factor, in this case $\xi=1$) and the Raman scattering efficiencies for the different components (=cross-sections; the σ's) are known (Tab. 1).

The relative proportions are calculated with the formula based on Placzek's polarizability theory:

$$x_i = \frac{\left(\frac{a}{\sigma \times \xi}\right)_i}{\sum_j \left(\frac{a}{\sigma \times \xi}\right)_j}$$

in which x_i, a, σ and ξ are, respectively, the molar fraction, the peak area, the Raman cross-section and the instrumental efficiency for component i. j represents the appropriate values for all components present in the inclusion as sum (Burke, E. A. J. 2001).

Tab. 1: Raman shifts (Δυ) and Raman scattering cross-sections (σ) of studied components in inclusions, modified after Burke, E. A. J. (2001)

Component	Phase	Δυ [cm^{-1}]	Rel. Intensity [%]	σ (514 nm)
CO_2	Liquid	1284	56	1
		1387	100	1.5
	Clathrate	1278	40	
		1381	100	
CH_4	Vapour	2917		7.5
	Clathrate	2904	100	
		2914	22	
N_2	Vapour	2330		1
		2291		
		2252		
H_2	Vapour	4129	12	2.3
		4146	15	2.3
		4158	100	2.3
		4163	14	2.3
H_20	Liquid	2900 - 3750		
	Ice	3148		

6.1.2. Microthermometry

The Microthermometry gives information about phase transitions like the melting and homogenization temperature. The melting temperature is defined as the point when a solid phase changes in a liquid phase. In contrast, the homogenization temperature illustrates the point when a liquid phase transits in a gas phase or a supercritical fluid. Hence, the so-called "heating-freezing" stage is heating up conductively and is combined with an optical microscope. Due to metastabilities during the cooling cycle, only temperatures during a heat cycle should be observed.

The measurements in this thesis were performed with a Linkam MDSG600 stage, combined with an Olympus BX60 microscope. In addition, the program LinkSys32 on a connected computer was used. The cooling of the stage occurred with liquid nitrogen. Calibration of the microthermometry was done by synthetic water inclusions ($T_m(H_2O)$ = 0.0°C, $T_h(H_2O)$ = 374.0°C) and synthetic CO_2 fluid inclusions ($T_m(CO_2)$ = -56.6°C).

The both side polished thick sections were solved with acetone from their specimen holder and only relevant areas were analysed.

A combination with the Raman spectroscopy allows the qualitative measurement and analyses of the fluid and gas phases of the different inclusions at different temperatures.

6.1.3. Electron microprobe analyser (EPMA)

The EPMA is a non-destructive analytical tool to determine the chemical composition of small samples up to a resolution of one micrometer. Therefore, a sample is bombarded with a monochromatic electron beam, which is emitting characteristic x-rays. In this manner, concentrations of elements from atomic number four (beryllium) to plutonium can be measured at levels as low as 100 ppm. The x-rays can be detected either with the element specific wavelength analysis (WDS = wavelength dispersive system) or with the element specific energy analysis (EDS = energy dispersive system). WDS spectrometers use the effect described by the Bragg's law that x-rays will be refracted at characteristic angles of the crystal lattices. The EDS is used for fast qualitative analyses, in which x-rays are registered as a function of their energy.

In the course of the investigation of tourmaline, the elements B, F, Na, Mg, Al, Si, K, Ca, Ti, Mn and Fe were analysed using a JEOL JXA-8200 operating in WDS and EDS mode, installed at the Eugen F. Stumpfl Electron-Microprobe-Laboratory of the Montanuniversitaet Leoben. The analyses were performed at 20 keV and 10 nA, using counting times as short as 20 and 10 s for peak and backgrounds, respectively (Tab. A11 in the appendices).

For the analyses of andalusite, biotite, garnet and cordierite the elements Mg, Na, Fe, Ca, Cr, Al, Si, Ti, K, Mn and for rutile the elements Mg, Nb, Sn, Cr, Ti, Al, Zr, W, Fe, Mn, Ta and V were analysed (Tab. A12, Tab. A13, Tab. A14 in the appendices).

Columbite analyses were performed at 30 keV and 40 nA, using counting times as short as 50 and 25 s for peak and backgrounds for the elements Nb and U. In addition, the elements Si, Y, Ti, Ta, Ca, Mn, Sn, Fe, Sc, W, Zr and Hf with counting times as short as 20 and 10 s for peak and backgrounds were analysed in the columbite samples. The spectra of the HREE (heavy rare earth elements) is based on semi-quantitative analyses, which were performed without standards due to the very small size of the grains and the protracted calibration.

The details of the quantitative analyses are listed in Tab. 2.

Tab. 2: Details of the quantitative analyses

Analysis	Order	Element	Crystal	Standard	Detection Limit (ppm)
Tourmaline	1	F	LDE1	FphlogopiteLB	552
	2	Na	TAP	41_K_sanidKE12	173
	3	Ca	PETJ	WollastLB10Mu	143
	4	Fe	LIFH	IlmeniteLB15Kv	188
	5	K	PETH	AdularLB	64
	6	B	LDEB	49BNLB	1302
	7	Mg	TAP	34olivineLB	116
	8	Si	PETJ	AdularLB	162
	9	Ti	LIFH	40_K_Rutil_KE5	255
	10	Al	TAP	Labradorit17LB	118
	11	Mn	LIFH	RhodLB	172
Andalusite, biotite, garnet, cordierite	1	Mg	TAP	34olivineLB	89
	2	Na	TAP	SpisanidineLB	190
	3	Fe	LIF	34olivineLB	2034
	4	Ca	PETH	WollastLB10Mu	84
	5	Cr	LIFH	Cr2O3LB	244
	6	Al	TAP	AdularLB	124
	7	Si	PETJ	Labradorit17LB	278
	8	Ti	LIFH	40_K_RutilKE8	247
	9	K	PETJ	SpisanidineLB	134
	10	Mn	LIFH	RhodLB	212
Rutile	1	Mg	TAP	27SPI_AM	28
	2	Nb	PETJ	Nbmet10020kv	159
	3	Sn	PETJ	SPIcassiterite	130
	4	Cr	LIFH	20Crocoite	49
	5	Ti	LIFH	40RutileLB20KV	126
	6	Al	TAP	albLB50kv20na	32
	7	Zr	PETJ	47ZircLB20KV	142
	8	W	LIFH	⍰Wmet	161
	9	Fe	LIFH	ChpNWM20KvLB	78
	10	Mn	PETJ	RhodLB20Kv	222
	11	Ta	LIFH	Tamet	258
	12	V	LIFH	Vmet	0
Columbite	1	Si	TAP	29kaers	137
	2	Y	PETJ	51SpiLB30Kv	325
	3	Ti	PETJ	SPIRutile	70
	4	Nb	PETH	ColtanMS139	77
	5	Ta	LIFH	ColtanMS139	203
	6	Ca	PETJ	29kaers	50
	7	U	PETH	Uo230kvLb	67
	8	Mn	LIFH	ColtanMS139	51
	9	Sn	PETJ	12_Cassiterite	128
	10	Fe	LIFH	ColtanMS139	59
	11	Sc	PETJ	Sc10030kv	47
	12	W	LIFH	ColtanMS139_W	320
	13	Zr	PETJ	Zr	150
	14	Hf	LIFH	Hf	130

6.2. Results and description of the petrography and mineral chemistry

In summary, all the studied dykes of Elba Island display a grey to light-grey colour and a fine-grained-aplitic to medium-grained-porphyritic texture. Portions with an abundance of tourmaline and tourmaline-rich veins appear brownish or black. Some dykes are symmetric with straightened or skeletal tourmaline crystals. Zoned dykes with fine- and coarse-grained crystals and zones with more or less tourmaline crystals are common (Fig. 26) (Tab. A1 + Tab. A2 in the appendices).

Fig. 26: Dykes with an abundance of skeletal tourmaline and zoning, from Spiaggio Pauline, Elba Island (photo by R.J. Bakker, October 2013)

The pegmatitic dykes belonging to the first generation of veins show an average dip direction of 219 degrees and an average dip of 57 degrees. Their thickness varies from 0.5 cm to 3.5 m.

The mean thickness is 96 cm. Because of this wide range, it is possible that some of these dykes also represent a second or a third generation. Generally, the first generation of dykes dip at middle-high angle respect to the country rock.

The second generation of dykes usually fills fractures within the country rock. In addition, they often crosscut dykes belonging to the first generation. They show an average dip direction of 167 degrees and an average dip of 44 degrees. Some of these dykes are deformed and were formed during escape. The thickness is variable from 3 cm to 30 cm. Mean thickness is 14 cm.

The third generation of dykes or the tourmaline-rich veins also fills fractures and cracks within the country rock (Fig. 26) and crosscuts dykes of the first and of the second generation. They often dip at high angles (80 degrees up to vertical) and their thickness varies from 0.5 cm to 10 cm with a mean thickness of 3.6 cm. Sometimes these dykes appear as a network of a possible shear movement. Pure tourmaline veins with brownish or black colour represent a very late stage of the intrusions, when nearly Boron-pure fluids interact with the country rock.

6.2.1. Sample 57 A

This sample within monzogranite was collected near the quarry of San Piero in Campo. Although the bedrock shows many tourmaline "suns", the thin section does only include tourmaline as an accessory mineral. It displays a microcrystalline texture and a coarse-grained band (Fig. 27) with quartz and feldspar (especially K-feldspar) as main components and rare mica (especially muscovite), garnet and cordierite. Opaque minerals and bluish tourmaline are accessory.

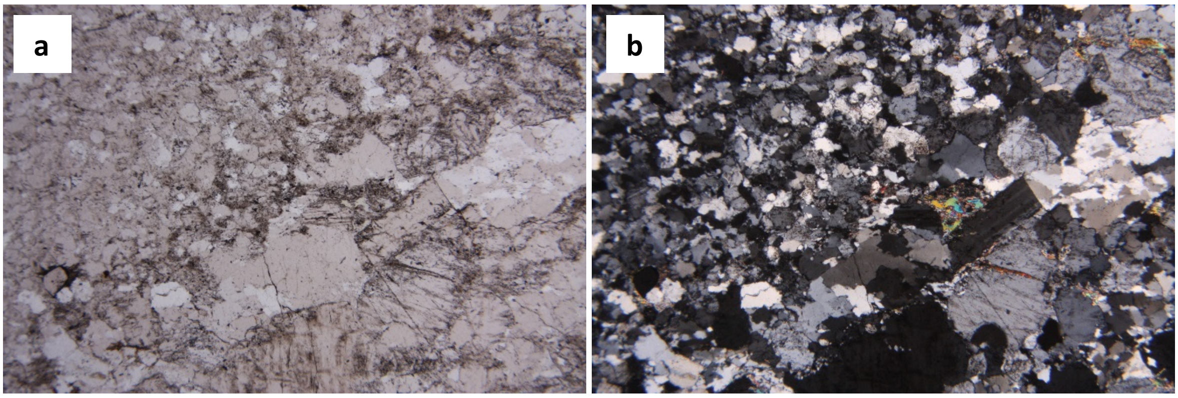

Fig. 27: Transmitted light image (a) and cross-polarized light image (b) of the microcrystalline texture and a coarse-grained band with quartz, feldspar and mica (length of the images 4 mm)

Quartz as mineral phase makes up nearly 80% of the whole rock volume and is represented by almost rounded, multiple-fractured, crystals sometimes showing embayments. The feldspar crystals are generally sub-idiomorphic whereas quartz is intercrystalline. K-feldspar is sometimes included in quartz. The plagioclase crystals are generally subhedral to rounded and show albite-carlsbad and albite twinning. In addition, feldspars often exhibit sericitic alteration.

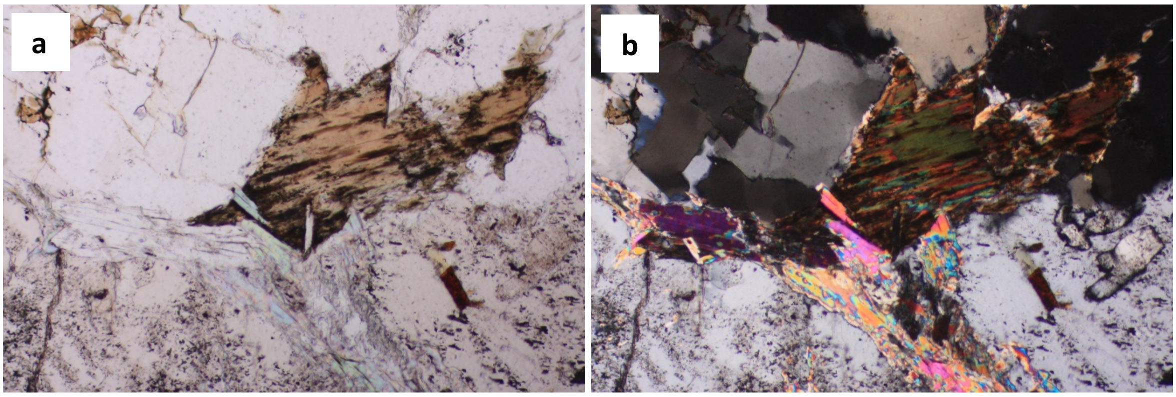

Fig. 28: Transmitted light image (a) and cross-polarized light image (b) of scattered micas (length of the images 1 mm)

Micas are represented by coarse-grained muscovite or as replacement at grain boundaries as well as by biotite (Fig. 28). Biotite is often altered and chloritized (Fig. 29). In this thin section, garnet is represented by almandine and pyrope. The euhedral garnet crystals display a high relief and isotropy. Some inclusions are found in these crystals, which are identified as solid quartz inclusions (Fig. 29).

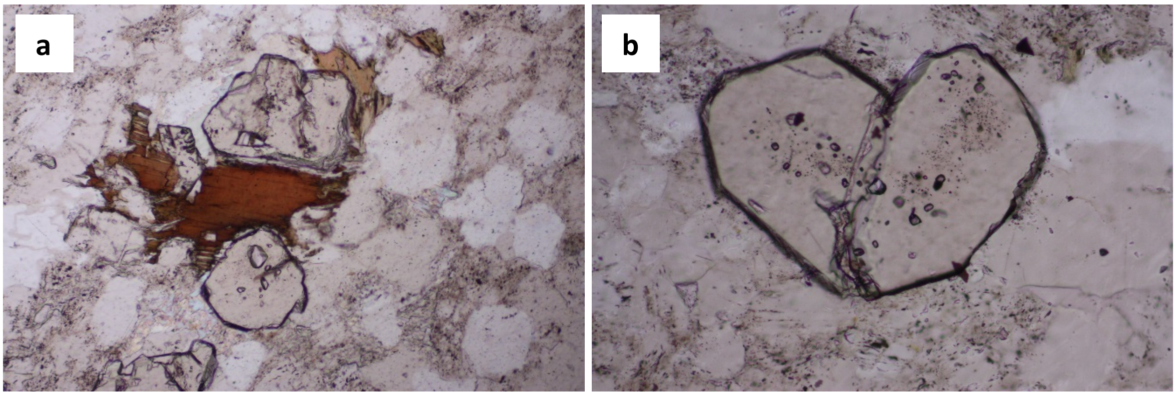

Fig. 29: Transmitted light image of (a) garnet and chloritized biotite (length of the image 1 mm) and of (b) garnet with quartz inclusions (length of the image 0.2 mm)

Cordierites appear as large (up to 1 mm in size), greenish crystals, which are more intensely altered than the other mineral phases due to pinitisation (Fig. 30).

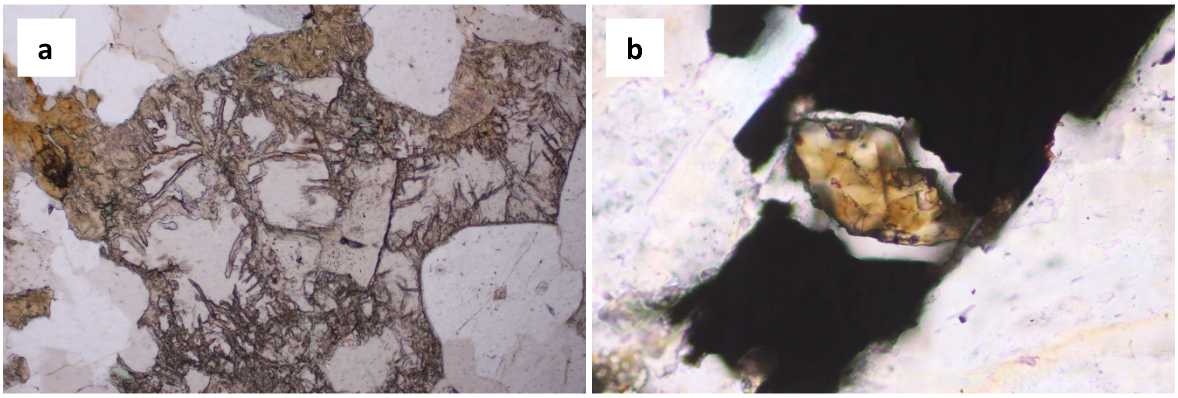

Fig. 30: Transmitted light image of (a) altered cordierite (length of the image 1 mm) and of (b) bright rutile between dark anatase crystals (length of the image 0.2 mm)

Raman spectroscopy allowed a classification of (1) zircon within some biotites with radioactive rims, (2) anatase displayed as tiny, dark crystals and (3) rutile as tiny, bright crystals (Fig. 30) (Fig. A1 in the appendices).

6.2.2. Sample 59 B

This sample was collected along the road to San Piero in Campo within metasediment. The thin section represents a small main vein with brownish green tourmalines going through green micas (Fig. 31). Another deviating vein is also visible as a second generation with small bluish tourmalines. Both veins consist of medium-grained quartz, feldspar (especially K-feldspar), tourmaline, rare mica, garnet and apatite. Rutile and a few opaque minerals are also accessory.

Quartz crystals are often recrystallized and multiple-fractured and K-feldspar is often included in quartz. The generally subhedral feldspar crystals show albite-carlsbad and albite twinning and exhibit sericitic alteration.

In the main vein, the short prismatic tourmaline crystals are olive-green (schorl) with a distinctive pleochroism from brownish green to dark greenish blue. In the deviating vein, the bluish rounded crystals display a distinctive pleochroism from bright brown to greenish blue. Occasionally, tourmaline is altered or shows fascicular aggregates.

Fig. 31: Scanned thin section 59B (dimensions: 2.8 x 4.8 cm)

Apatite as colourless crystals with a high relief shows negative shaped fluid inclusions with gas-rich bubbles (Fig. 32). Mica as a replacement mineral is common and often fills cracks and altered minerals as a brownish mass. Monazite – (Ce), $CePO_4$, as greenish or colourless crystals with a high relief, was also found (Fig. 32). Garnet crystals are isotropic with a high relief.

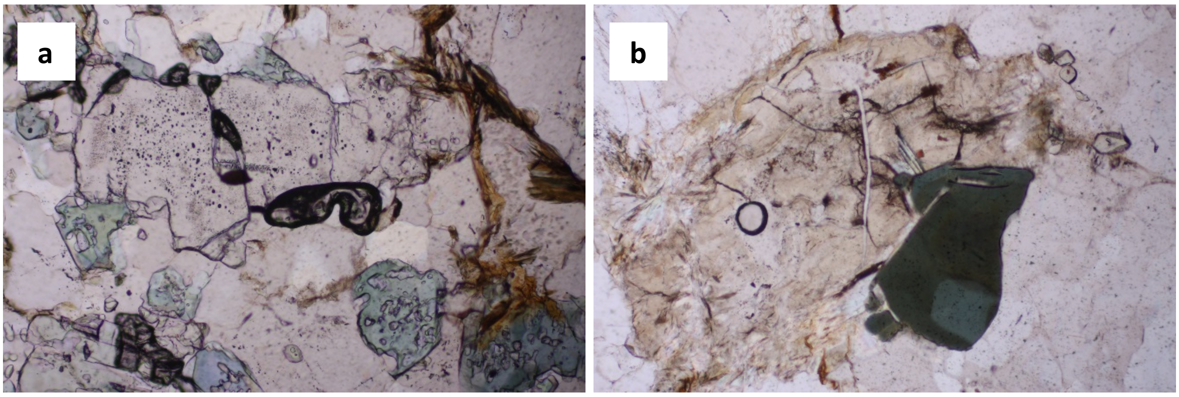

Fig. 32: Transmitted light image (a) of apatite, dark rutiles, tourmalines, mica and quartz, and transmitted light image (b) of mica as a brownish mass, tourmaline and small monazite crystals on the right (length of the images 1 mm)

Raman spectroscopy evidenced the presence of cassiterite, SnO_2 (Fig. A2 in the appendices) and rutile, grown together in a single crystal (Fig. 33) and of hematite as an opaque mineral (Fig. 34).

The columnar green, bluish mica (Fig. 35) as part of the country rock is conspicuous. Raman spectroscopy allowed a classification of fluorophlogopite $KMg_3(AlSi_3)O_{10}F_2$, a fluorine mica. The weak colourful prismatic crystals, up to 2 mm in size, are scattered and show the typical cross-polarized light image of mica.

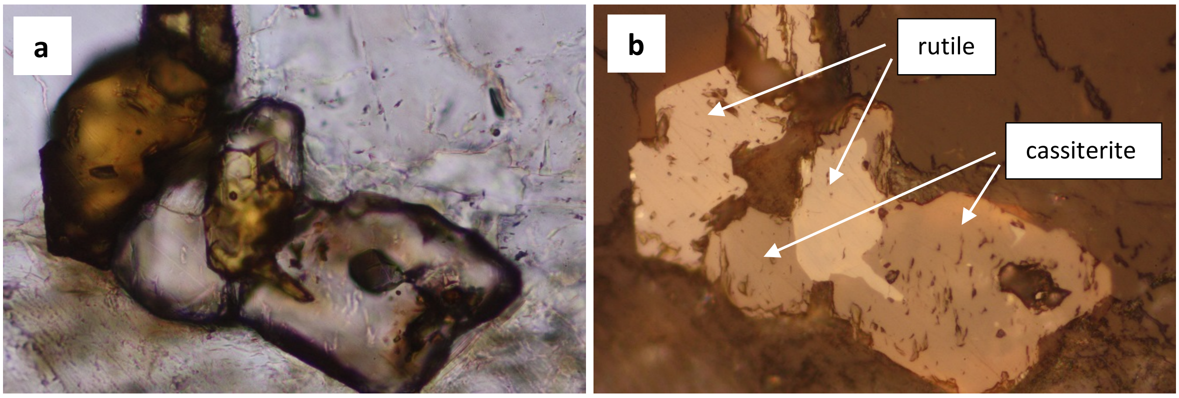

Fig. 33: Transmitted light image (a) and reflected light image (b) of cassiterite and rutile as one crystal (length of the images 0.2 mm)

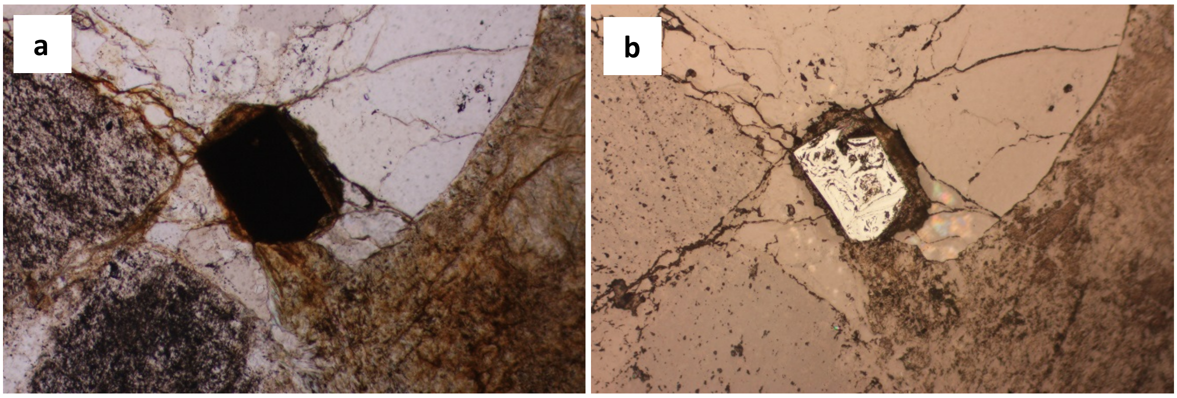

Fig. 34: Transmitted light image (a) and reflected light image (b) of hematite (length of the images 1 mm)

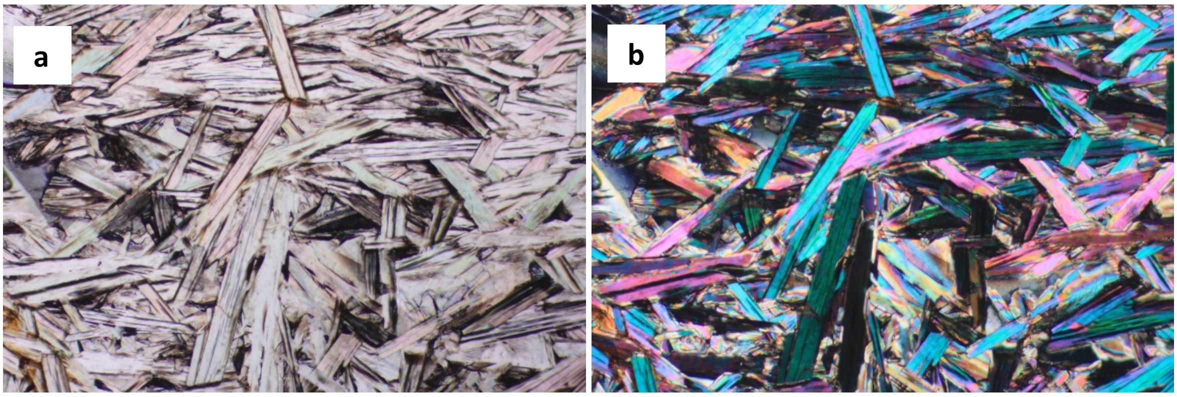

Fig. 35: Transmitted light image (a) and cross-polarized light image (b) of fluorophlogopite (length of the images 1 mm)

6.2.3. Sample 60 A

60A was also collected along the road to San Piero in Campo within metasediment. Medium-grained quartz, feldspar, pink andalusite and tourmaline are main components. Mica fills cracks and altered grains as a secondary mineral or fills the lamination of feldspars as coarse crystals (Fig. 36).

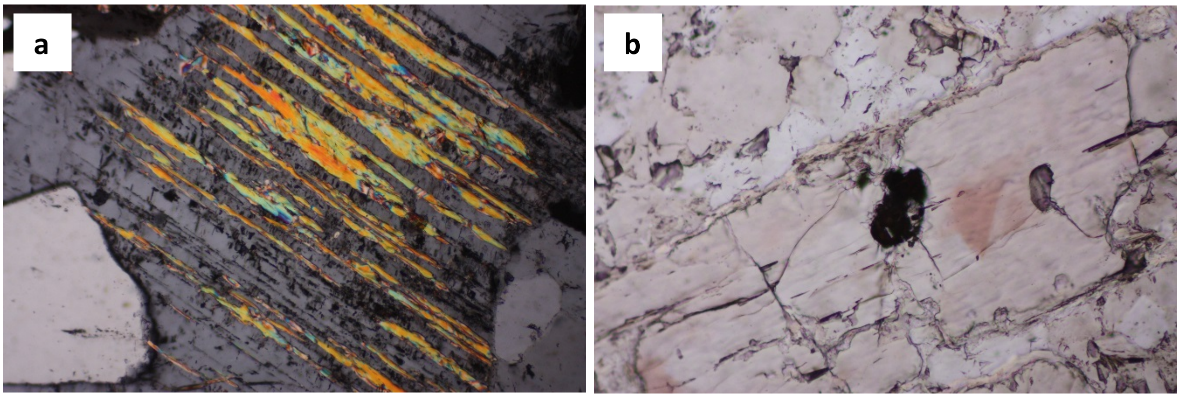

Fig. 36: Cross-polarized light image (a) of mica along the twinning of feldspar and transmitted light image (b) of andalusite with rutile in the core (length of the images 0.5 mm)

Quartz appears as recrystallized, polycrystalline and multiple-fractured. Feldspar crystals (especially plagioclase), up to 2 mm in size, are generally subhedral, altered and often display polysynthetic or albite twinning and sericitic alteration (Fig. 37). The large andalusite crystals (up to 3 mm in size) are columnar or zoned, where the noticeable pink colour indicates zones of different element composition (Fig. 36 + Fig. 37). The prismatic crystals (the lateral cut shows squares) display a weak pleochroism from pale to pink and a moderate high relief. Occasionally, the rims of andalusite show sericitic alteration and rutiles can be found inside the core of andalusite (Fig. 36).

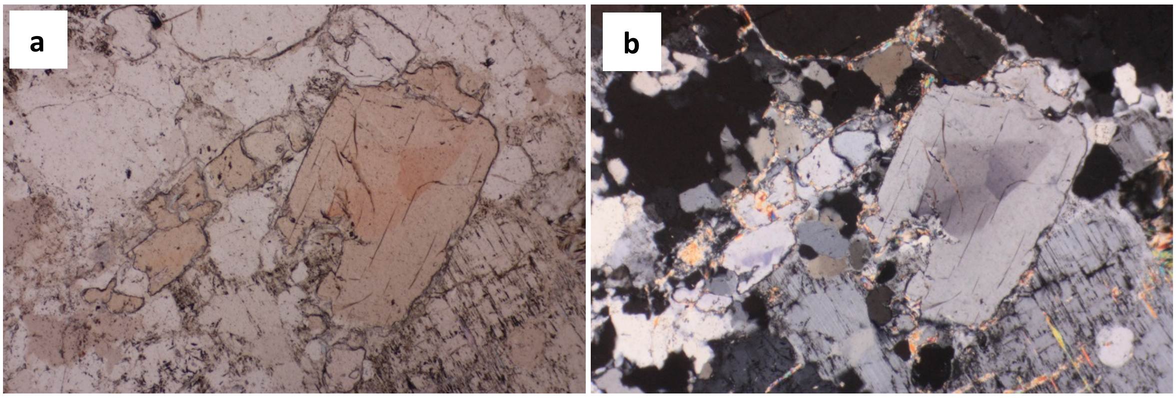

Fig. 37: Transmitted light image (a) and cross-polarized light image (b) of pink andalusite, feldspar and quartz (length of the images 2 mm)

Tourmaline crystals occur olive-green to brown prismatic, sometimes boudinated in a preferred orientation or zoned, and with a distinctive pleochroism from pale green to dark green (Fig. 38). The idiomorphic grains have sizes up to 4 mm and lateral cuts display typical triangles. Raman spectroscopy evidenced the presence of hematite and several dark rutiles.

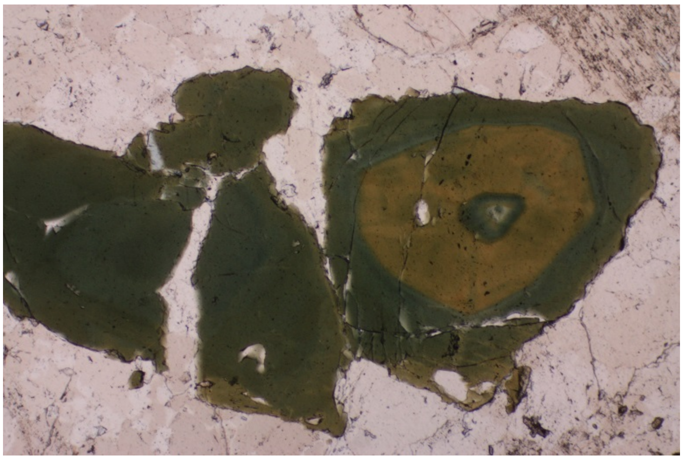

Fig. 38: Transmitted light image of tourmaline (length of the image 2 mm)

6.2.4. Sample 64 A

This sample was collected near the mine Grotta d'Oggia within monzogranite. The thin section represents two specifiable areas. One area consists of two large feldspar crystals, up to 2 cm in size, and the other area consists of a microcrystalline framework of feldspar (especially plagioclase) as well as rare quartz, andalusite and tourmaline (Fig. 39).

The feldspar mineral phase makes up nearly 70-75% of the whole thin section. The two crystals at the bottom of the thin section are albite crystals. Some tiny, dark rutile crystals can also be found inside albite. The microcrystalline framework evidences some deformation and secondary processes. Therefore, the pink andalusite shows irregular fissures and the small bluish tourmaline crystals are anhedral and fractured.

Fig. 39: Scanned thin section 64A with large feldspar crystals at the bottom (dimensions: 2.8 x 4.8 cm)

Quartz displays two different generations of fluid inclusions (Fig. 40). While irregular, larger inclusions can be found along vertical traces, regular, small inclusions can be found in horizontal traces.

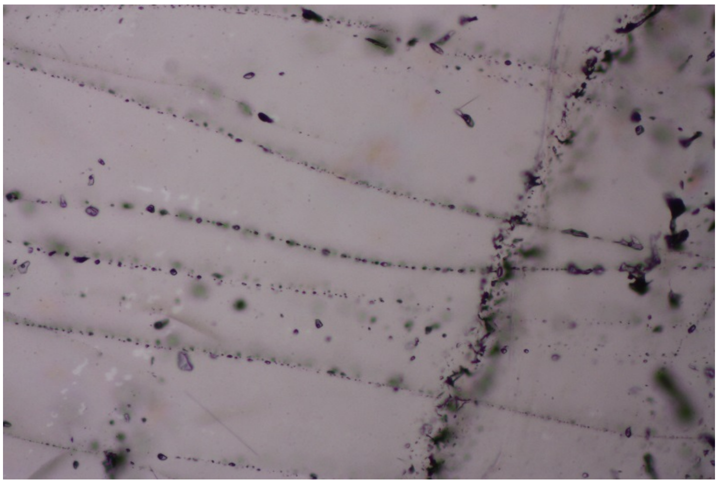

Fig. 40: Fluid inclusions in quartz (length of the image 0.5 mm)

6.2.5. Sample 65 C

Sample 65C was collected at the mine Grotta d'Oggia within monzogranite. The thin section displays a symmetrical zoning with zones of coarse-grained quartz, feldspar, tourmaline and zones of fine-grained quartz, feldspar and tourmaline (Fig. 41). Mica is a replacement mineral or occurs with small grains as Biotite. Opaque minerals are accessory.

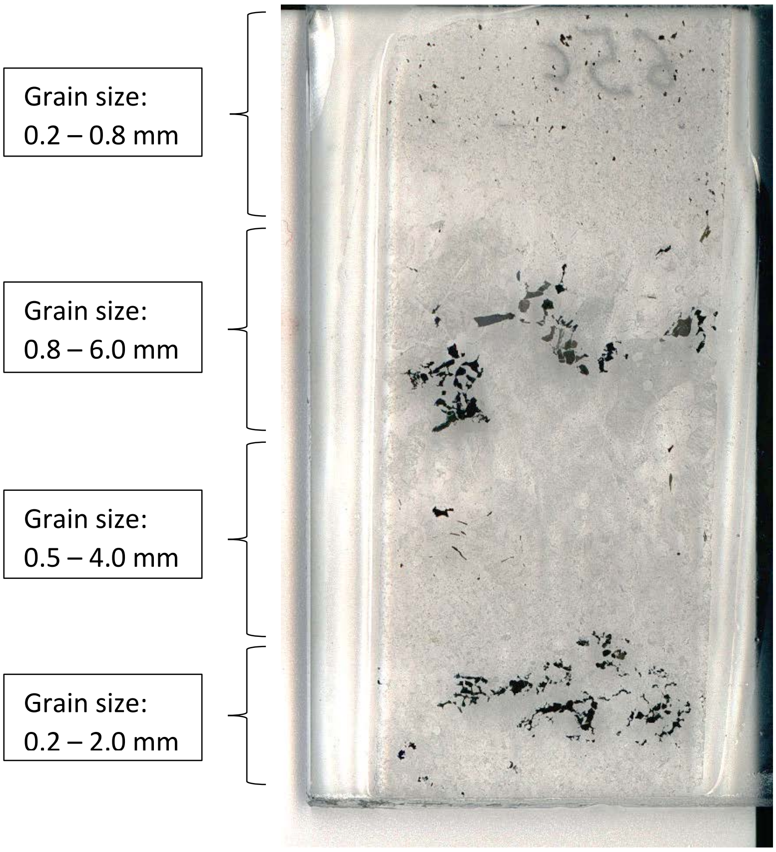

Fig. 41: Scanned thin section 65C with different grain sizes of tourmaline, quartz, feldspar and biotite (dimensions: 2.8 x 4.8 cm)

Quartz is represented as almost rounded, polycrystalline crystals and feldspar crystals are generally subhedral (large single-crystals) or hypidiomorph (especially plagioclase). Biotite with its distinctive pleochroism from bright brown to greenish blackish brown displays single, elongated, brownish crystals (Fig. 42). The olive-green, bluish tourmaline crystals are prismatic, up to 6 mm in size, sometimes zoned or small and irregularly shaped (Fig. 42). Feldspars (especially K-feldspars) are often perthitic and biotite is sometimes altered and chloritized. Raman spectroscopy allowed the classification of several tiny, dark rutiles.

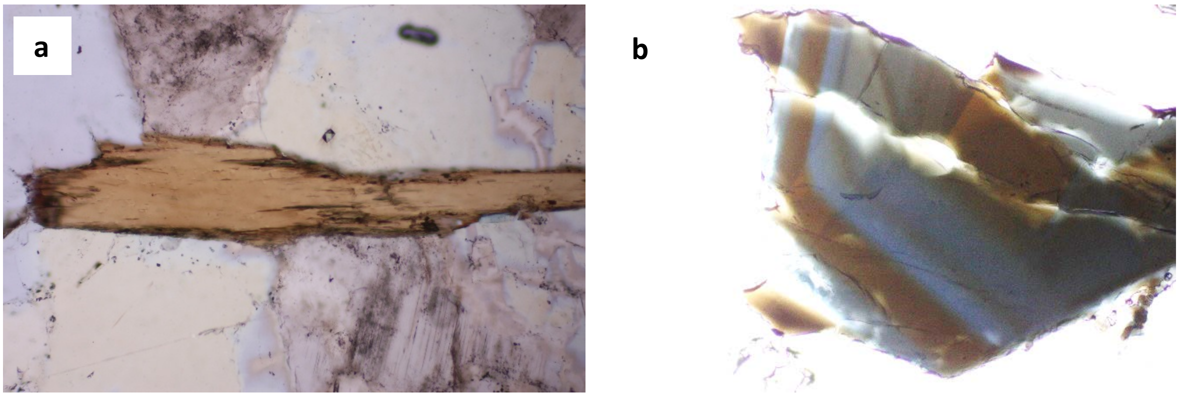

Fig. 42: Transmitted light image (a) of elongated, brownish biotite and transmitted light image (b) of zoned tourmaline (length of the images 1 mm)

6.2.6. Sample 67 E

67E was collected near the mine Grotta d'Oggia within metasediment. Main components are coarse-grained quartz, feldspar and pink andalusite. Sericite and coarse-grained mica can be found at the edge of feldspar crystals or along cracks in single crystals. Cordierite and opaque minerals are accessory. Quartz is represented by polycrystalline, multiple-fractured crystals and feldspar (especially albite) is represented by subhedral, altered crystals often with polysynthetic or albite twinning.

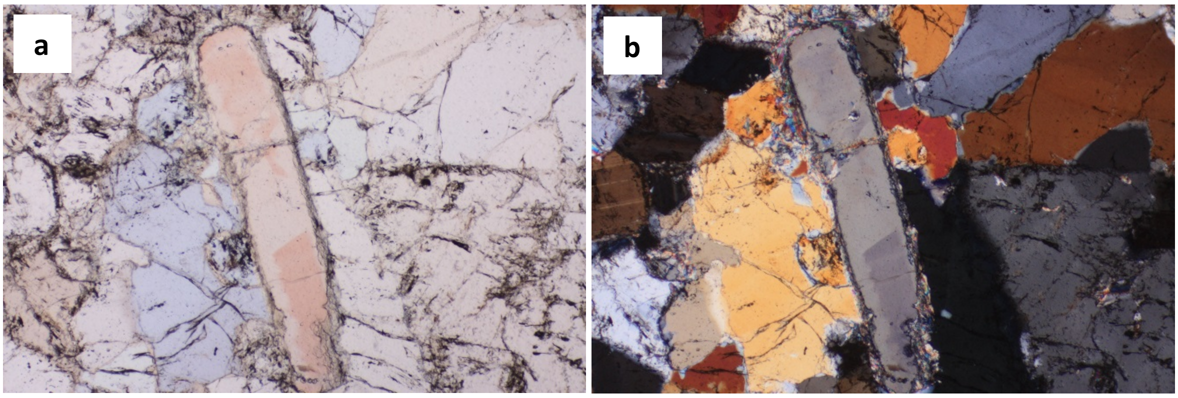

Fig. 43: Transmitted light image (a) and cross-polarized light image (b) of pink zoned andalusite and quartz (length of the images 2 mm)

The andalusite crystals are large (up to 3 mm in size), columnar or square in lateral cuts, and often display a pink zoning due to different element composition or sericitic alteration (Fig. 43). Cordierite appears as large (up to 1 mm in size), greenish crystals, which are partly transformed and show pinitisation and therefore are more intensely altered than the other mineral phases (Fig. 44).

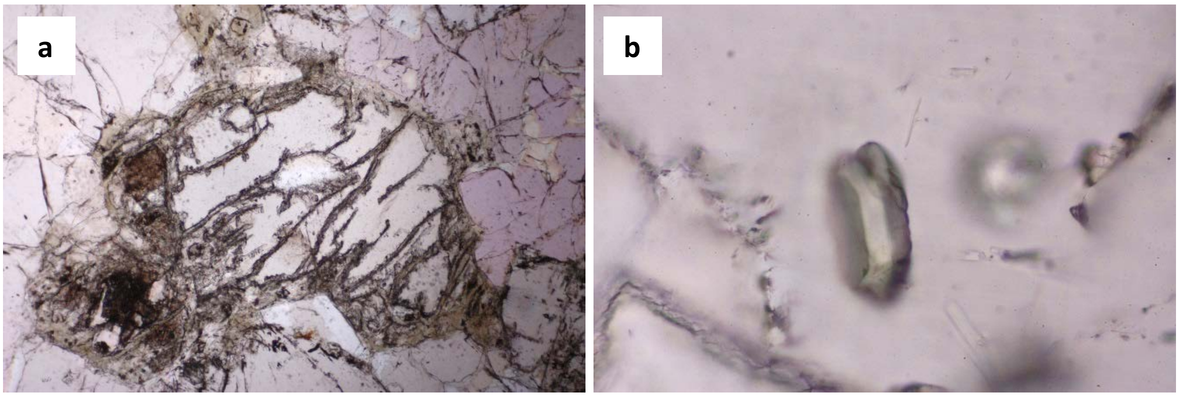

Fig. 44: Transmitted light image (a) of highly altered cordierite (length of the image 2 mm) and transmitted light image (b) of monazite (length of the image 0.2 mm)

Raman spectroscopy allowed the classification of (1) tiny brownish to blackish rutiles, (2) xenotime, YPO_4 and monazite – (Ce), $CePO_4$, as greenish greyish columnar crystals (Fig. 44) and (3) colourless zircon with a high relief (Fig. 45) (Fig. A3 in the appendices).

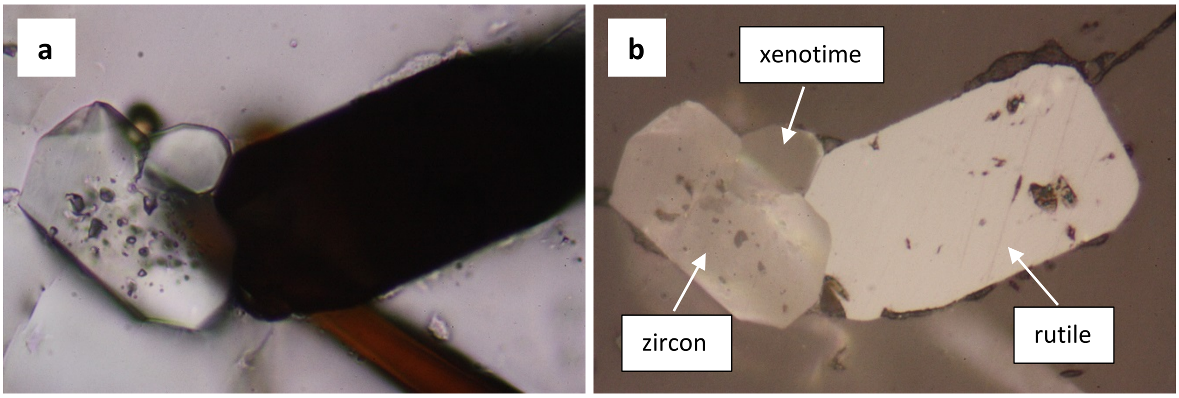

Fig. 45: Transmitted light image (a) and reflected light image (b) of rutile, zircon and xenotime (length of the images 0.1 mm)

6.2.7. Sample 72 C

This sample was collected near La Pila, Catri, within serpentinite. Middle-grained quartz, coarse-grained pink andalusite, feldspar and cordierite are main components (Fig. 46). Fibrous sillimanite, on grain boundaries or on grains, tourmaline and opaque minerals are accessory.

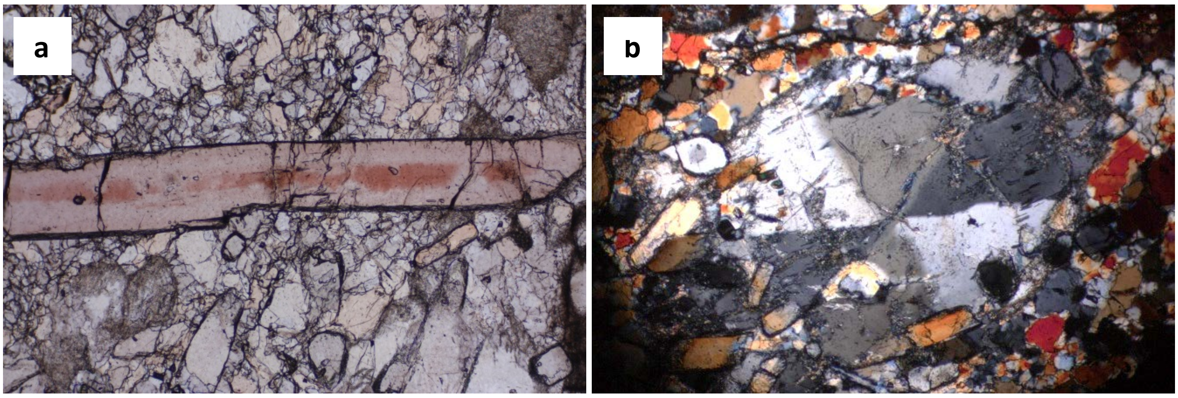

Fig. 46: Transmitted light image (a) of pink zoned andalusite, quartz and cross-polarized light image (b) of cordierite, quartz (length of the images 2 mm)

Quartz crystals are recrystallized, polycrystalline and smaller than the other components. Feldspars (especially oligoclase) are altered and perthitic. The large (up to 5 mm in size) idiomorphic, prismatic, at lateral cuts squarish, andalusite crystals make up to 25% of the whole thin section, which displays a porphyritic texture (Fig. 46). The long axes of the andalusite crystals have a preferred orientation and some crystals are stretched or even boudinated in a direction parallel to this preferred orientation of andalusite crystals in general (Fig. 47). This stretching lineation evidences a magmatic flow direction due to a magmatic deformation.

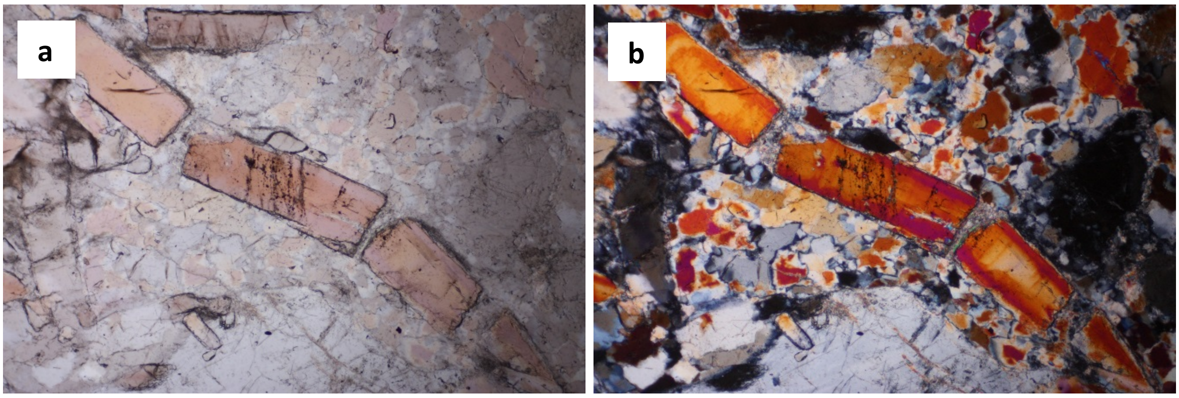

Fig. 47: Transmitted light image (a) and cross-polarized light image (b) of a boudinated pink andalusite crystal with melting inclusions (length of the images 2 mm)

In addition, andalusite shows a weak pleochroism and a zoning of pink colour in the core and a pale red in the rim as well as a high relief compared to the other components (Fig. 46). Often melting inclusions, made of mica and quartz and enclosed diaspore and zircon along traces, can be found perpendicular to the stretching lineation, which also evidence a magmatic flow (Fig. 47).

Tourmaline crystals are greenish and bluish with a distinctive pleochroism from bright greenish brown to dark blue, and are short prismatic, zoned and also stretched or boudinated in the same direction as andalusite (Fig. 48). The bounded cordierite crystals are colourless and more intensely altered than the other minerals due to pinitisation. They display typical psudohexagonal twinning (Fig. 46) and pleochroic halos caused by zircon (Fig. 48). Sillimanite occurs fibrous as a secondary mineral. Raman spectroscopy allowed the classification of dark rutile crystals and xenotime (Fig. A4 in the appendices).

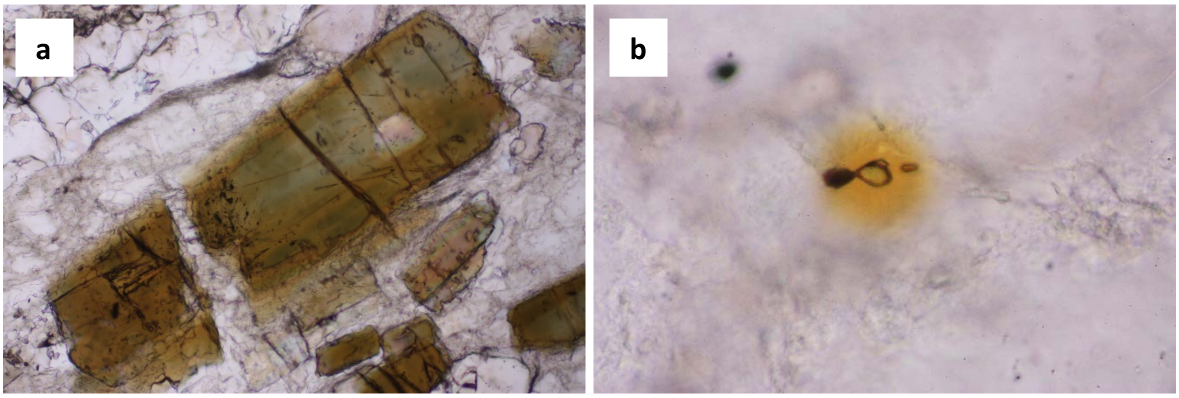

Fig. 48: Transmitted light image (a) of a boudinated tourmaline crystal (length of the image 1 mm) and transmitted light image (b) of a pleochroic halo around zircon enclosed in cordierite (length of the image 0.2 mm)

6.2.8. Sample 75 D

Sample 75D was collected near Catri within monzogranite. The thin section displays a zoning of microcrystalline framework, a zone of medium-grained quartz, feldspar, apatite with coarse-grained tourmaline and a zone of coarse-grained K-feldspar and quartz (Fig. 49 + Fig. 50).

Quartz is represented by polycrystalline, rounded to multiple-fractured crystals. Feldspar crystals are large (up to 8 mm in size on the top of the thin section) and subhedral with albite and albite-carlsbad twinning and quartz is often included in feldspar (Fig. 50). Feldspars are sometimes full of inclusions (fluid inclusions and quartz), so they look like they were highly altered (Fig. 51). Apatite (Raman spectroscopy allowed the classification of fluorapatite) was only found in the middle band of the thin section and the colourless six corners crystals show a high relief (Fig. 51). Tourmaline shows brownish, big single-crystals (up to 8 mm in size) and distinctive pleochroism from bright brown to dark brown (Fig. 49). The microcrystalline framework consists of quartz, feldspar and faint, scattered biotite and anatase as an accessory mineral.

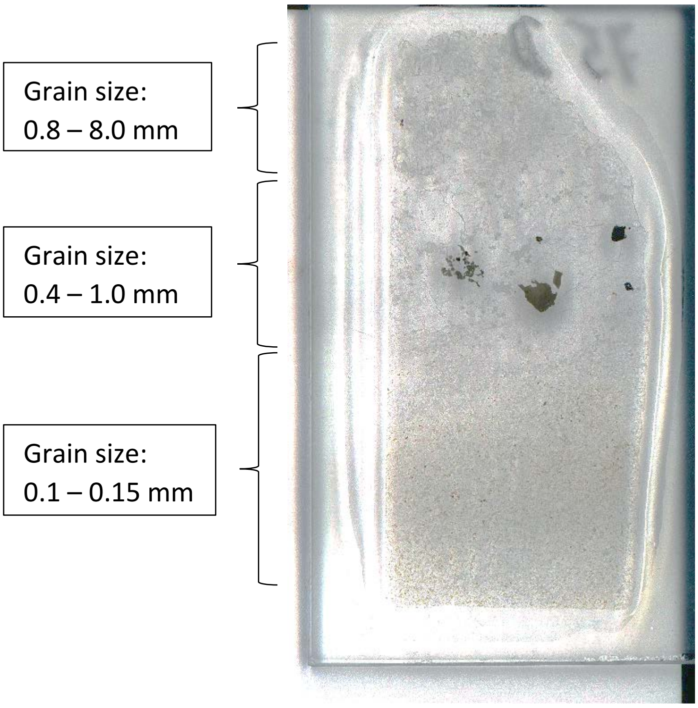

Fig. 49: Scanned thin section 75D with zoning of different grain sizes (dimensions: 2.8 x 4.8 cm)

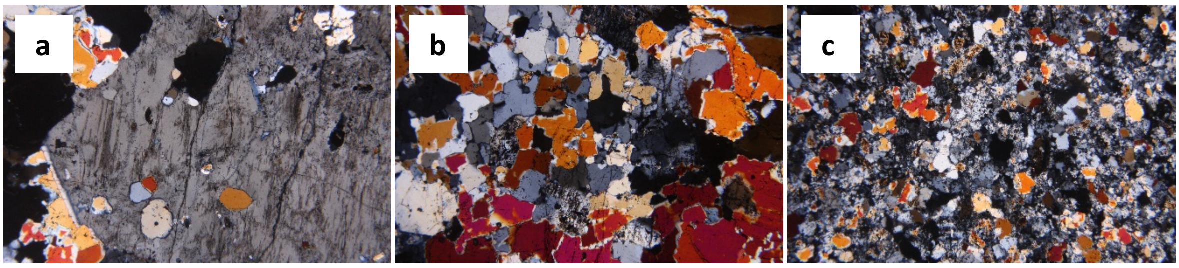

Fig. 50: Cross-polarized images of (a) the coarse zone with large K-feldspars, (b) of the zone on the middle of the thin section and (c) of the microcrystalline framework (length of the images 4 mm)

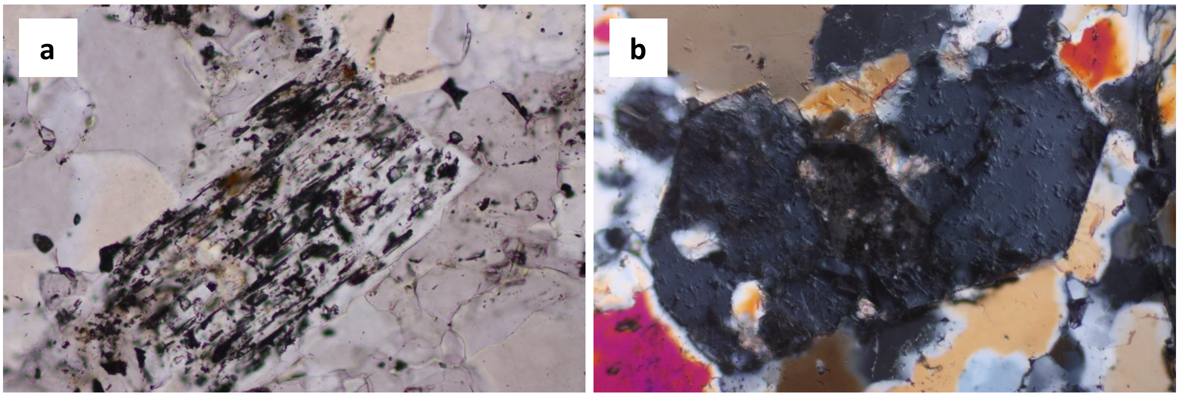

Fig. 51: Transmitted light image (a) of feldspar with inclusions (length of the image 0.5 mm) and cross-polarized image (b) of fluorapatite (length of the image 1 mm)

Fluid inclusions in plagioclase are often irregular and contain N_2 and small amounts of CH_4 and carbonates (Fig. 52). The fluid inclusions in tourmaline are typically elongated, contain CO_2 and sometimes borate crystals (Fig. 52). Plagioclase is often enclosed in tourmaline, which is why tourmaline was generated after plagioclase. In addition, melting inclusions with quartz occur in tourmaline. Quartz also displays fluid inclusions (Fig. 53).

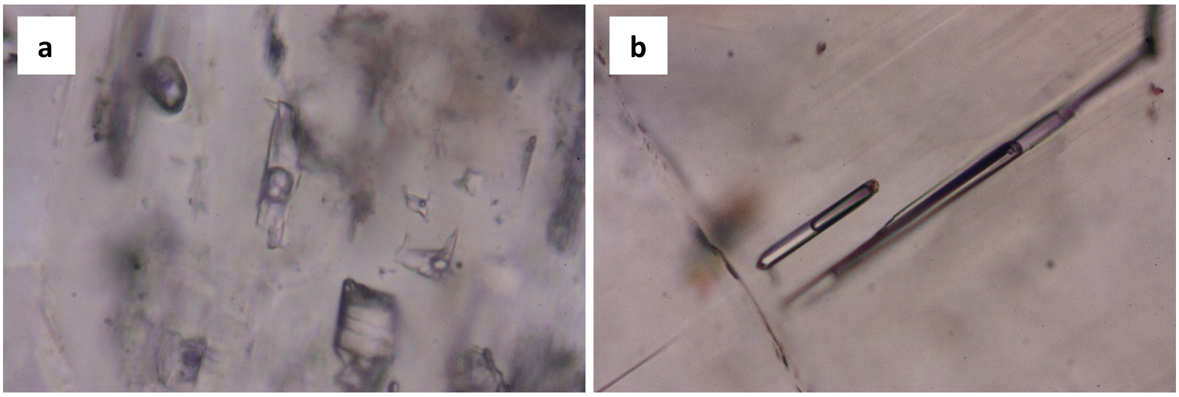

Fig. 52: Transmitted light image (a) of fluid inclusions in plagioclase (length of the image 0.1 mm) and transmitted light image (b) of elongated fluid inclusions in tourmaline (length of the image 0.2 mm)

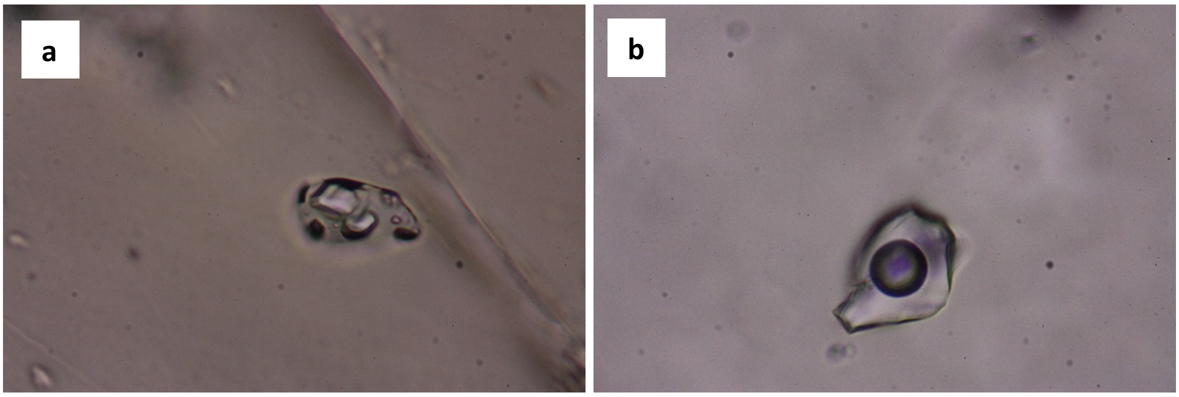

Fig. 53: Transmitted light image (a) of melting inclusions in tourmaline and transmitted light image (b) of a fluid inclusion in quartz (length of the images 0.1 mm)

6.2.9. Sample 85 A

This sample was collected near Catri within serpentinite. The thin section represents a composition of two large quartz crystals (up to 20 mm in size) on the top, a large feldspar crystal (up to 15 mm in size) on the bottom and a few tourmaline crystals up to 1.8 mm in diameter (Fig. 54).

Fig. 54: Scanned thin section 85A with quartz, feldspar and tourmaline (dimensions: 2.8 x 4.8 cm)

The two quartz crystals and the feldspar crystal (albite) are jointed and show cracks and traces of fluid inclusions (Fig. 55). Feldspars display a strong alteration. The tourmaline occurs zoned and olive-green (schorl) prismatic or triangular in lateral cuts, and is full of fluid inclusions (Fig. 55).

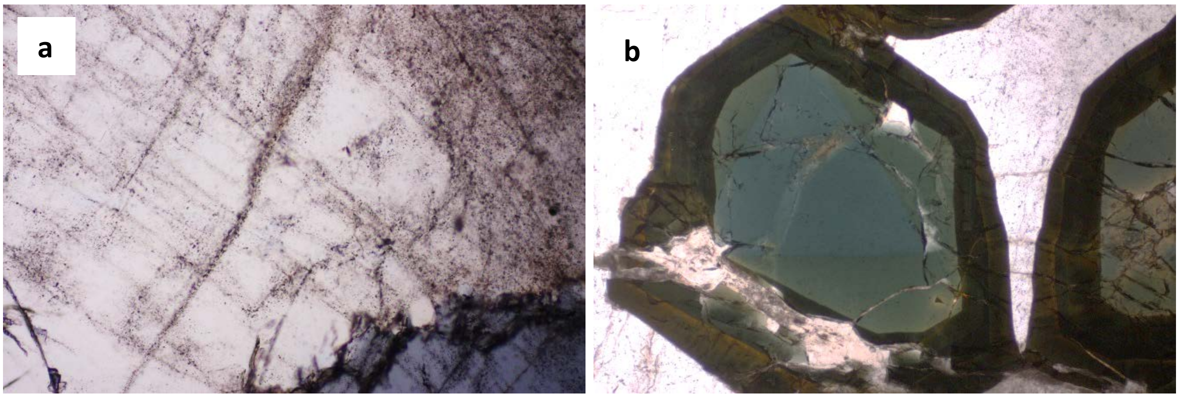

Fig. 55: Transmitted light image (a) of cracks and fluid inclusions enclosed in feldspar and quartz (length of the image 1 mm) and transmitted light image (b) of zoned tourmaline (length of the image 2 mm)

6.2.10. Sample 0 A

0A was collected along the road to San Illario within serpentinite.

The thin section displays a zoned dyke with coarse-grained tourmaline (up to 6 mm in size), quartz, feldspar and zones of fine-grained quartz, feldspar and tourmaline (Fig. 56). Coarse mica is accessory.

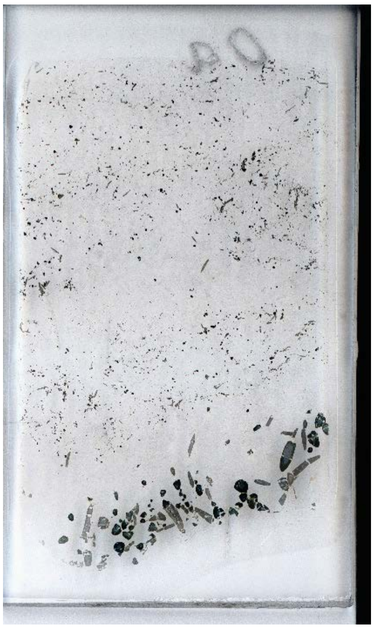

Fig. 56: Scanned thin section 0A with zoning (dimensions: 2.8 x 4.8 cm)

The quartz crystals with their different sizes are recrystallized, polycrystalline and sometimes showing embayments, or they occur as rounded, inclusion-free quartz nodules in deformed plagioclase (Fig. 57). Feldspars occur as plagioclase or K-feldspars and are generally sub-idiomorphic. They show albite and microcline twinning and sometimes exhibit perthitic alteration due to magmatic exsolution (Fig. 57).

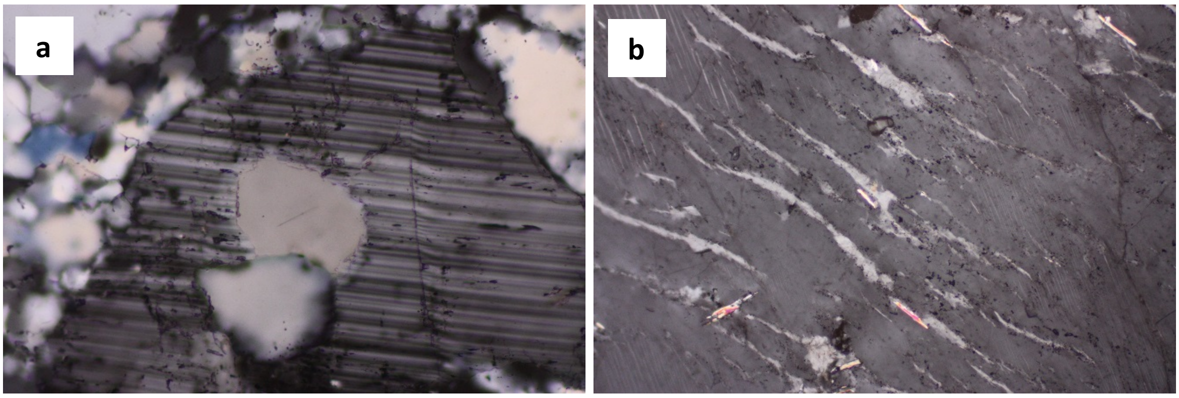

Fig. 57: Cross-polarized image (a) of recrystallized and rounded quartz in feldspar (length of the image 0.5 mm) and cross-polarized image (b) of perthitic exsolution of feldspar (length of the image 1 mm)

The large tourmaline crystals show zoning and often healed fractures due to cracks that were generated at the same time as tourmaline (Fig. 58). Generally, tourmaline has olive-green (schorl) prismatic crystals with distinctive pleochroism from bright brown to dark green at the rim or to blue in the core. In lateral cuts, the triangle crystals do not change the colours. The fine-grained tourmaline crystals display a different zoning (Fig. 58).

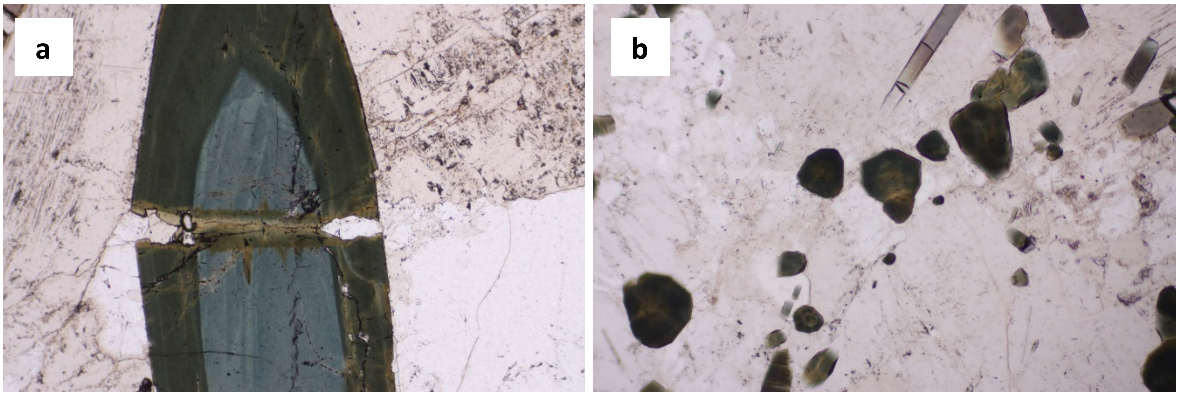

Fig. 58: Transmitted light image (a) of tourmaline with healed fractures (length of the image 2 mm) and transmitted light image (b) of fine-grained tourmaline crystals (length of the image 1 mm)

Fluid inclusions and primary melting inclusions can be found in tourmaline. The primary inclusions are often located at rims and the fluid inclusions are located along cracks and fractures (Fig. 59). Quartz crystals display fluid inclusions of several generations along traces, healed cracks and even along subgrain boundaries (Fig. 59).

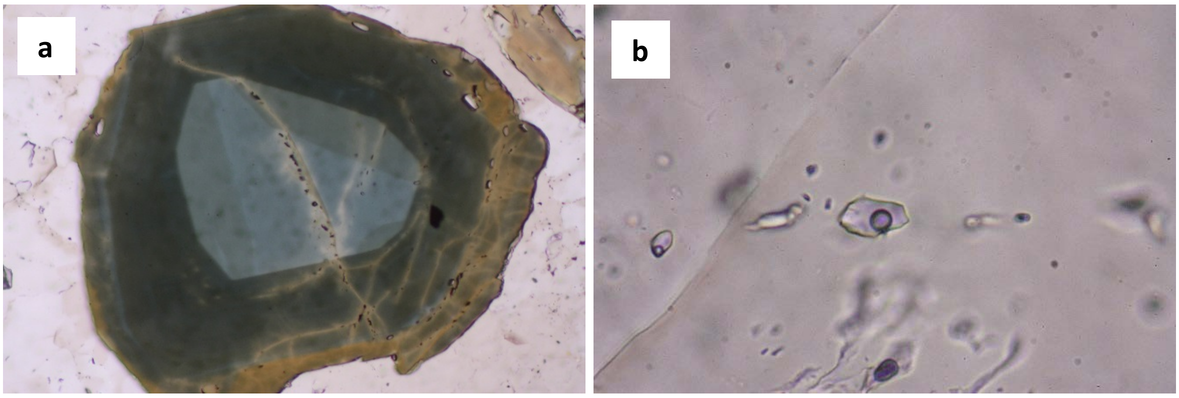

Fig. 59: Transmitted light image (a) of tourmaline with fluid inclusions along cracks and melting inclusions at the rim (length of the image 0.5 mm) and transmitted light image (b) of different fluid inclusions enclosed in quartz (length of the image 0.1 mm)

Raman spectroscopy allowed the classification of xenotime-(Y), YPO_4, grown together with zircon on tourmaline (Fig. 60) and of monazite-(Ce) as transparent single crystals with a high relief, also on tourmaline (Fig. 61) (Fig. A5 in the appendices).

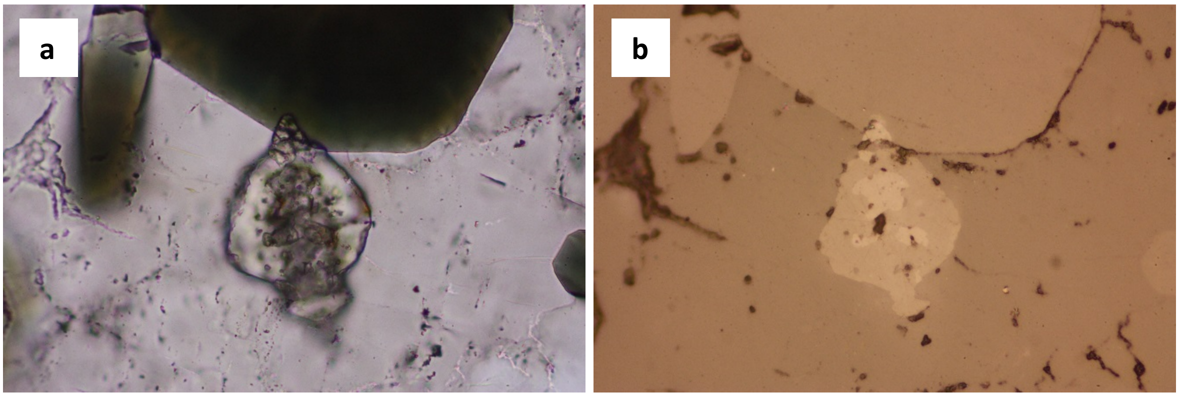

Fig. 60: Transmitted light image (a) and reflected light image (b) of xenotime and zircon on tourmaline (length of the images 0.2 mm)

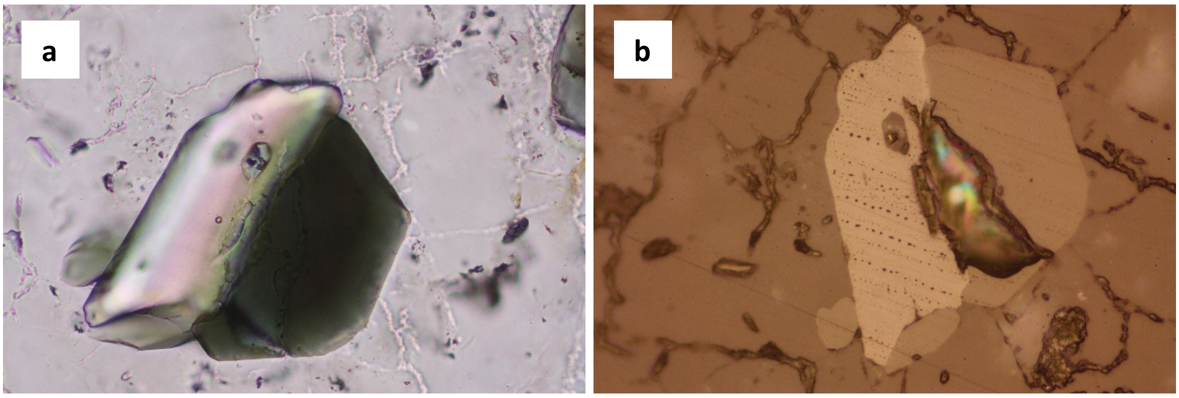

Fig. 61: Transmitted light image (a) and reflected light image (b) of monazite on tourmaline (length of the images 0.2 mm)

6.2.11. Sample 1 J

Sample 1J was collected at Spiaggia Spartaia, near Procchio. The country rock is a skarn with abundant calc silicate. Marble and metamorphic lime can be found in this rock with vesuvianite, wollastonite, calcite, feldspar, grossular and diopside.

1J consists of medium-grained quartz and feldspar as main components. Calcite, mica (especially biotite), hedenbergite and a few large opaque minerals are accessory. Quartz crystals are often recrystallized and polycrystalline, showing embayments, and make up 40% of the whole thin section. In addition, quartz displays zoning with primary inclusions in the rim and different generations of fluid inclusions along traces and as clouds in the core (Fig. 62). The fluid inclusions in quartz are negatively shaped and CH_4-rich with a little CO_2 content. Feldspar (especially plagioclase) is represented by subhedral, altered crystals, often with polysynthetic twinning.

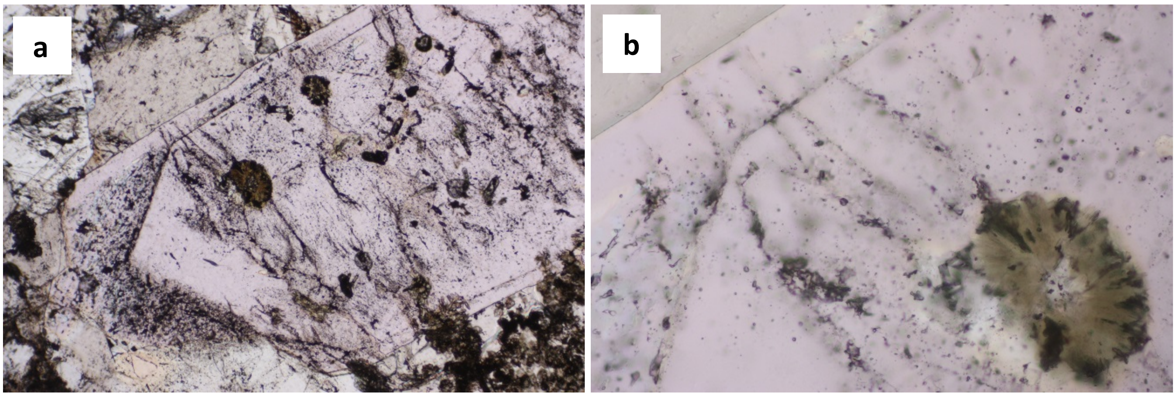

Fig. 62: Transmitted light image (a) of zoned quartz with different inclusions in the rim and in the core (length of the image 2 mm) and close-up (b) (length of the image 0.5 mm)

Fibrous chromite, elongated hedenbergite (Fig. A6 in the appendices) and rounded diopside inclusions as secondary minerals, often enclosed in the cores of quartz and feldspar, are common (Fig. 63). Therefore, an assimilation with the country rock occurred and calc silicates infiltrated this sample.

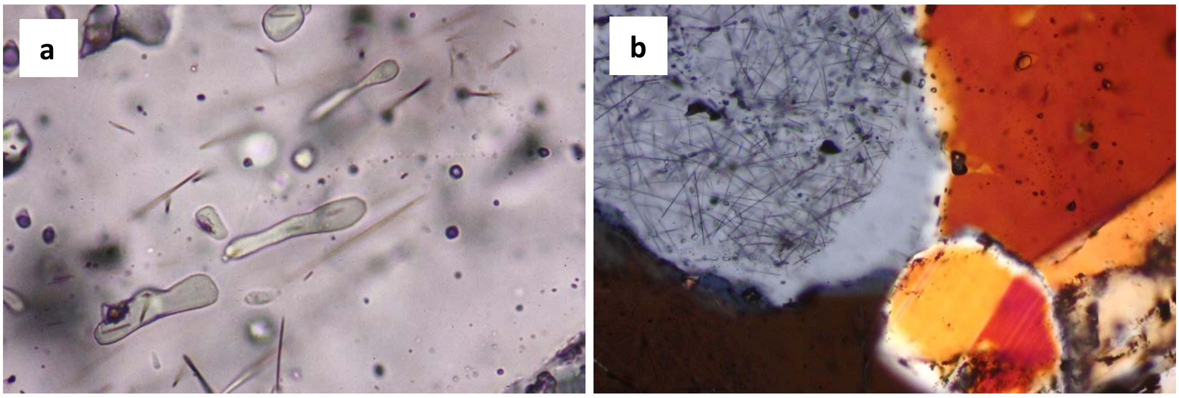

Fig. 63: Transmitted light image (a) of fibrous chromite and elongated hedenbergite enclosed in quartz (length of the image 0.1 mm) and cross-polarized image (b) of chromite and hedenbergite only enclosed in the core of a quartz (length of the image 0.5 mm)

Raman spectroscopy allowed the classification of zircon, pyrite, hematite, anatase and uraninite (Fig. 64). Titanite, a calcium titanium nesosilicate mineral, which is often eroded, evidences also the calcium-rich influence. The classification of smithite, $AgAsS_2$, an elongated sulfosalt, was also allowed (Fig. 64) (Fig. A7 in the appendices).

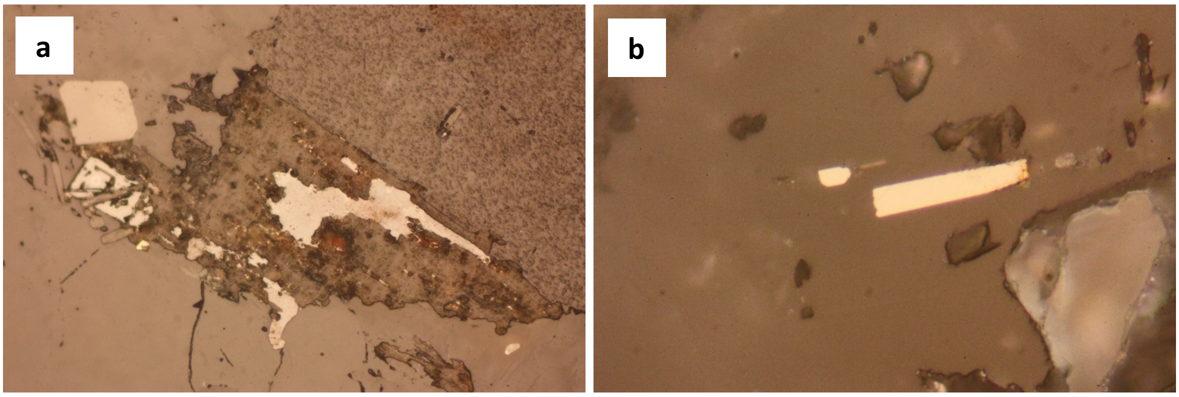

Fig. 64: Reflected light image (a) of cubic zircon, uraninite and intergrowth of pyrite and hematite in biotite (length of the image 0.5 mm) and reflected light image (b) of elongated smithite (length of the image 0.1 mm)

6.2.12. Sample 3 A

This sample was also collected at Spiaggia Spartaia, near Procchio. The thin section represents a weathered dyke with zoning. Large crystals with sizes up to 8 mm of tourmaline, quartz and feldspar are on the top of the thin section. Fine-grained (0.1 – 0.5 mm in size) crystals with a preferred orientation of quartz, feldspar and tourmaline are on the bottom(Fig. 65). A few opaque minerals are accessory.

Fig. 65: Scanned thin section 3A with zoning (dimensions: 4.8 x 2.8 cm)

Quartz is represented by polycrystalline, multiple-fractured crystals. On the bottom of the thin section, several quartz lenses can be found. Feldspar crystals are generally sub-idiomorphic whereas quartz is anhedric. The plagioclase crystals are generally subhedral to rounded and show albite-carlsbad and albite twinning. There are two generations of tourmalines because of the strong deformation. The first generation of tourmaline crystals are greenish brown, sometimes zoned and anhedral, and the second generation of crystals are blue, deformed and often fill cracks of the boudinated first generation tourmaline (Fig. 66).

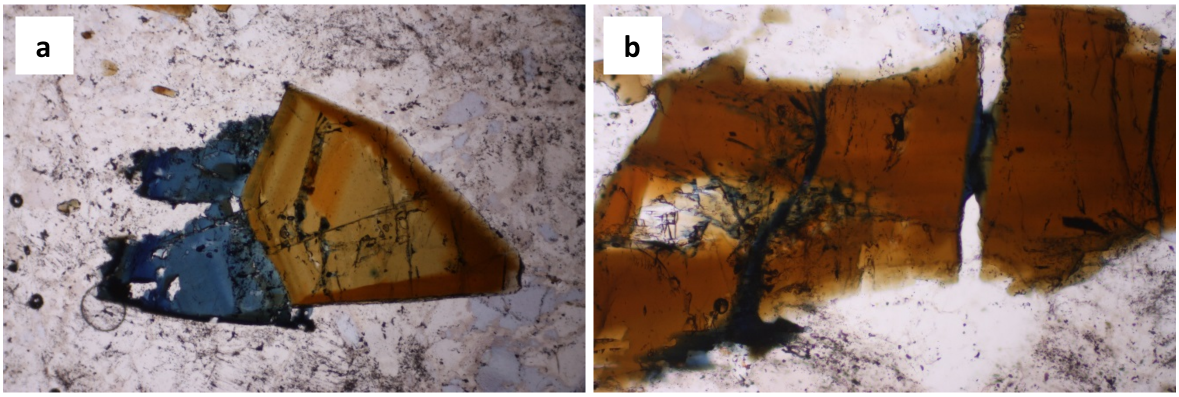

Fig. 66: Transmitted light image (a) of brown and deformed blue tourmaline (length of the image 2 mm) and transmitted light image (b) of boudinated tourmaline with blue tourmaline in cracks (length of the image 1 mm)

Raman spectroscopy evidenced the presence of pyrite, hematite and intergrowth of columbite-(Fe), $FeNb_2O_6$ and columbite-(Mn), $MnNb_2O_6$ (Fig. 67) (Fig. A8 + A9 in the appendices). Fluid inclusions enclosed in quartz or along subgrain boundaries are common. There are different types of fluid inclusions in quartz: one type is rich in gas-phases and consists of CO_2 and little amounts of CH_4, H_2S and N_2, wheras the other type contains columnar spinel crystals (Fig. 67).

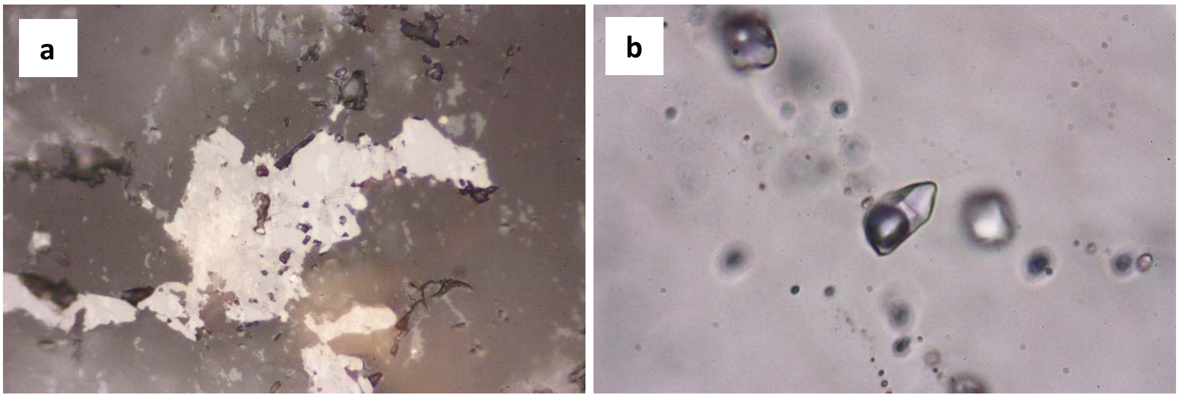

Fig. 67: Reflected light image (a) of intergrowth of columbite-(Fe) and columbite-(Mn) (length of the image 0.2 mm) and transmitted light image (b) of fluid inclusions with spinel crystals enclosed in quartz (length of the image 0.1 mm)

6.2.13. Sample 5 B

5B was collected at Spiaggia Pauline (Paolina) within radiolarite. The thin section displays a zoning of fine-grained quartz, feldspar on the bottom, coarse-grained quartz, tourmaline, feldspar in the middle and a mixed-grained zone (small tourmaline crystals with large quartz and feldspar) on the top of the thin section (Fig. 68).

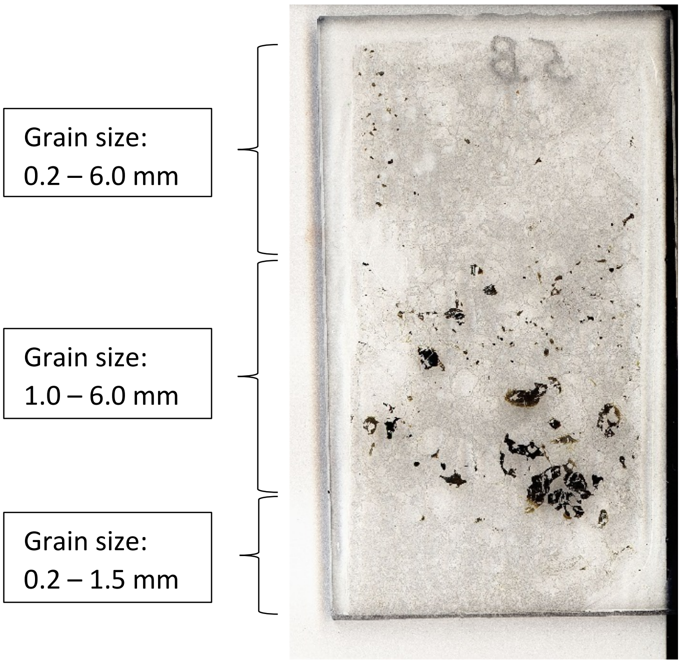

Fig. 68: Scanned thin section 5B with zoning (dimensions: 4.8 x 2.8 cm)

Primary mica occurs as coarse muscovite, secondary mica is often chloritized, radiated and grown together with hematite (Fig. 69). Opaque minerals are accessory. Quartz crystals occur as almost rounded and polycrystalline. Different types of fluid inclusions with CH_4, small amounts of CO_2 and a high salinity can be found enclosed in quartz (Fig. 69).

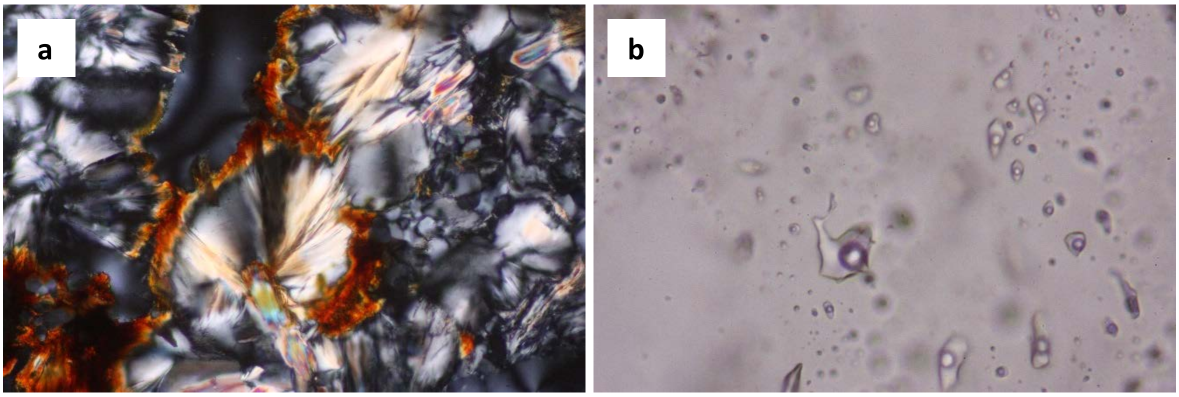

Fig. 69: Cross-polarized image (a) of chloritized radiating mica grown together with hematite (length of the image 0.5 mm) and transmitted light image (b) of different fluid inclusions enclosed in quartz (length of the image 0.1 mm)

Feldspars are generally subhedral and show albite-carlsbad or polysynthetic twinning. Occasionally, the feldspar crystals display exsolution lamination (Fig. 70). The large tourmaline crystals, up to 6 mm in size, are brown to greenish and generally zoned. They are sometimes irregular shaped, fractured and show a colourless rim, which indicates some interaction and replacement of the crystals (Fig. 71). Raman spectrosopy allowed the classification of cassiterite.

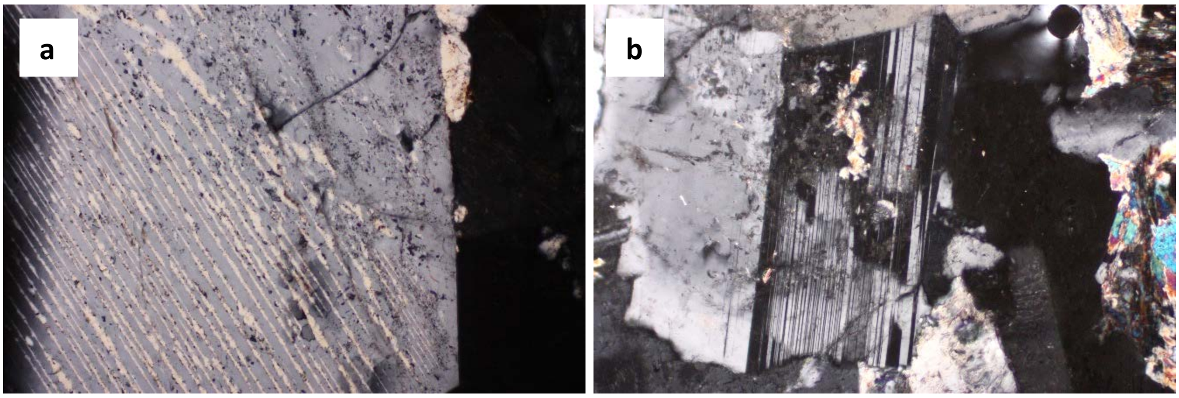

Fig. 70: Cross-polarized light image (a) of exsolution lamination of feldspar, compared to cross-polarized light image (b) of twinning (length of the images 1 mm)

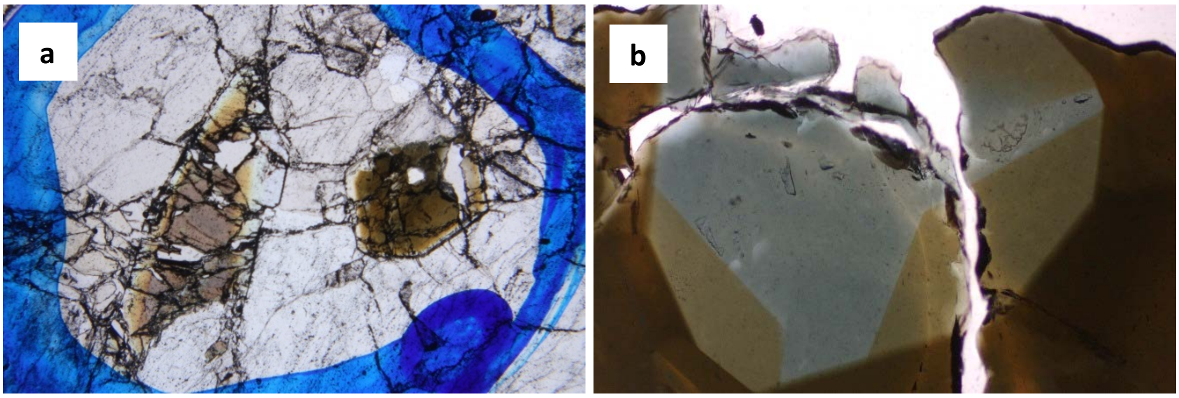

Fig. 71: Transmitted light image (a) of tourmaline crystals with a colourless rim (length of the image 4 mm) and transmitted light image (b) of zoned tourmaline (length of the image 1 mm)

6.2.14. Sample 9 C

This sample was collected at the west coast of Elba Island, south of Pomonte, within metasediment. The metasediment has a distinctive schistosity and consists of a fine-grained quartz and mica rich matrix (up to 0.05 mm in size) with opaque minerals and hematite.

The thin section contains a pegmatitic vein (thickness 2 cm) of medium-grained quartz, feldspar, tourmaline and mica (Fig. 72). In addition, several schistosity parallel veins (thicknesses from 0.5 to 4 mm), containing just quartz, are going through the brownish metasediment (Fig. 73).

Fig. 72: Scanned thin section 9C (dimensions: 4.8 x 2.8 cm)

Quartz as mineral phase makes up nearly 70% and is represented by recrystallized, polycrystalline, multiple-fractured crystals sometimes showing embayments.

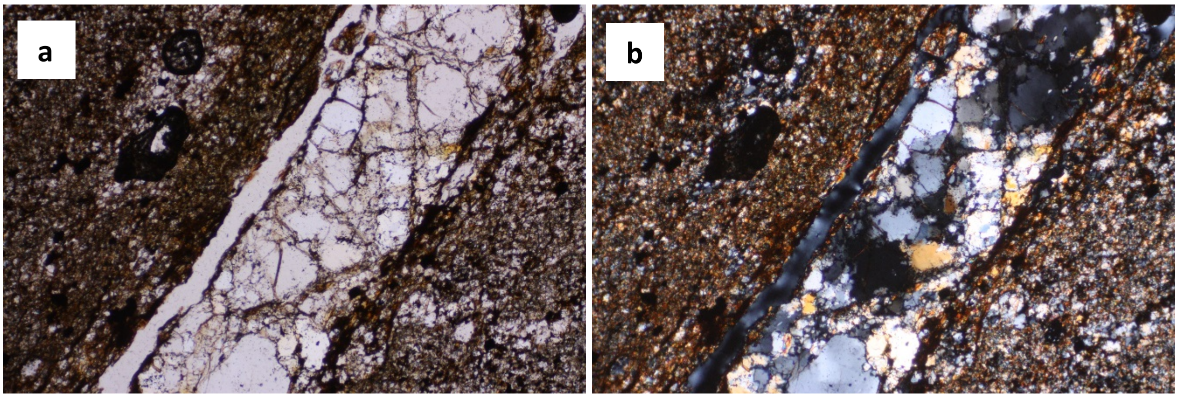

Fig. 73: Transmitted light image (a) and cross-polarized light image (b) of a schistosity parallel quartz vein through metasediment (length of the images 2 mm)

Feldspar crystals (especially plagioclase) occasionally show albite-carlsbad twinning, are anhedral and are sometimes included in quartz.

Bluish-brown and reddish-brown tourmaline is represented by large or irregular shaped crystals, up to 5 mm in size. Lateral cuts show typical triangles, which are often zoned (Fig. 74). Colourless mica as foliated crystals or as secondary sericite between grain boundaries occurs in the thin section (Fig. 74).

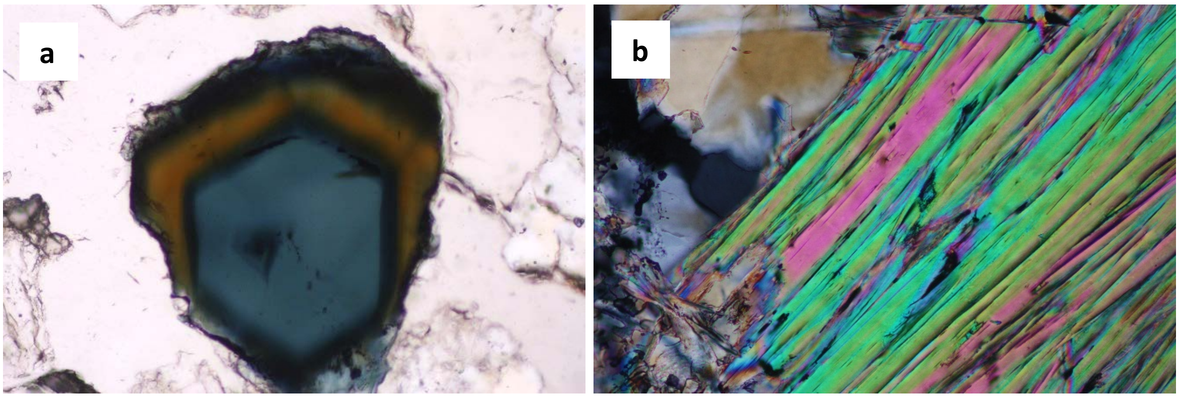

Fig. 74: Transmitted light image (a) of zoned tourmaline and cross-polarized light image (b) of foliated mica (length of the images 0.5 mm)

Raman spectroscopy allowed the classification of dark rutiles in the pegmatitic vein and of hematite in the metasediment, sometimes transformed into magnetite (Fig. 75). Only at the margin of the metasediment, a thin area with small tourmalines can be found within the metasediment due to assimilation by tourmaline (tourmalinization).

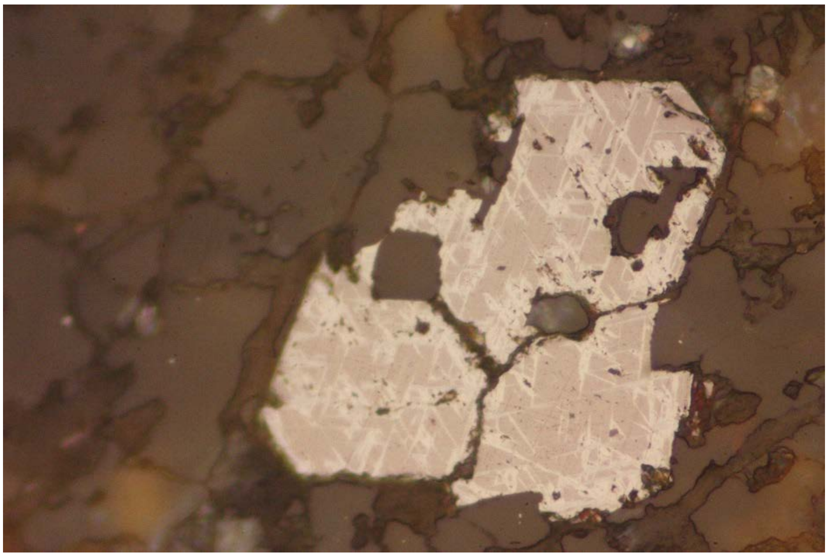

Fig. 75: Reflected light image of magnetite lamination in hematite (length of the image 0.2 mm)

6.2.15. Sample 15 A

15A was collected near the coast north of Chiessi within serpentinite. The thin section displays an undeformed grey volcanic dyke with a microcrystalline porphyritic texture (Fig. 76). The microcrystalline framework consists of quartz, plagioclase and biotite. Opaque minerals are accessory.

Fig. 76: Scanned thin section 15A (dimensions: 4.8 x 2.8 cm)

In this microcrystalline framework, large phenocrysts of quartz, plagioclase, allanite and biotite, up to 8 mm in size, are scattered. Quartz grains are rounded and undeformed, sometimes showing embayments (Fig. 77). Feldspars are generally subhedral or superposed and show albite-carlsbad and polysynthetic twinning (Fig. 77). The rims of the feldspars are sometimes affected by magmatic corrosion. In addition, feldspars often display alteration into sericite or calcite. The rounding and the internal corrosion of several grains occurred by dissolutions in the magma.

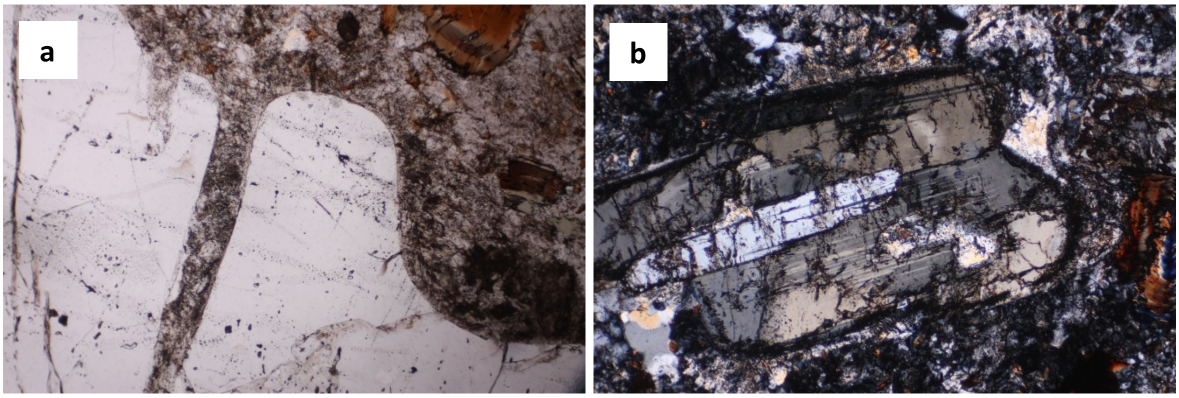

Fig. 77: Cross-polarized light image (a) of quartz embayments and cross-polarized light image (b) of superposed feldspar crystals with twinning and affected rims (length of the images 2 mm)

Biotite sometimes has prismatic, brown to reddish brown crystals with distinctive pleochroism from bright brown to dark brown, except locally greenish chloritized parts and pleochroic halos due to monazite-(Ce) and zircon crystals (Fig. 78). Apatite with colourless, short prismatic crystals and a high relief is also found enclosed in biotite. Allanite is another phenocryst with a pleochroism from pale red to pink (Fig. 78). Apatite, zircon, quartz and albite crystals are enclosed in allanite.

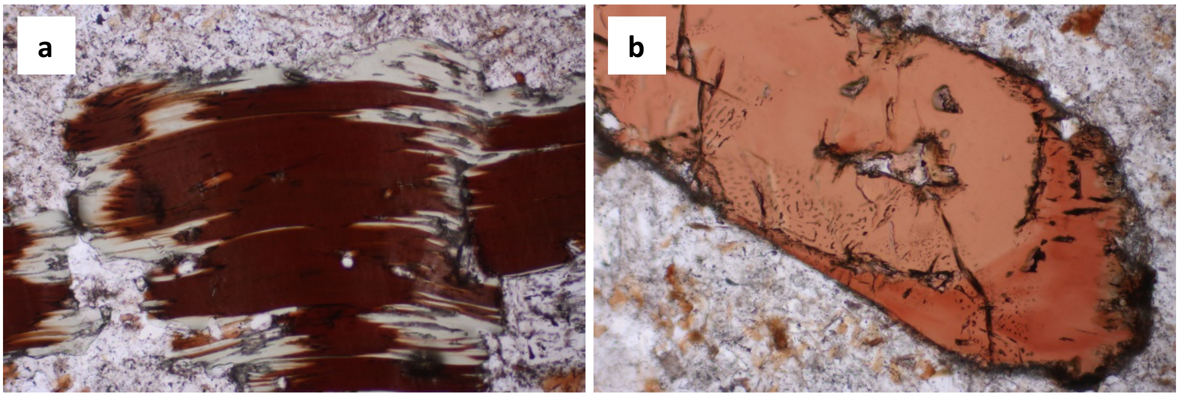

Fig. 78: Transmitted light image (a) of deformed and chloritized biotite and transmitted light image (b) of allanite with several inclusions (length of the images 1 mm)

There are different types of fluid inclusions (regular or rich in gas-phases) in the quartz phenocrysts. Both types contain CH_4 and CO_2. Large fluid inclusions are also enclosed in allanite (Fig. 79). Even feldspars exhibit inclusions: irregular fluid inclusions with cubic crystals and CH_4 in the vapour bubbles (Fig. 79). Raman spectroscopy evidenced the presence of zircon, brookite (TiO_2) and a niobium, tantalum oxide (Fig. A10 in the appendices).

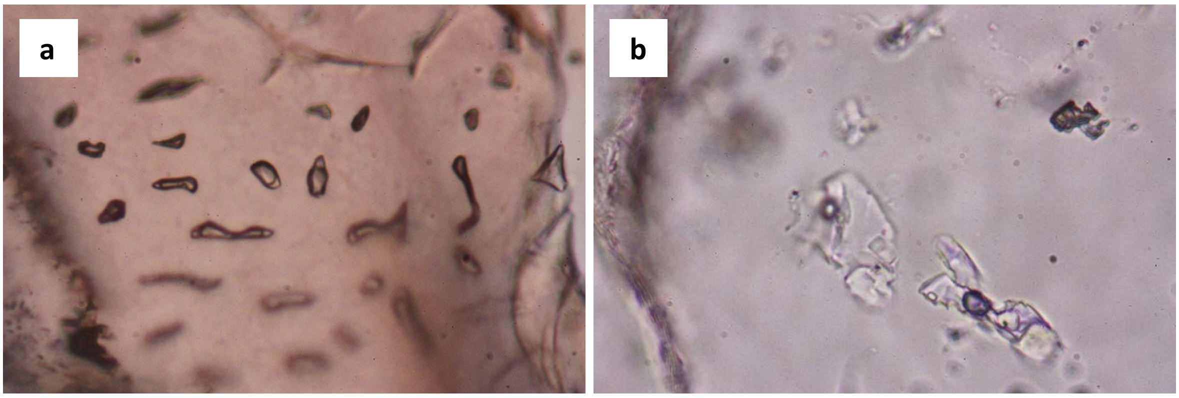

Fig. 79: Transmitted light image (a) of fluid inclusions enclosed in allanite and transmitted light image (b) of irregular fluid inclusions enclosed in feldspar (length of the images 0.1 mm)

6.2.16. Sample 17 A

Sample 17A was collected at Spiaggia Barbarossa near Porto Azzurro within calamita schist and was found near a fault-zone, which affected the bedrock. The thin section represents a brecciated pegmatite with several exsolutions along small veins and brittle deformation (Fig. 80).

Fig. 80: Scanned thin section 17A (dimensions: 4.8 x 2.8 cm)

Quartz crystals are represented as recrystallized, polycrystalline and coarse-grained on the bottom of the thin section. Sometimes they are showing embayments and subdomains. Some feldspars are large (up to 8 mm in size) and altered, showing rare polysynthetic twinning and exsolution lamination (flame-like lamellae). Quartz often shows magmatic exsolution within feldspars (Fig. 81).

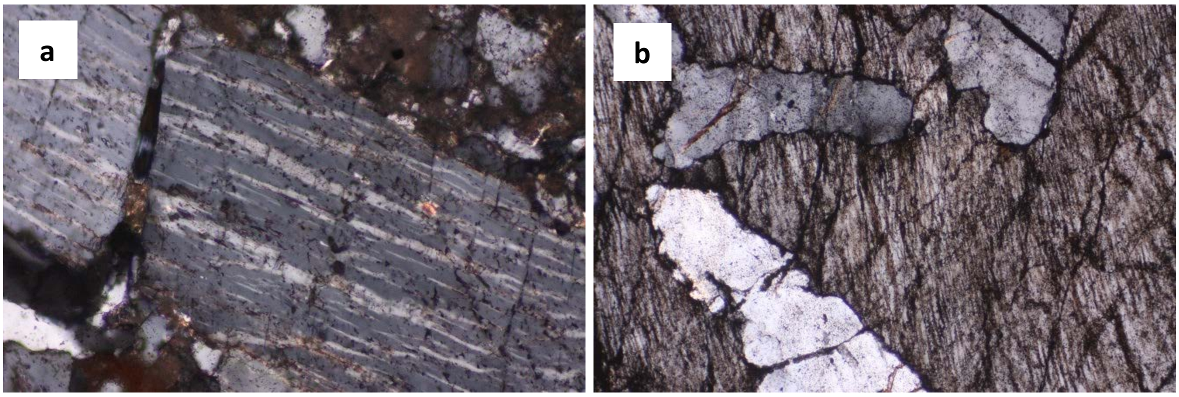

Fig. 81: Cross-polarized image (a) of flame-like lamellae in feldspar (length of the image 0.5 mm) and cross-polarized image (b) of exsolutions of quartz within feldspar (length of the image 2 mm)

Tourmaline as a minor component with a few fragments along exsolution veins appears small. The breccia consists of fragments, chlorite and hematite, which fill fractures and fissures and sometimes replace primary minerals. Even fluid inclusions enclosed in feldspar, quartz and tourmaline can be found in this brecciated rock (Fig. 82).

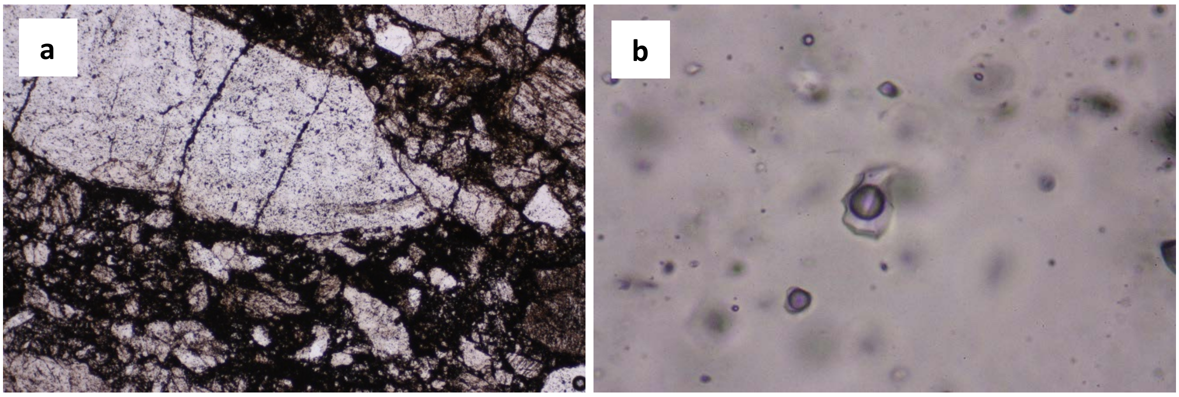

Fig. 82: Transmitted light image (a) of the breccia with fragments (length of the image 2 mm) and transmitted light image (b) of fluid inclusions enclosed in quartz (length of the image 0.1 mm)

6.2.17. Sample 23 F

This sample was collected at the beach of Ferrato on the Calamita peninsula within calamita schist. The thin section displays a weathered rock with a microcrystalline porphyritic texture (Fig. 83).

Fig. 83: Scanned thin section 23F (dimensions: 4.8 x 2.8 cm)

The microcrystalline texture consists of quartz, feldspar and mica. In this framework, large phenocrysts of quartz, feldspar and tourmaline, up to 6 mm in size, are scattered. Only on the top of the thin section, andalusite with a high relief and a distinctive pleochroism from colourless to pink can be found as a minor component. Some opaque inclusions (alloy) and quartz are enclosed in andalusite. Quartz often appears recrystallized, polycrystalline and as altered crystals, often with subgrains which are inclusion-free. Only rounded quartz relicts within feldspars are protected against recrystallization. Feldspars are generally subhedral and often display polysynthetic twinning and deformation like fracturing and stretching (Fig. 84).

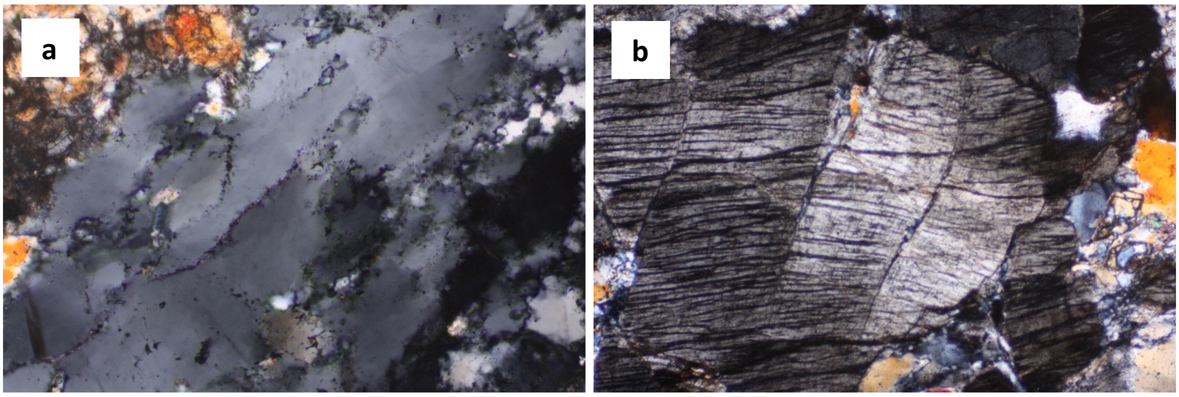

Fig. 84: Cross-polarized image (a) of recrystallized quartz with subgrains (length of the image 1 mm) and cross-polarized light image (b) of fractured and stretched feldspar (length of the image 2 mm)

The tourmaline crystals are prismatic, up to 6 mm in size, and sometimes fractured and show a great variation of colours and zoning, which indicate different element compositions (Fig. 85). Rutiles and spinels are enclosed in tourmaline. Mica fills fractures and fissures as a secondary mineral, especially in feldspars. Fluid inclusions with cubic salt crystals can only be found in quartz relicts within feldspars (Fig. 85). Sometimes they contain CH_4 and small amounts of CO_2.

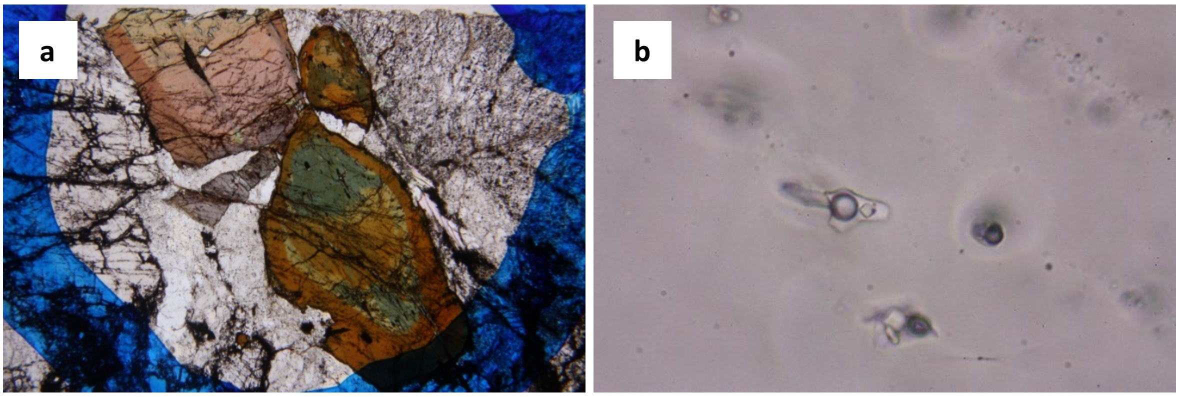

Fig. 85: Transmitted light image (a) of colourful tourmaline crystals with zoning (length of the image 4 mm) and transmitted light image (b) of fluid inclusions with cubic crystals enclosed in quartz relicts (length of the image 0.1 mm)

6.2.18. Sample 25 A

25A was collected at the beach of Istia on the Calamita peninsula within calamita schist. The thin section shows different brecciated zones of fine- to medium-grained tourmaline with a preferred orientation, quartz, feldspar and pink andalusite on the edges of the thin section as well as a zone of coarse-grained quartz, K-feldspar and secondary mica on the middle of the thin section (Fig. 86).

Fig. 86: Scanned thin section 25A with different zones (dimensions: 4.8 x 2.8 cm)

Quartz is represented by elongated and highly recrystallized crystals, sometimes showing embayments, or by intact relicts due to magmatic exsolution of quartz in feldspars (Fig. 87). Occasionally, mica fills pores and fissures as a secondary mineral. Feldspars are often deformed and altered and show rare polysynthetic twinning.

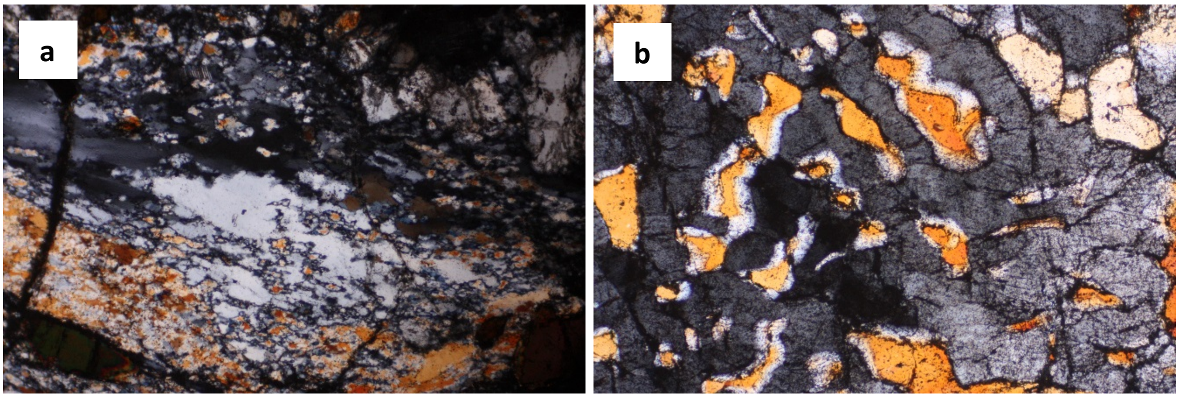

Fig. 87: Cross-polarized light image (a) of highly recrystallized quartz and cross-polarized light image (b) of magmatic exsolution of quartz in feldspar (length of the images 2 mm)

Brownish-green and reddish-yellow tourmaline crystals are either prismatic or small and triangular in lateral cuts and the long axes of these crystals have a preferred orientation. Occasionally, tourmaline is brittlely deformed and boudinated in a direction parallel to this preferred orientation and sometimes the crystals display cracks along traces perpendicular to the stretching lineation (Fig. 88). In addition, the tourmaline crystals in this thin section even show radiation damages with pleochroic halos, which occur as darkish green spots around intergrowths of xenotime-(Y) and zircon (Fig. 88).

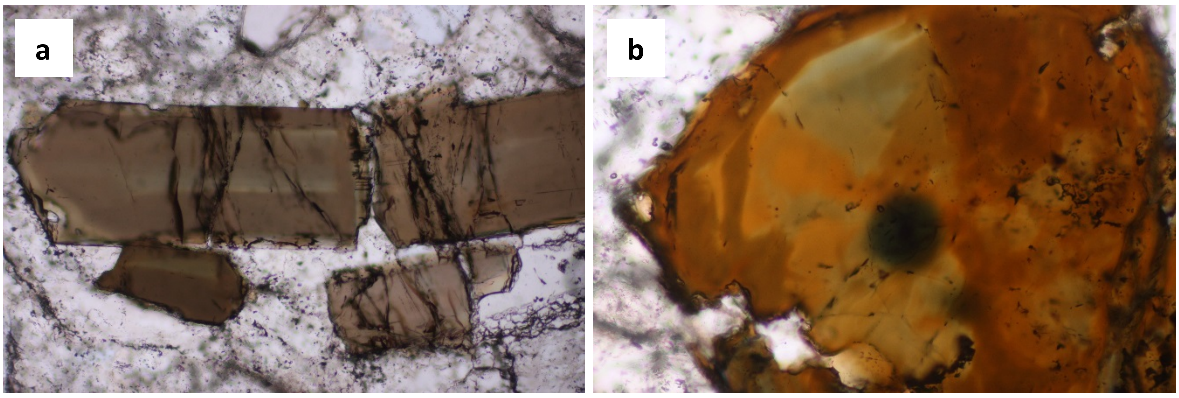

Fig. 88: Transmitted light image (a) of boudinated tourmaline with cracks (length of the image 1 mm) and transmitted light image (b) of radiation damage in tourmaline (length of the image 0.5 mm)

At the edge of the thin section, pink andalusite crystals with a distinctive zoning and middle high relief can be found (Fig. 86). Andalusite is also brittely deformed and boudinated, and melting inclusions, diaspore (Fig. 90) and fluid inclusions with CO_2 in the vapour bubbles, are often enclosed in andalusite. Regular fluid inclusions along traces with cubic salt crystals, micas or pyrosmalite-(Fe) (Fig. 91), irregular-shaped, and gas-rich inclusions can be observed in quartz (Fig. 89).

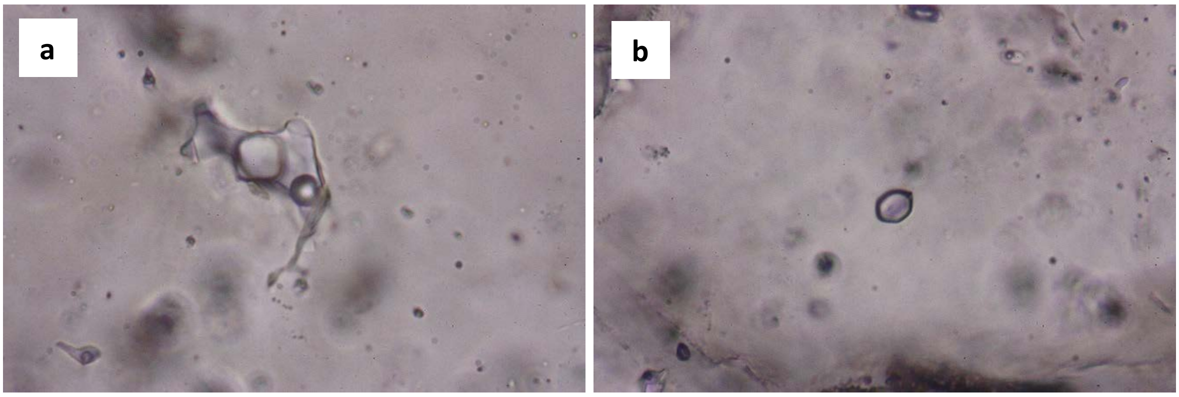

Fig. 89:Transmitted light image (a) of a fluid inclusion with a cubic salt crystal and transmitted light image (b) of a fluid inclusion rich in gas-phases enclosed in quartz (length of the images 0.1 mm)

Raman spectroscopy allowed the classification of columbite-(Fe) and intergrowths of rutile, anatase (Fig. A11 in the appendices) and brookite. Xenotime-(Y) and zircon crystals were causing the radiation damages of tourmaline.

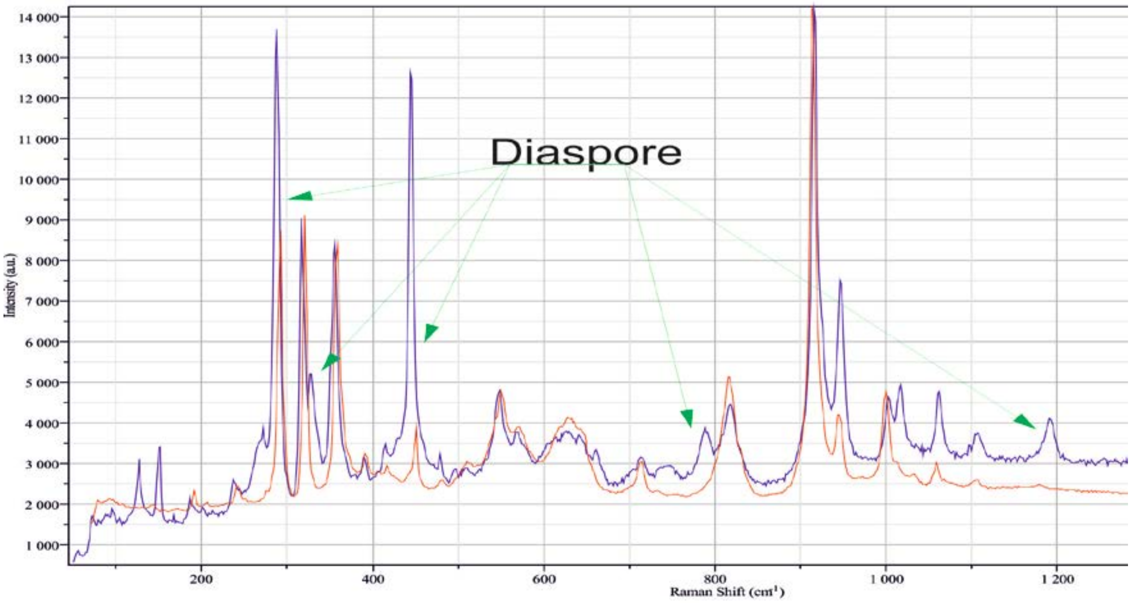

Fig. 90: Raman spectrum of andalusite (red) and combination of andalusite and diaspore (blue) (peaks at Raman shift 160, 340, 425, 790, 1190 cm^{-1})

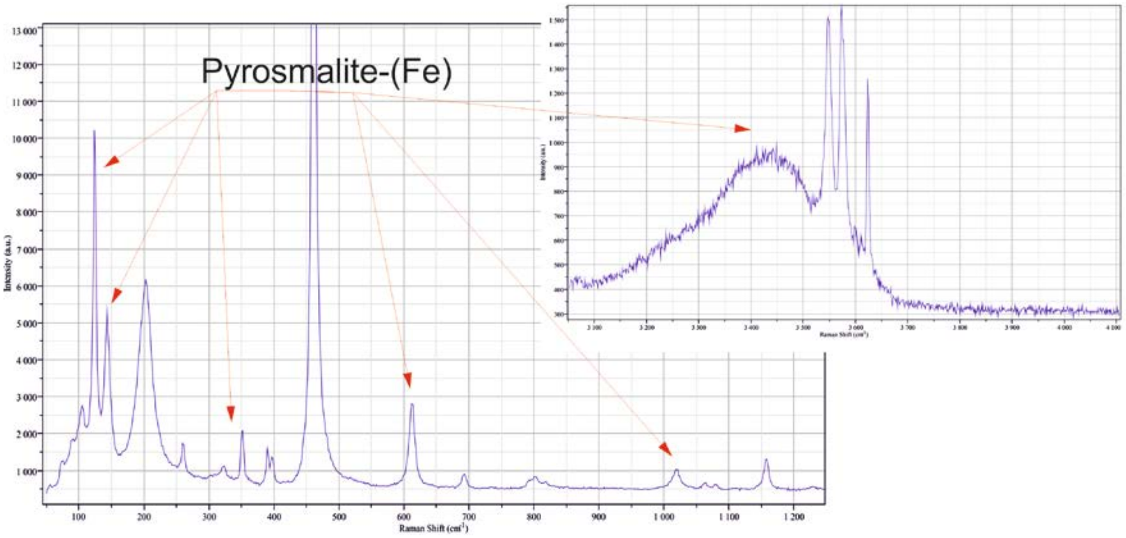

Fig. 91: Raman spectrum of quartz and pyrosmalite - (Fe) (blue) as well as the OH spectrum of pyrosmalite - (Fe) (green) (peaks at Raman shift 106, 143, 360, 620 (main peak), 1020 cm^{-1})

6.2.19. Sample 29 D

This sample was collected at the beach of Stagnano on the Calamita peninsula within calamita schist. The thin section displays two zones. One zone consists of fine- to medium-grained feldspar with titanite and little amounts of quartz and the other zone is a brownish, tourmaline- and feldspar-rich groundmass with quartz lenses and opaque minerals (Fig. 92).

Fig. 92: Scanned thin section 29D with brownish tourmaline, feldspar groundmass (dimensions: 4.8 x 2.8 cm)

Quartz is represented by polycrystalline, totally recrystallized crystals or by inclusion-rich relicts in the groundmass (Fig. 93). The groundmass consists of fine-grained tourmaline and albite with (1) aggregates of small (up to 0.5 mm in size) columnar and radiating tourmaline crystals and with (2) aggregates of dark rutiles and colourless titanites (Fig. A12 in the appendices). Large titanites (up to 0.5 mm in size) are common in the white feldspar matrix (Fig. 94).

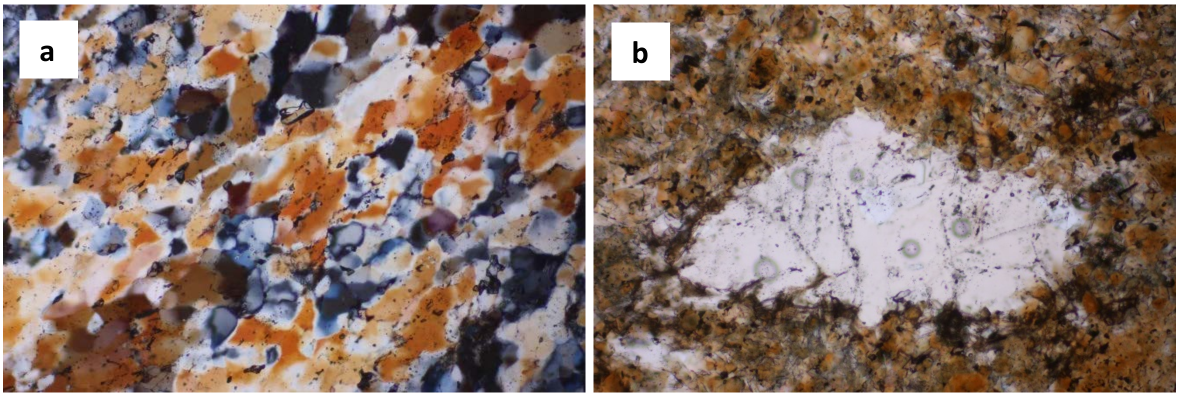

Fig. 93: Cross-polarized light image (a) of totally recrystallized quartz and transmitted light image (b) of a quartz lens in the brownish groundmass (length of the images 1 mm)

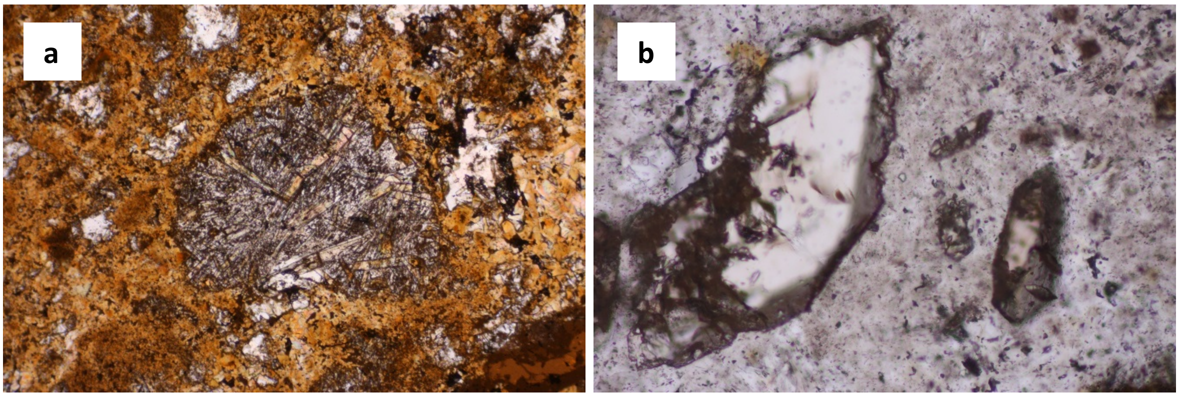

Fig. 94: Transmitted light image (a) of radiating, columnar tourmaline crystals within the albite-tourmaline groundmass (length of the image 2 mm) and transmitted light image (b) of titanite within the white feldspar matrix (length of the image 0.5 mm)

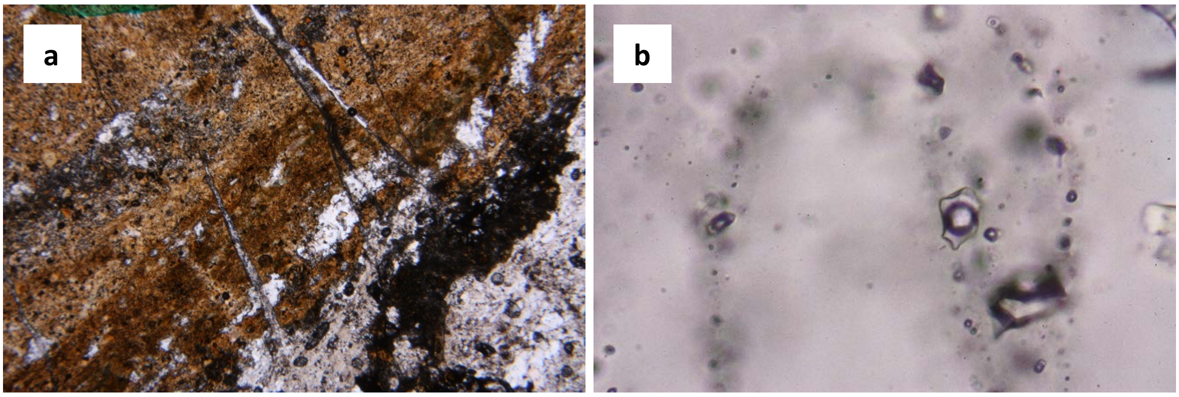

Fig. 95:Transmitted light image (a) of interaction between the brownish groundmass and the white matrix (length of the image 4 mm) and transmitted light image (b) of different types of fluid inclusion along traces enclosed in quartz (length of the image 0.1 mm)

Very small feldspar fissures and cracks from the white matrix interfuse the tourmaline-albite groundmass. In addition, the brownish groundmass interfuses the white matrix on the top of the thin section and displays a flow structure. Different types of fluid inclusions are enclosed in the quartz lenses, where some are rich in CO_2 and some are high in salinity (Fig. 95).

6.2.20. Sample 35 B

Sample 35B was collected near the mine "Ginepro" on the Calamita peninsula within calamita schist. The thin section shows fine- to medium-grained (sizes from 0.5 mm to 4 mm) quartz, feldspar, andalusite, garnet and tourmaline crystals (Fig. 96). Opaque minerals are accessory.

Fig. 96: Scanned thin section 35B (dimensions: 4.8 x 2.8 cm)

Quartz is represented by anhedral crystals, which are often multiple-fractured and recrystallized due to static deformation. Feldspars are generally sub-idiomorphic, altered and show albite twinning and exsolution alteration (Fig. 97). Large feldspar crystals (up to 4 mm in size) display a magmatic texture. Only minor sericitic replacement occurs, the majority of the feldspars are not affected (Fig. 97). The colourless andalusite crystals, up to 2 mm in size, with a middle high relief, are columnar or zoned with a pink colour in the core and the lateral cut shows squares (Fig. 98) (Fig. A13 in the appendices).

The large tourmaline crystals (up to 3.5 mm in size) are idiomorphic, sometimes fractured and display a great variation of colours and zoning (Fig. 98). In this thin section, some tourmalines also show radiation halos.

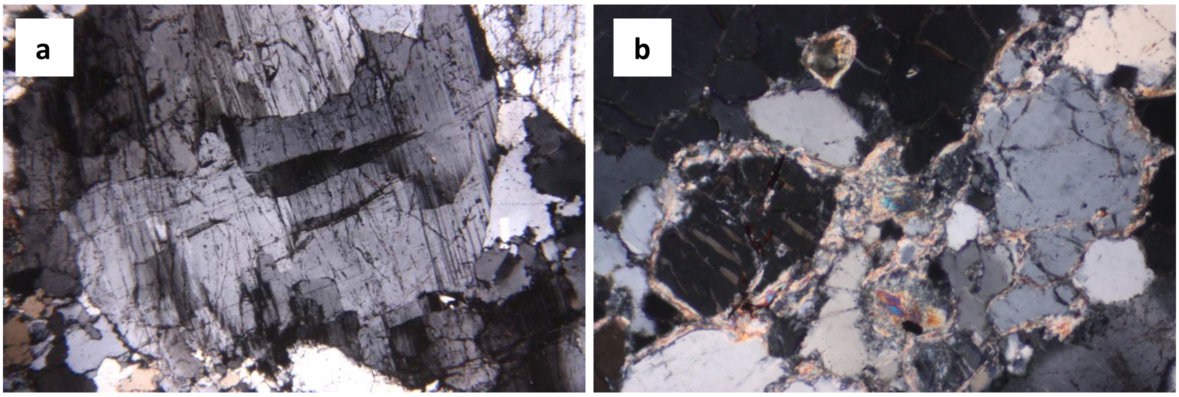

Fig. 97: Cross-polarized light image (a) of feldspar with twinning (length of the image 4 mm) and cross-polarized light image of sericitic replacement (length of the image 1 mm)

Garnet is represented as euhedral colourless to pale red crystals with a high relief and an isotropy. Raman spectroscopy allowed the classification of almandine.

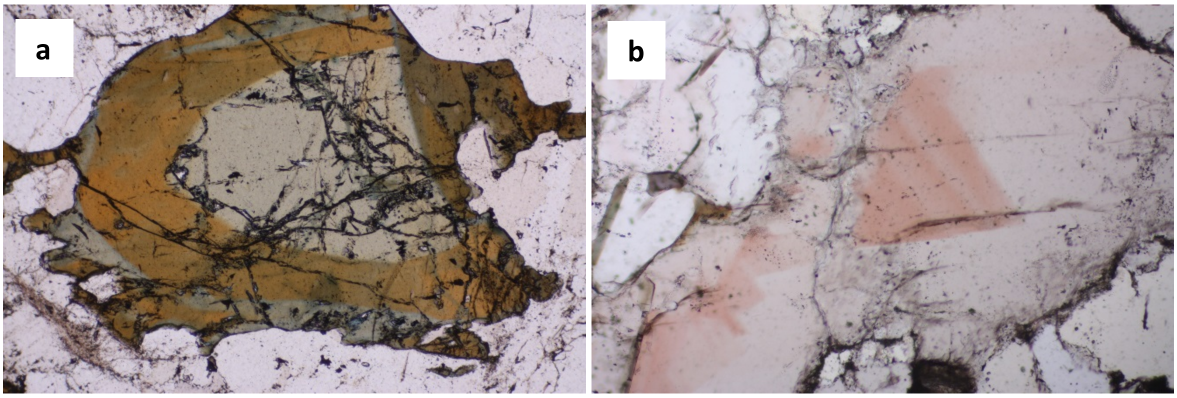

Fig. 98: Transmitted light image (a) of colourful, zoned tourmaline (length of the image 2 mm) and transmitted light image (b) of zoned, pink andalusite (length of the image 1 mm)

Fluid inclusions enclosed in andalusite are rich in gas-phases. They contain CO_2, CH_4 and sometimes mica and quartz. H_2O-rich, often secondary fluid inclusions can be found enclosed in tourmaline. In addition, different types of fluid inclusions are enclosed in quartz: (1) rich in gas-phases (CO_2 and little amount of CH_4), (2) inclusions with cubic salt crystals and (3) inclusions along traces, which contain crystals with birefringence (Fig. 99).

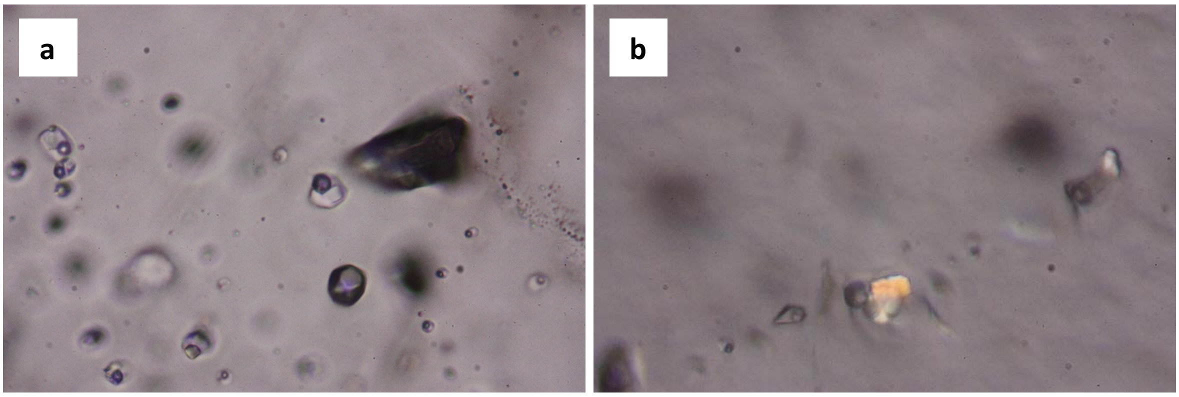

Fig. 99: Transmitted light image (a) of fluid inclusions rich in gas-phases (dark inclusions) and with cubic salt crystals and cross-polarized light image (b) of a fluid inclusion, which contain a crystal with birefringence enclosed in quartz (length of the images 0.1 mm)

Raman spectroscopy evidenced the presence of bright titanite crystals and of intergrowths of reddish-black columbite-(Fe) and columbite-(Mn) (Fig. 100).

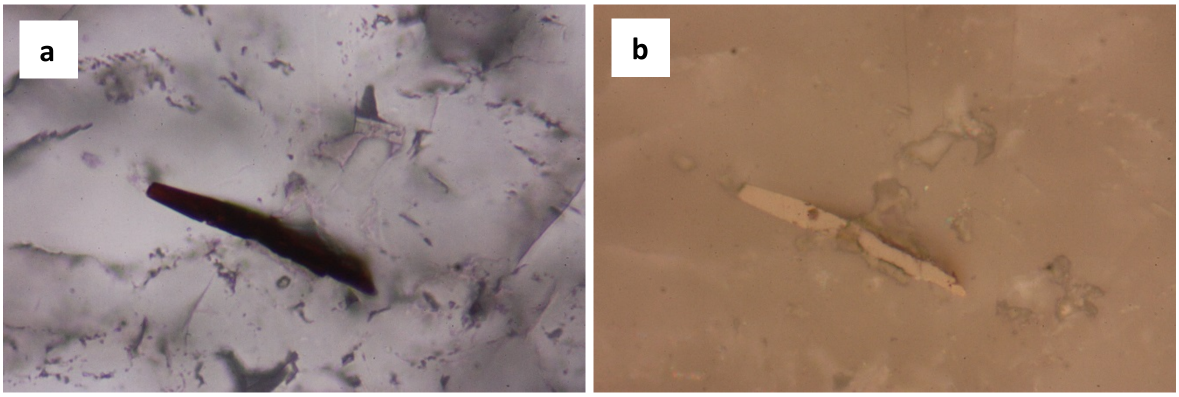

Fig. 100: Transmitted light image (a) and reflected light image (b) of columbite (length of the images 0.1 mm)

6.3. Fluid Inclusion Research

Nine thick sections were prepared for fluid inclusion research. Sample 67E and 85A were used to prepare small samples (between 4 and 10 mm in size) of single crystals for microthermometry. A single quartz grain (QTZ3) was cut from sample 67E. Two quartz grains (QTZ1 and QTZ2) and one piece with three tourmaline grains (TUR1) were cut from sample 85A. Both samples are from the eastern part of the Monte Capanne pluton. The nucleation, melting and homogenization temperatures of the fluid inclusions were analysed with microthermometry (see Chapter 6.1.2). The compositions of the fluid inclusions were measured with Raman spectroscopy (see Chapter 6.1.1) and a combination of Raman spectroscopy and microthermometry.

6.3.1. Sample 67E – QTZ3

In this both side polished sample (Fig. 101), four different types of altogether 69 studied fluid inclusions were classified (Tab. A3 + A4 in the appendecies). The liquid phase of these inclusions consists of a low concentration of brine (low salinity).

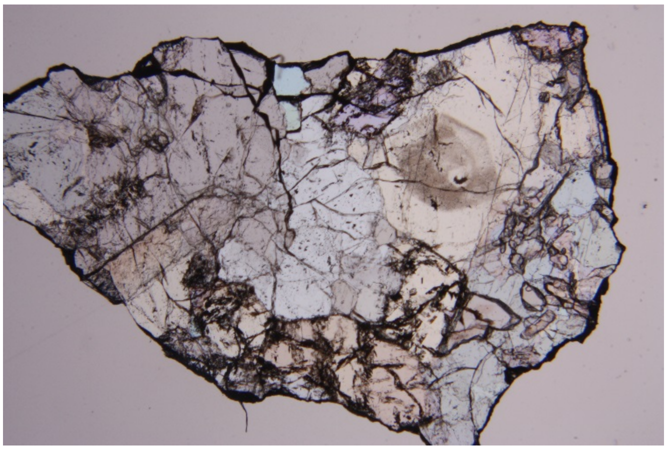

Fig. 101: Transmitted light image of sample 67E - QTZ3 (length of the image 4 mm)

Type I (Fig. 102) cannot be found along fissures or traces and is represented by isolated, randomly distributed fluid inclusions. This type is characterized by regular shaped large inclusions (7.5 – 20.5 µm in diameter) with a high area bubble ratio (area of the bubble divided by the total area, from

25 to 50 vol%). The vapour phase consists of highly variable amounts of CO_2 (x varies from 0.2 to 0.9) and CH_4 (x varies from 0.1 to 0.9) and minor amounts of N_2 (x varies from 0.00 to 0.04) and H_2 (x varies from 0.00 to 0.12) (Fig. 103). The borate mineral sassolite, H_3BO_3 was identified by Raman spectroscopy as dark tiny tabular crystals, only in the liquid phases of Type I (Fig. 105). The size of this crystal and its solubility can be influenced by the laser beam of the Raman spectroscopy.

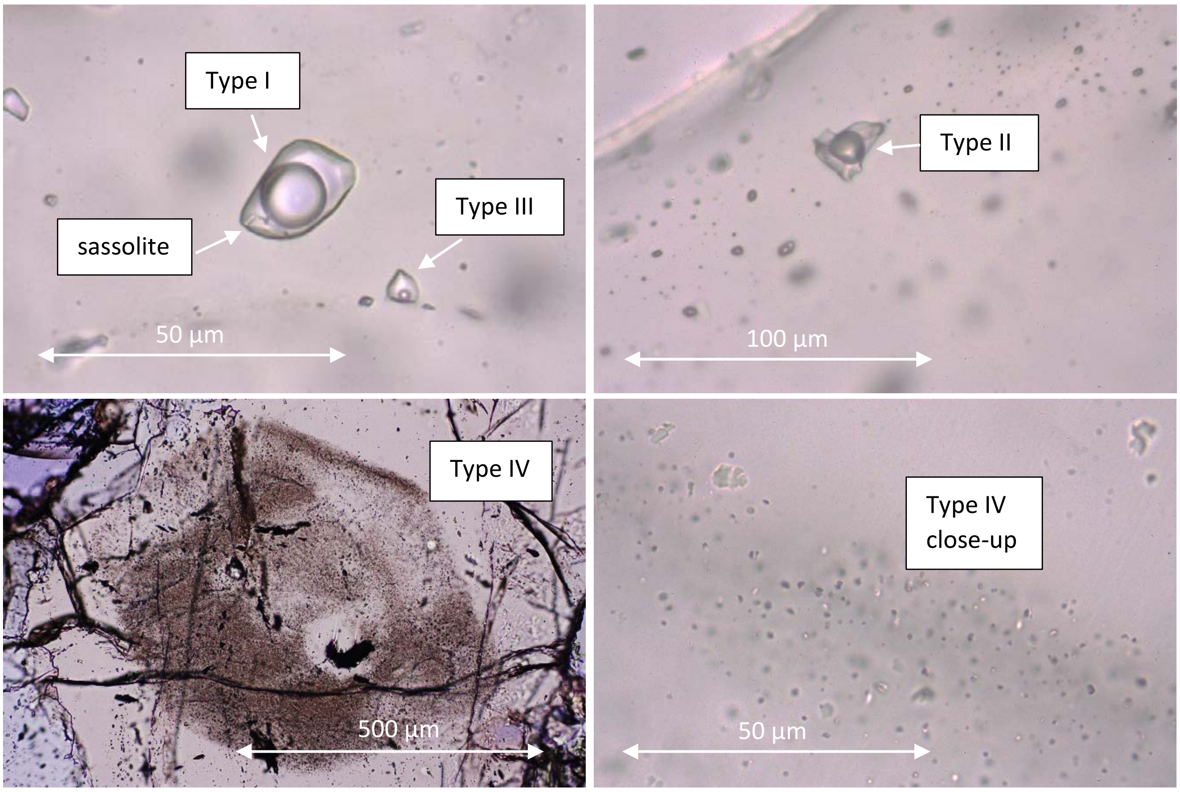

Fig. 102: Transmitted light images of the different fluid inclusion types in sample 67E - QTZ3

Type II (Fig. 102) does not occur along fissures or traces and is isolated and randomly distributed. This type is characterized by irregular shaped, greyish inclusions, 8–24 µm in diameter. The classification was done only because of this shape. Similar to Type I, area bubble ratios (from 10 to 60 vol%), and variable amounts of CO_2 (x varies from 0.0 to 0.5), H_2 (x varies from 0.1 to 1.0) and CH_4 (x varies from 0.0 to 0.4) were identified (Fig. 103).

Type III (Fig. 102) can be found along fissures or traces as a second generation. It is represented by small regular shaped inclusions (5–12 µm in diameter) with a low area bubble ratio (from 10 to 30 vol%). The vapour phases consist of variable amounts of CH_4 (x varies from 0.0 to 0.4) and H_2 (x varies from 0.6 to 1.0), whereas CO_2 was not detected in the vapour bubbles (Fig. 103).

Type IV (Fig. 102) represents tiny inclusions (~ 1 µm in diameter), which only occur in an assemblage as a cloud in the central part of quartz crystals. The vapour phases contain H_2, CO_2 and CH_4, but only small amounts were detected with Raman spectroscopy, which do not allow composition calculation. In the inclusions, tiny columnar crystals were identified as mica (birefringent grains in Fig. 102). This type represents the oldest generation of inclusions in the sample.

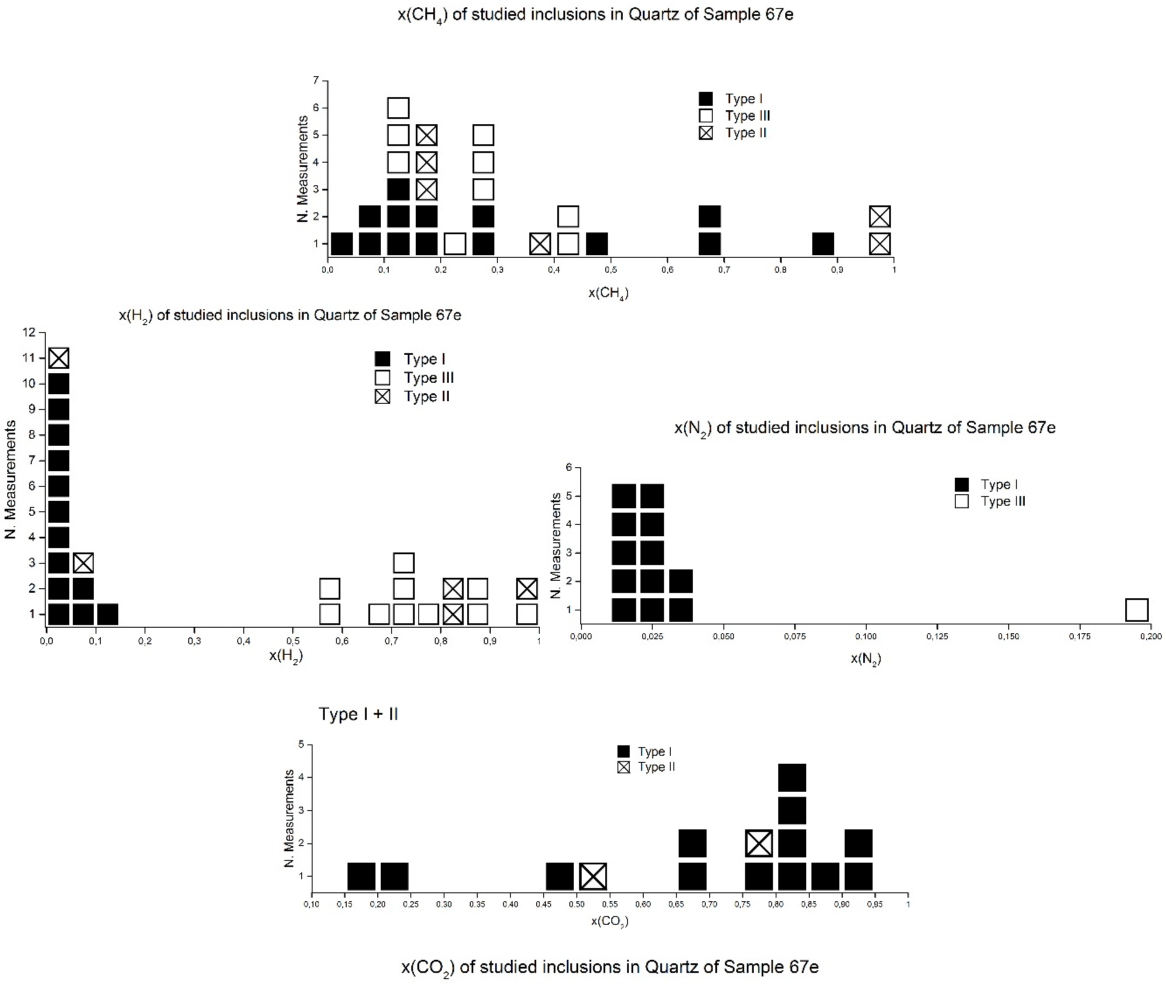

Fig. 103: The composition of the different types of fluid inclusions in sample 67E-QTZ3

Two nucleation temperatures of Type I were observed during cooling experiments at around -30°C and around -40°C. The first melting temperature varies from -7.7°C to +1.4°C and represents the ice melting; the second melting temperature varies from -0.8°C to +11.3°C and represents the clathrate melting. The homogenization temperature of Type I varies from 281.2°C to 381.3°C, the mode is between 360°C and 380°C, which display most occurring temperatures and the highest of all types (Fig. 104).

The melting temperature of Type II varies from -2.4°C to +4.1°C and the homogenization temperature is highly variable from 126.8°C to 389.5°C with a mode between 180°C and 240°C, which is clearly lower than Type I (Fig. 104).

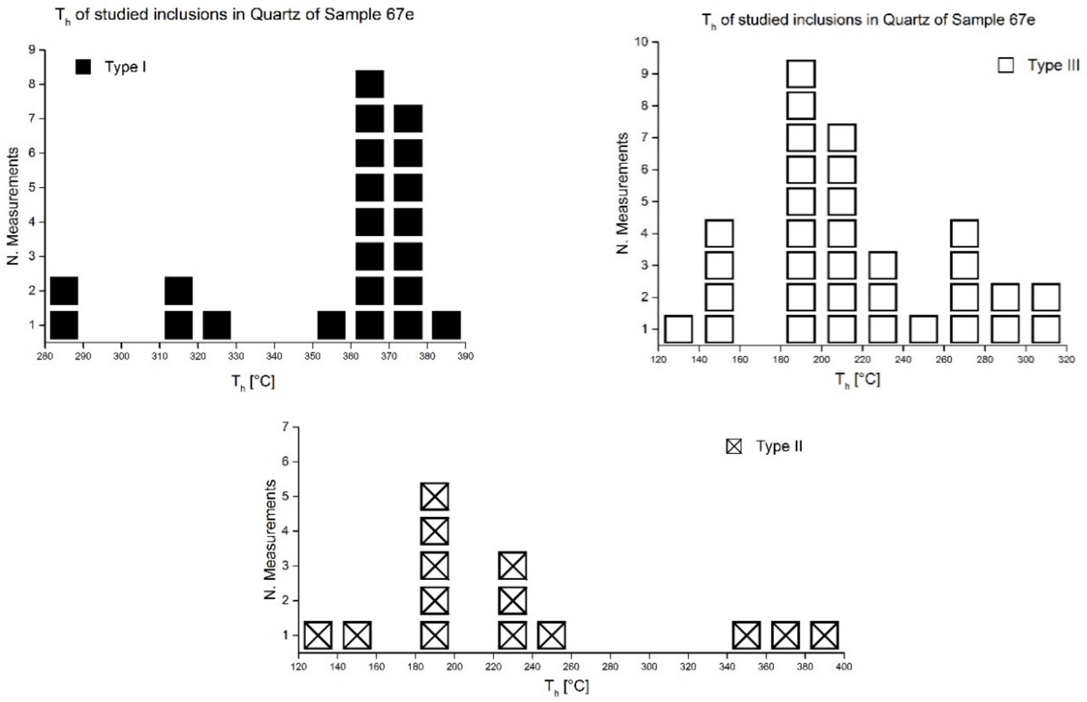

Fig. 104: Homogenization temperatures of the different types of fluid inclusions in sample 67E-QTZ3

The melting temperature of Type III varies from -2.6°C to +1.0°C. The homogenization temperature varies from 131.4°C to 316.7°C with the mode between 180°C and 220°C, similar to Type II inclusions (Fig. 104).

Because of the tiny size of Type IV, microthermometry could not be applied due to optical restrictions.

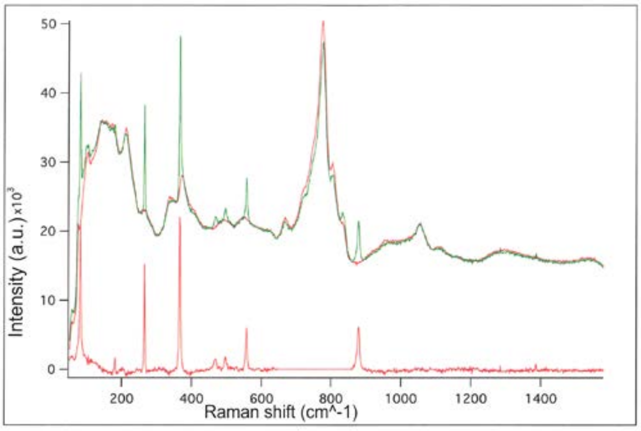

Fig. 105: Raman spectrum of sassolite (Raman shift peaks at 209, 500, 880 cm^{-1}) and of arsenolite (Raman shift peaks 85, 269, 370, 560 cm^{-1})

6.3.2. Sample 85A – QTZ1

In this sample (Fig. 106), only one type of fluid inclusion of altogether 36 studied fluid inclusions could be classified (Tab. A5 + A6 in the appendices). However, there must be at least two generations: one with the borate mineral sassolite in the liquid phase and one generation without sassolite, which is often long shaped (Fig. 107). The vapour phase of all inclusions consists of a brine with a high salinity. Only a few inclusions with mica and arsenolite, As_2O_3, an arsenic mineral (Fig. 105) in the liquid phases, were identified. The sizes of the inclusions range from 5 to 25 µm in diameter. The area bubble ratio varies from 10 to 40 vol%.

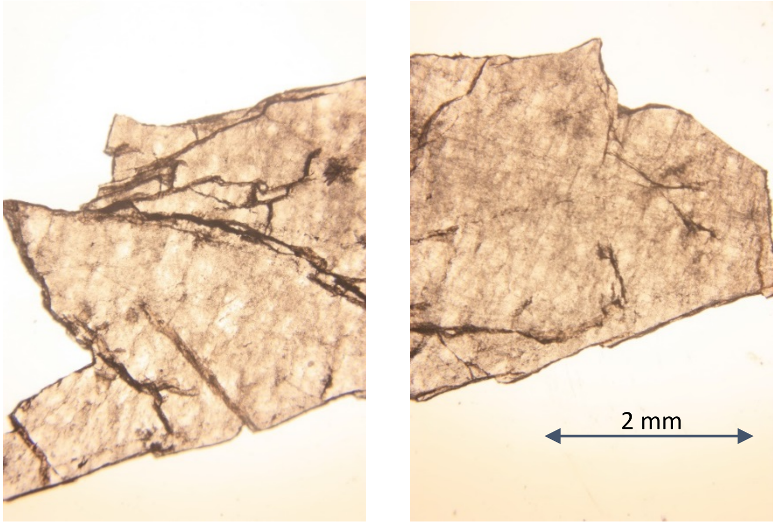

Fig. 106: Transmitted light images of sample 85A - QTZ 1

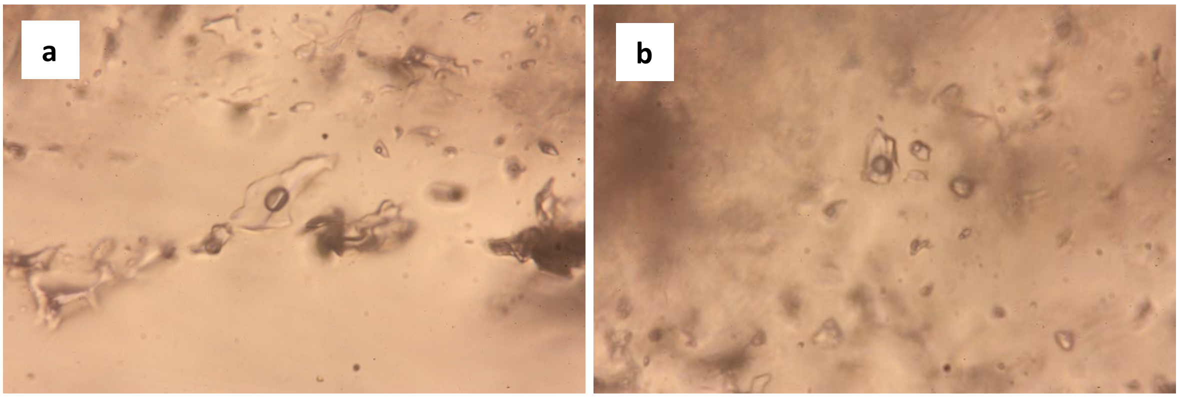

Fig. 107: Transmitted light image (a) of a long shaped inclusion without borate and transmitted light image (b) of fluid inclusions with borate (length of the images 0.1 mm)

The vapour phases consist of high amounts of CO_2 (the mode of x is around 0.95) and minor amounts of CH_4 (the mode of x is around 0.05). Nucleation occurred between -30°C and -40°C. The melting temperature of ice varies from -4.4°C to -0.4°C and the homogenization temperature from 191.2°C to 257.3°C with a mode between 220°C and 240°C (Fig. 108).

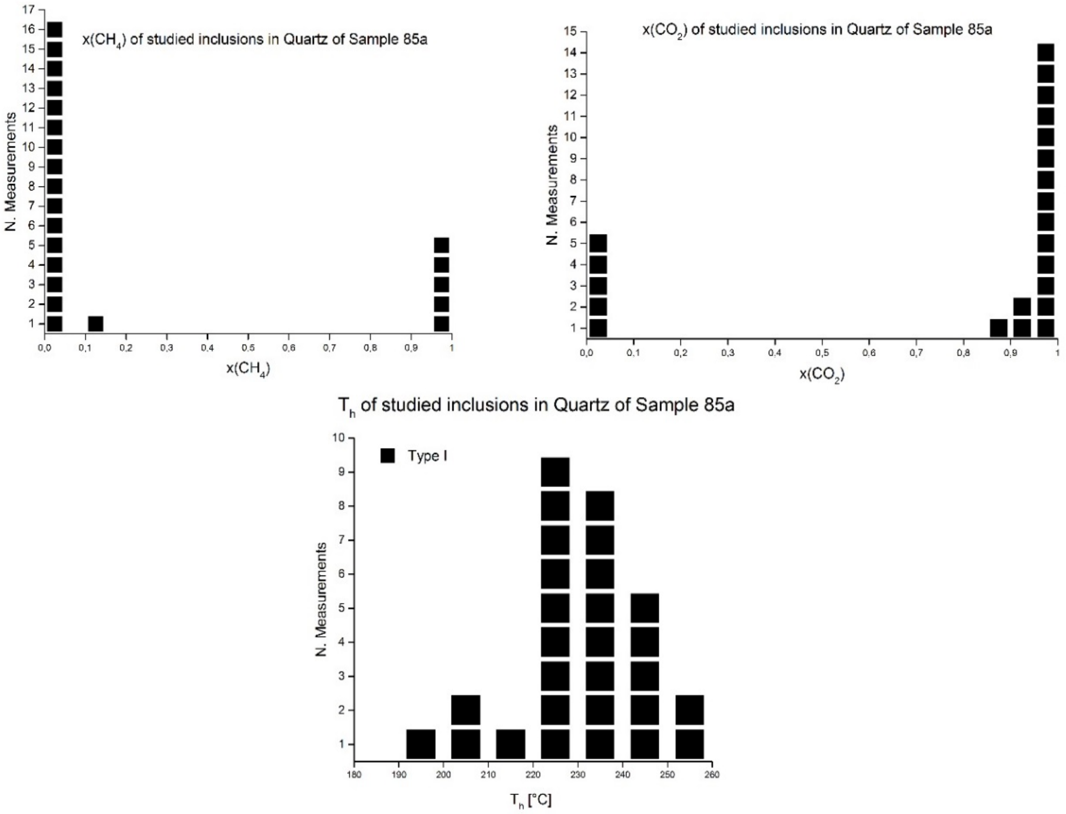

Fig. 108: Composition and homogenization temperature of the fluid inclusions in sample 85A-QTZ1

6.3.3. Sample 85A – QTZ2

Sample 85A – QTZ2 (Fig. 109) displays two types of altogether 40 studied fluid inclusions (Tab. A7 + A8 in the appendices). The liquid phase of these inclusions consists of a low salinity fluid.

Type I is characterized by regular shaped fluid inclusions with sizes from 5 to 10 µm in diameter, which do not contain borate in the liquid phase (Fig. 110). The area bubble ratio varies from 10 to 35 vol%. In Type I, the gas phases contain CO_2 and CH_4 and could be detected in every studied vapour bubble. The mode of $x(CO_2)$ is around 0.95 and the mode of $x(H_2)$ is around 0.05 (Fig. 111). The nucleation was observed between -30°C and -44°C. The melting temperature varies from -4.1°C to -2.2°C and the homogenization temperature from 199.0°C to 278.8°C with a mode between 230°C and 250°C, which is similar to those fluid inclusions found in sample 85A-QTZ1 (Fig. 111).

Fig. 109: Transmitted light image of sample 85A - QTZ2 (length of the image 4 mm)

Type II is classified by inclusions with an area bubble ratio from 20 to 40 vol% and an irregular shape, with sizes from 3 to 20 µm in diameter (Fig. 110). This type contains the borate mineral sassolite in the liquid phases. The gas phases CO_2 and CH_4 could not be detected in the vapour bubbles. The nucleation occurred between -30°C and -35°C. The melting temperature of this type varies from -3.2°C to -2.5°C and the homogenization temperature from 198.7°C to 245.1°C, with a mode between 230°C and 240°C (Fig. 111).

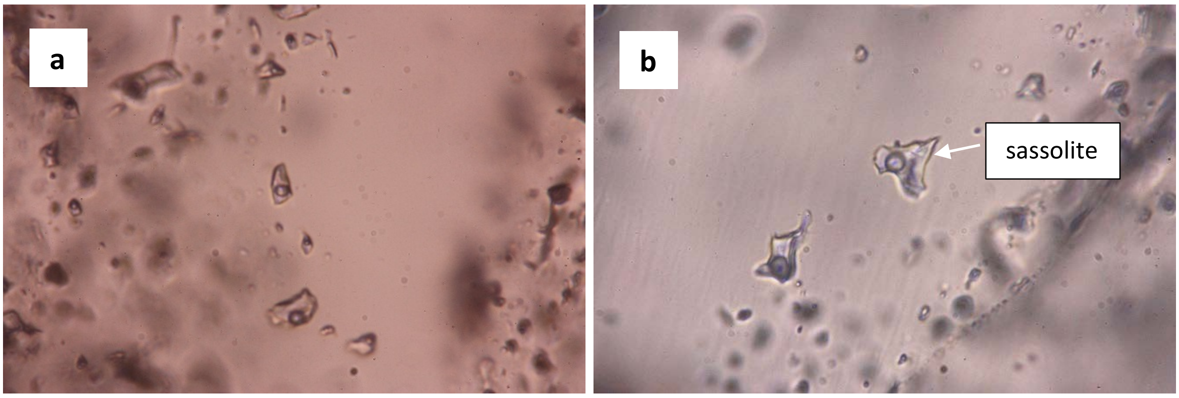

Fig. 110: Transmitted light image (a) of regular shaped inclusions of Type I and transmitted light image (b) of irregular shaped inclusions of Type II with sassolite (length of the images 0.1 mm)

In addition, some melt inclusions with solid phases could be identified, which belong to an earlier generation, but which are not suitable for microthermometry.

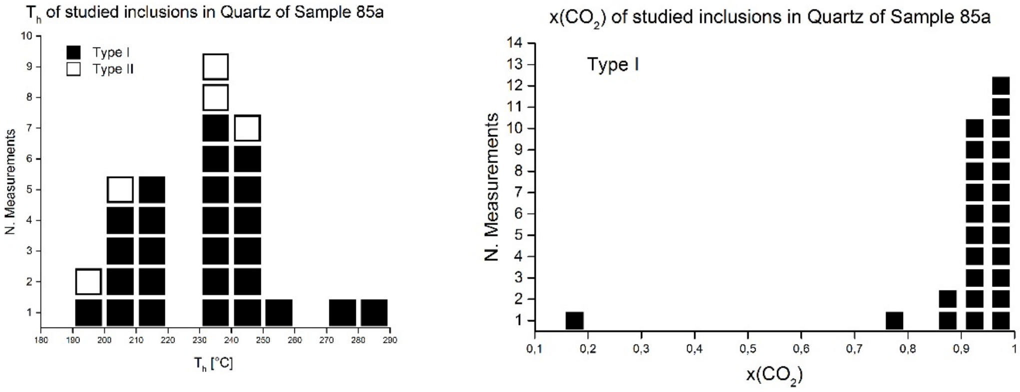

Fig. 111: The homogenization temperature and the composition of the fluid inclusions in sample 85A-QTZ2

6.3.4. Sample 85A – TUR1

In this tourmaline sample, two different types of altogether 41 studied fluid inclusions (Tab. A9 + A10 in the appendices) were classified (Fig. 112). The fluid phase of these inclusions consists of a low salinity fluid.

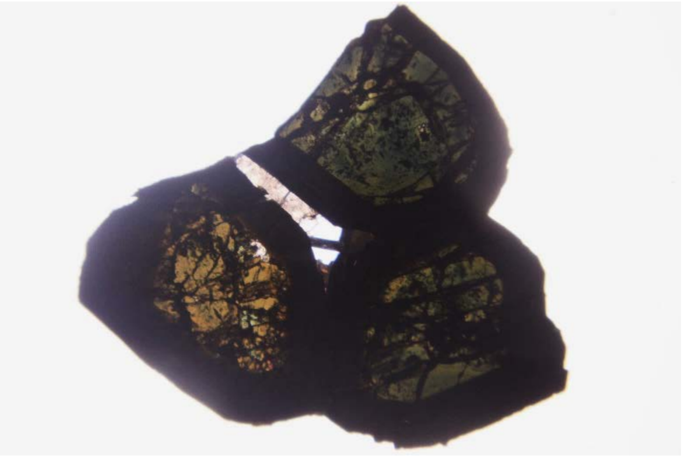

Fig. 112: Transmitted light image of sample 85A - TUR1 (length of the image 4 mm)

Several fluid inclusions display a disruptive fluorescence and because of the metastability of some inclusions and the solubility of sassolite, this mineral dissolves in the liquid phase even with the activation of the laser beam of the Raman spectroscopy.

Type I is characterized by large inclusions (from 10 to 100 µm in diameter), often with a high area bubble ratio (from 20 to 45 vol%). They are sometimes irregular shaped and show a dark vapour bubble (Fig. 113). Borate or other minerals could not be observed in the liquid phases of these inclusions. The gas phases contain CH_4 and sometimes CO_2 could be detected in the vapour bubbles of Type I. The melting temperature of Type I varies from -9.3°C to 0.2°C and the homogenization temperature from 286.3°C to 381.8°C, with a mode between 360°C and 380°C (Fig. 114).

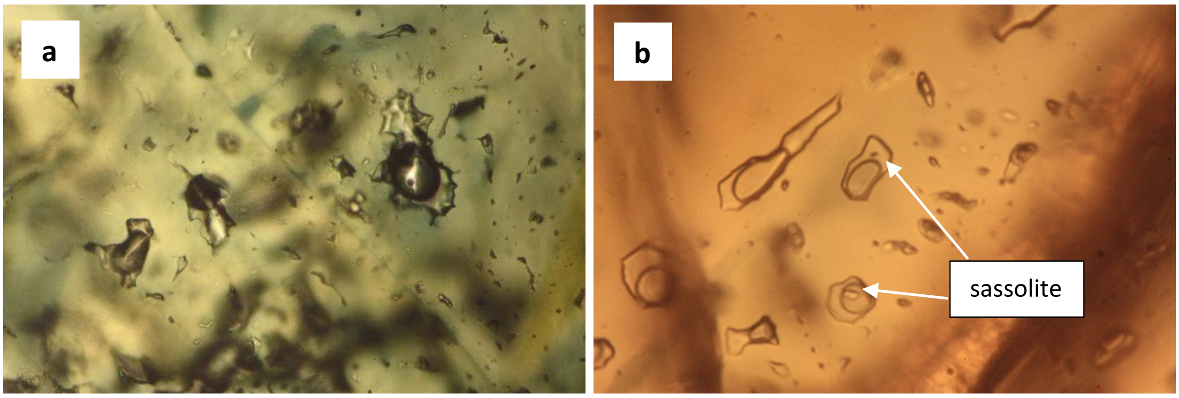

Fig. 113: Transmitted light image (a) of irregular shaped Type I fluid inclusions (length of the image 0.25 mm) and transmitted light image (b) of a large Type II inclusion with borate crystals (length of the image 0.1 mm)

Type II is classified by very large inclusions (from 20 to 200 µm in diameter) with a high are bubble ratio (from 40 to 55 vol%). They are regular shaped and they always contain borate crystals or even arsenolite (As_2O_3) in the liquid phases (Fig. 113).

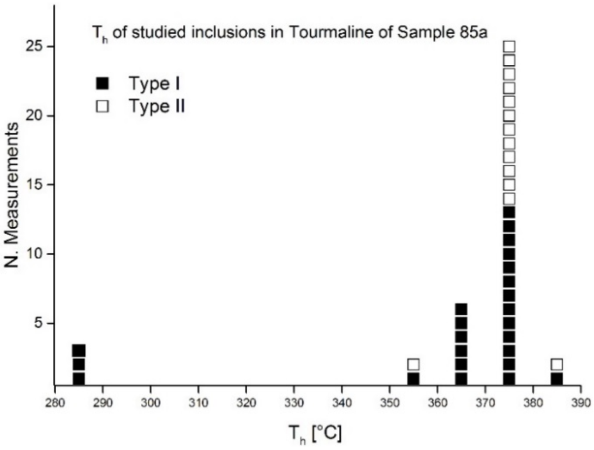

Fig. 114: Homogenization temperatures of the fluid inclusions in sample 85A-TUR1

Only small amounts of CO_2 and CH_4 were detected with Raman spectroscopy, which do not allow composition calculation. Two nucleation- and two melting temperatures were recognized during cooling or heating experiments of Type II. First nucleation occurrs between -10°C and -25°C and the second nucleation between -45°C and -50°C. The first melting temperature varies from -9.2°C to - 6.2°C and represents the melting of ice and the second melting temperature varies from +8.6°C to 25.8°C and likely represents the melting of borate. The homogenization temperature of Type II varies from 359.8°C to 381.3°C, with a mode between 370°C and 380°C (Fig. 114).

6.3.5. Example of the combination of Raman spectroscopy and microthermometry

The combination of Raman spectroscopy and microthermometry led to the identification of every species and phases at selected temperatures. As an example, an observation of one fluid inclusion of sample 67E-QTZ3 is described here in detail.

Fluid inclusion 1 (Fi1) contains CH_4 and CO_2 in the vapour phase and a columnar borate crystal in the liquid phase at room temperature (20°C) (Fig. 115 + Fig. 116). Fi1 is now cooled down to the temperature of -32°C, which is between the first and the second nucleation. A formation of ice and clathrate can be observed. Soon below this temperature, the vapour bubble experience a compression. The peak of the Raman spectrum of CH_4 is shrunk, a distinct peak beside the CH_4 peak is originated (clathrate peak) and the ice peak over the expanded Raman spectrum of water is displayed (Fig. 116). At -100°C and heated back at -50°C, there is still ice, clathrate and the borate crystal in the liquid phase. The vapour bubble still displays a compression (Fig. 115). During the heating process, a permanent recrystallization of ice can be seen, until the melting point of ice is attained. At 0°C (this stage is between the first and the second melting point), the ice spectrum is shrunk compared to the spectrum at -50°C with influence of the expanded water spectrum and the vapour bubble still experiences a little compression (Fig. 115 + Fig. 116). At +10°C, ice and clathrate are completely melted and the original stage is attained.

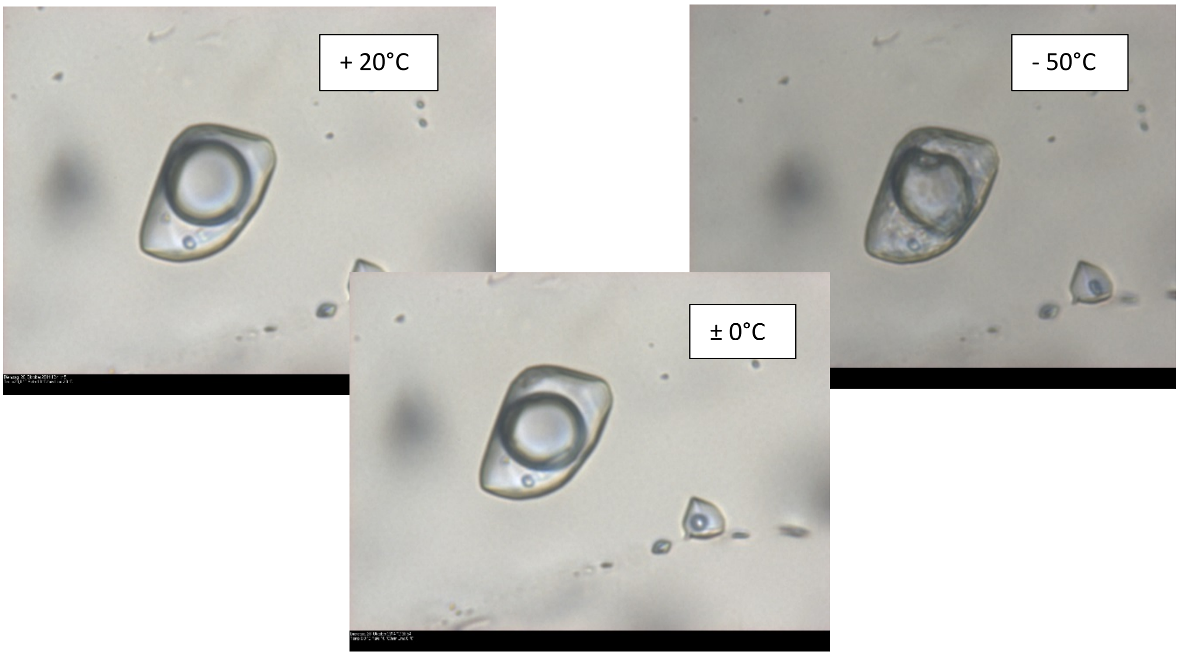

Fig. 115: Different stages of Fi1; length of the images 0.1 mm

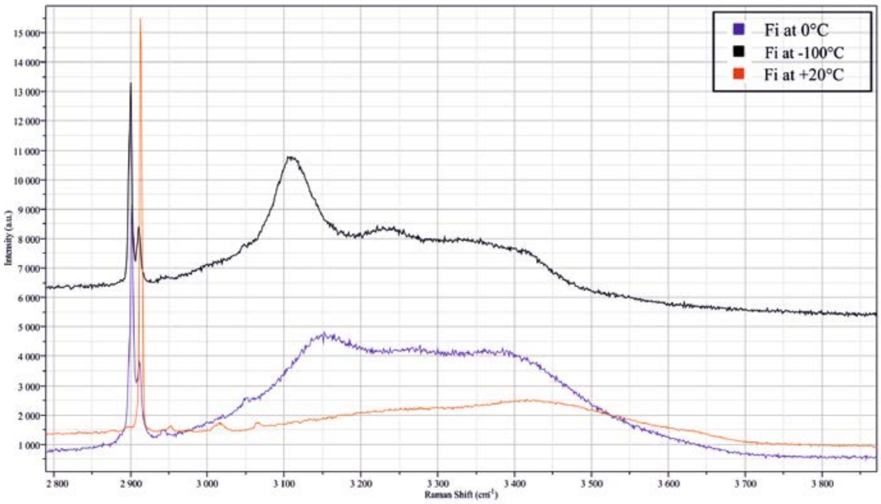

Fig. 116: Raman spectrum of Fi1 at different temperatures

7. Discussion and conclusions

In the course of this thesis, different rock samples and minerals of aplite, pegmatite dykes and tourmaline-rich veins have been analysed. With the aid of the electron microprobe, tourmaline could be divided clearly into different types with its structural formula. Every sample displays different types and even single tourmaline crystals with different colours could be identified from the core to the rim. Andalusite with its distinctive pink colour and pleochroism and cordierite could also be divided clearly (Tab. A14 in the appendices). Due to the occurrence of garnet and biotite in a coexistence in some samples, a geothermometry was calculated. In the end, some opaque minerals, especially columbite, were studied and the fluid inclusion research led to some information about the formation conditions of the aplite and pegmatite dykes (Tab. A3 - A10 in the appendices).

7.1. Tourmaline analyses

The tourmaline-supergroup minerals are specified with the general formula $X\ Y_3\ Z_6\ (T_6O_{18})\ (BO_3)_3\ V_3W$ according to the Subcommittee on Tourmaline Nomenclature (STN). The X-site can be divided into three principal groups based on the dominant species: alkali tourmalines (Na^+, K^+), calcic tourmalines (Ca^{2+}) and X-site-vacant tourmalines (□: vacancy). These groups are divided further, initially based on the W-site occupancy (dominated by OH^-, F^- or O^{2-}), then by the (actual or inferred) V-site occupancy (dominated by OH^-), next by the (actual or inferred) Y-site occupancy (dominated by Li^+, Mg^{2+}, Fe^{2+}, Mn^{2+}, Al^{3+}, Fe^{3+}, Cr^{3+}, Ti^{4+}) and finally by the (actual or inferred) Z-site occupancy (dominated by Al^{3+}, Mg^{2+}). The T-site is dominated by Si^{4+} and Al^{3+} and the B-site by B^{3+} (Henry et al. 2011). The most important tourmaline species are listed in Tab. 3.

Tab. 3: Structural formula types of some tourmaline species, modified after Hawthorne and Henry (1999)

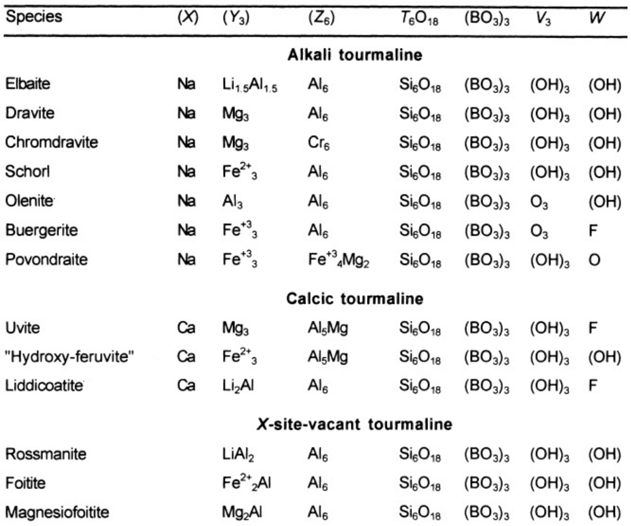

Species	(X)	(Y_3)	(Z_6)	T_6O_{18}	$(BO_3)_3$	V_3	W
			Alkali tourmaline				
Elbaite	Na	$Li_{1.5}Al_{1.5}$	Al_6	Si_6O_{18}	$(BO_3)_3$	$(OH)_3$	(OH)
Dravite	Na	Mg_3	Al_6	Si_6O_{18}	$(BO_3)_3$	$(OH)_3$	(OH)
Chromdravite	Na	Mg_3	Cr_6	Si_6O_{18}	$(BO_3)_3$	$(OH)_3$	(OH)
Schorl	Na	Fe^{2+}_3	Al_6	Si_6O_{18}	$(BO_3)_3$	$(OH)_3$	(OH)
Olenite	Na	Al_3	Al_6	Si_6O_{18}	$(BO_3)_3$	O_3	(OH)
Buergerite	Na	Fe^{+3}_3	Al_6	Si_6O_{18}	$(BO_3)_3$	O_3	F
Povondraite	Na	Fe^{+3}_3	$Fe^{+3}_4Mg_2$	Si_6O_{18}	$(BO_3)_3$	$(OH)_3$	O
			Calcic tourmaline				
Uvite	Ca	Mg_3	Al_5Mg	Si_6O_{18}	$(BO_3)_3$	$(OH)_3$	F
"Hydroxy-feruvite"	Ca	Fe^{2+}_3	Al_5Mg	Si_6O_{18}	$(BO_3)_3$	$(OH)_3$	(OH)
Liddicoatite	Ca	Li_2Al	Al_6	Si_6O_{18}	$(BO_3)_3$	$(OH)_3$	F
			***X*-site-vacant tourmaline**				
Rossmanite		$LiAl_2$	Al_6	Si_6O_{18}	$(BO_3)_3$	$(OH)_3$	(OH)
Foitite		Fe^{2+}_2Al	Al_6	Si_6O_{18}	$(BO_3)_3$	$(OH)_3$	(OH)
Magnesiofoitite		Mg_2Al	Al_6	Si_6O_{18}	$(BO_3)_3$	$(OH)_3$	(OH)

The electron microprobe analyses were calculated based on 31 anions (O atoms) and the assumption of OH = 4 *apfu* (atoms per formula unit). The occupancy can be estimated by using the stoichiometric H_2O (mass%) content. The B_2O_3 content was analysed (not calculated) due to the availability of appropriate diffracting crystals and synthetic boron nitride as a standard. The concentrations of B_2O_3 were reliable according to calculated concentrations from tourmaline of pegmatitic dykes. Finally, normalizations based on 15 cations (Y+Z+T) or 18 cations (Y+Z+T+B) were used for the various classifications.

Altogether 176 analyses of the samples 59B, 60A, 65C, 72C, 75D, 85A, 0A, 3A, 5B, 9C, 23F, 25A, 29D, 35B and TUR were performed (Tab. A11 in the appendices).

As a result, the tourmalines of Elba Island belong to the X-vacant tourmaline group (as primary tourmaline group) because of the lack of Na, Ca and K at the X-site. In general, Na is the dominant cation in the X-site, Fe^{2+} plays a predominant role in the Y-site. Al atoms fill the octahedral Z-site and partially the Y-site.

Most of the studied tourmalines consist of a foitite-schorl composition and some tourmalines of a dravitic or even elbaitic composition (Fig. 117).

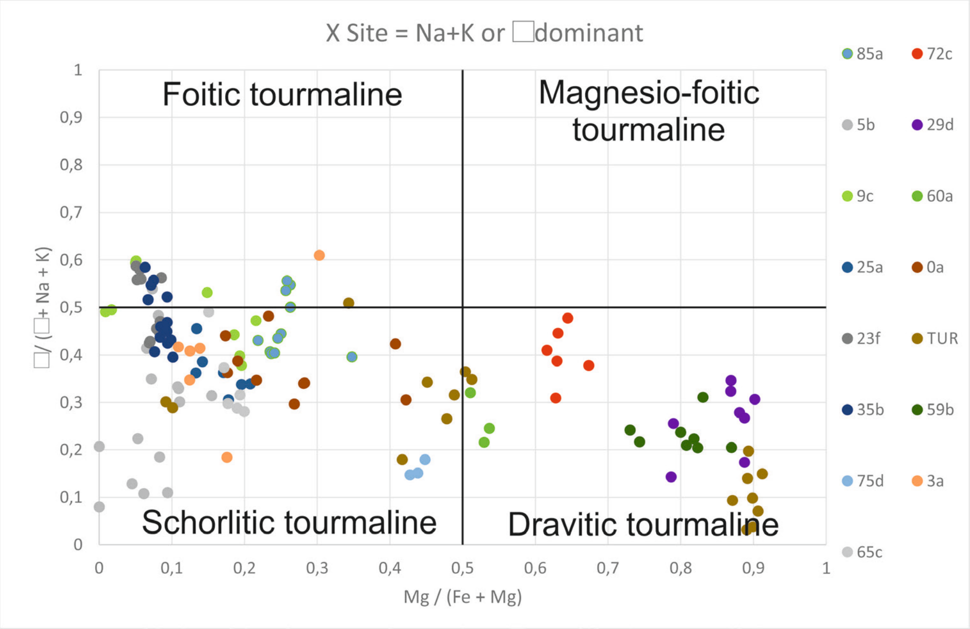

Fig. 117: The generalized tourmaline species based on Mg/(Mg+Fe) vs. □/(□+Na+K) ratios, modified after Henry et al. (2011)

In addition, the tourmaline composition can give information about the rock type with the most substituent elements plotted on Al-Fe(tot)-Mg and Ca-Fe(tot)-Mg ternary diagrams (Fig. 118).

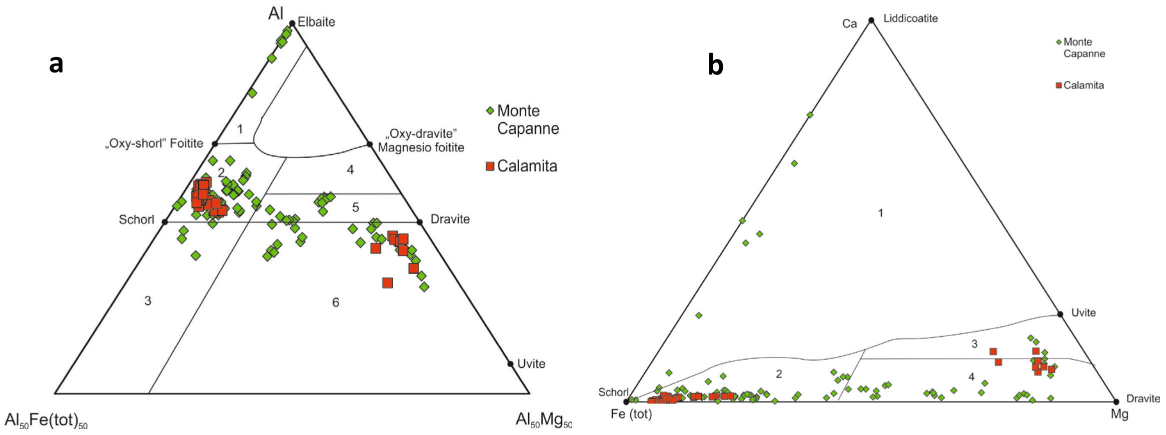

Fig. 118: Compositional diagram used for illustrating the host rock type: (a) ternary Al-Fe(tot)-Mg plot, 1= Li-rich granitoid pegmatites and aplites, 2= Li-poor granitoids and their associated pegmatites and aplites, 3=Fe^{3+}-rich quartz-tourmaline rocks, 4= Metapelites and metapsammites coexisting with an Al-saturating phase, 5= Metapelites and metapsammites not coexisting with an Al-saturating phase, 6= Fe^{3+}-rich quartz-tourmaline rocks, calc-silicate rocks, and metapelites. (b) ternary Ca-Fe(tot)-Mg plot, 1= Li-rich granitoid pegmatites and aplites, 2= Li-poor granitoids and their associated pegmatites and aplites, 3= Ca-rich metapelites, metapsammites, 4= Ca-poor metapelites, quartz-tourmaline rocks, modified after Henry and Guidotti (1985)

The tourmalines are divided into the tourmalines collected around the Monte Capanne pluton and into the tourmalines from the Calamita peninsula. The composition ranges from schorlitic to foitic tourmaline, and dravitic tourmaline in pegmatites around the Monte Capanne Pluton. The colourless tourmaline of the schorlitic group is a Mn-rich elbaitic tourmaline. At the Calamita peninsula, the tourmalines display two compositional groups of schorlitic and dravitic tourmaline.

Aurisicchio et al. (1999) mentioned that foitite-schorl crystals can be also found as overgrowth of elbaitic, polychrome (green, blue, yellow, pink, colourless) tourmalines, crystallised at the beginning of a hydrothermal stage as paragenesis 1 or crystallised during the circulation of hydrothermal fluids along fractures by the Monte Capanne pluton as paragenesis 2 (late hydrothermal stage). In the case of paragenesis 1, the tourmaline overgrowth occurred in hydrothermal fluids, directly derived from the crystallization of the pegmatite body. Indeed, there is no structural evidence of a significant opening of the pegmatite system. The increase of Fe in the late-stage tourmaline could be provided by the reaction of the primary minerals with the late, low-temperature, fluids of the cavities. The aluminous composition of the fluids could be responsible for the unusual alkali-deficient composition of the tourmaline. In the case of paragenesis 2, hydrothermal fluids reacted with the more evolved minerals (resulting in alteration, corrosion and mineral replacement) and generated the crystallization of schorlitic tourmaline together with quartz, K-feldspar and albite. These fluids circulated in open system condition (Aurisicchio et al. 1999). For comparison, in the course of this thesis, elbaitic, dravitic tourmaline crystals were found as overgrowth of foitite-schorl crystals (e.g. samples 5B, TUR).

Examples of the distinctive zoning of the tourmaline crystals and their changes in the structural formula is shown in Fig. 119. The common core-to-rim zoning displays an Al, Mg and Ca increase and a Fe decrease.

85a

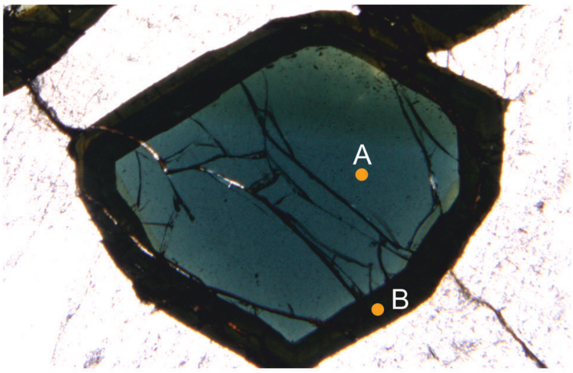

	X			Y_3					Z_6	T_6		B_3	V_3	W
Element	Na	Ca	K	Mg	Fe	Mn	Al	Ti	Al	Si	B	B	OH	OH
A	0,45	0,01	0,01	0,470	1,361	0,023	0,80	0,042	6	5,84	0,16	3,30	3,00	1,03
B	0,57	0,04	0,01	0,750	1,408	0,014	0,59	0,080	6	5,74	0,26	3,16	3,00	1,02

59b

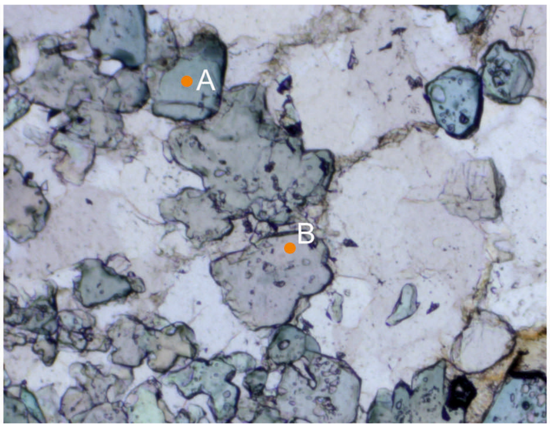

	X			Y_3					Z_6	T_6			B_3	V_3	W	
Element	Na	Ca	K	Mg	Fe	Mn	Al	Ti	Al	Si	Al	B	B	OH	F	OH
A	0,64	0,13	0,01	1,92	0,66	0,00	0,15	0,01	6,00	5,83	0,00	0,17	3,25	3,00	0,00	1,01
B	0,74	0,05	0,01	2,19	0,47	0,01	0,33	0,00	6,00	6,21	0,13	0,00	2,67	3,03	0,08	0,92

5b

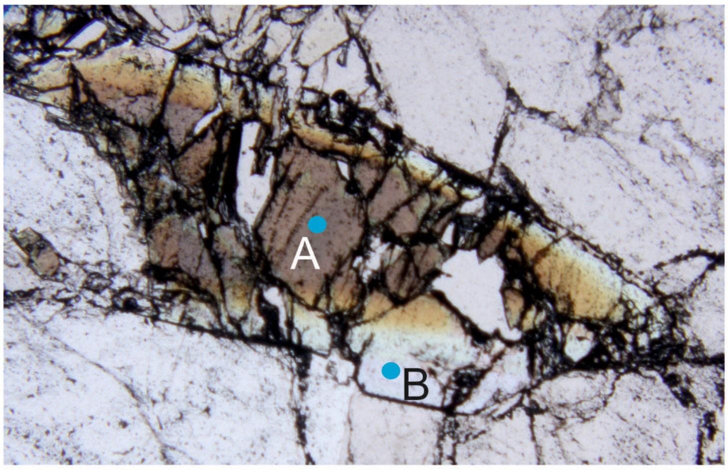

	X			Y_3					Z_6	T_6	B_3		V_3	W	
Element	Na	Ca	K	Mg	Fe	Mn	Al	Ti	Al	Si	B	Si	OH	F	OH
A	0,74	0,05	0,01	2,19	0,47	0,01	0,34	0,00	6,12	6,00	2,67	0,21	3,00	0,08	0,92
B	0,73	0,16	0,00	0,02	0,18	0,75	1,84	0,05	6,00	6,12	3,04	0	3,00	0,54	0,46

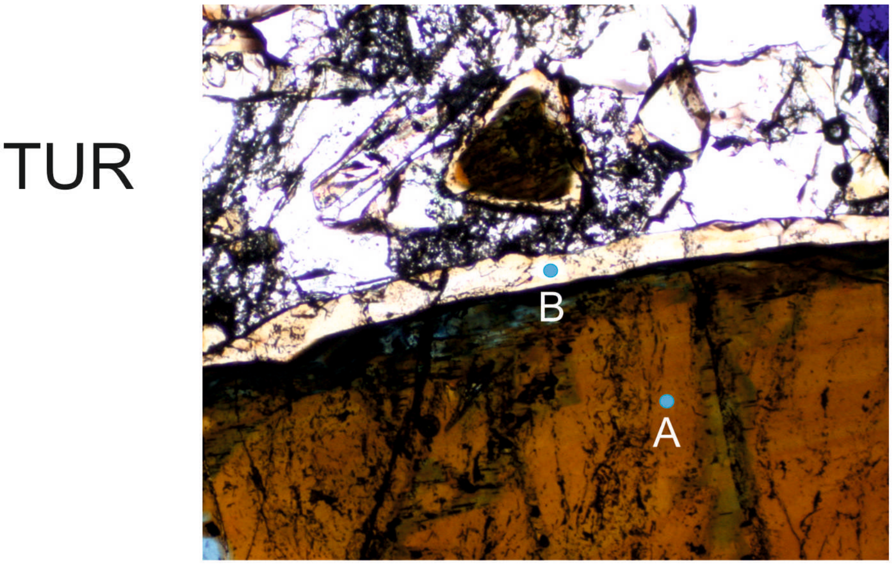

	X			Y_3					Z_6	T_6		B_3	V_3	W
Element	Na	Ca	K	Mg	Fe	Mn	Al	Ti	Al	Si	B	B	OH	OH
A	0,60	0,08	0,01	1,11	1,16	0,00	0,26	0,15	6,00	5,73	0,27	3,32	3,00	1,00
B	0,58	0,27	0,00	2,43	0,23	0,00	0,03	0,04	6,00	5,97	0,04	3,26	3,00	1,00

Fig. 119: Examples of tourmaline zoning and their change in the structural formula

7.2. Geothermometry with garnet and biotite

Geothermobarometry is a fundamental technique to determine magmatic conditions. The methods are usually based on the p-T dependency of equilibrium constants (K_D) and equilibrium curves of mineral reactions. According to the equitation of the "Gibbs free energy" in (1), reactions that have a strong temperature dependency (high ΔS) are used as geothermometers, whereas those with a strong pressure dependency (high ΔV) are usually used as geobarometers.

$$(1) \qquad \Delta G_{p,T} = \Delta H_{p,T} - T \cdot \Delta S_{p,T} + R \cdot T \cdot \ln(K) = 0$$

Exchange reactions from garnet and biotite are characterized by the interchange of atoms, in this case with the cation pair Mg/Fe^{2+}. Yet their application is problematical due to subsolidus re-equilibration effects down to a temperature of about 500°C, which influence their distribution coefficient (K_D). The Mg-Fe partitioning (exchange equilibrium) has been experimentally studied by Ferry and Spear (1978) in the temperature range of 550°C – 800°C at 2.07 kbar with metamorphites, within the limit value (Ca+Mn)/(Ca+Mn+Fe+Mg) = 0.2 and if the Fe-Mg solid solution of garnet is close to an ideal one. The garnet samples of Elba do sometimes exceed this value because of the enrichment in Ca and Mn. An improvement of the garnet-biotite geothermometer was discussed by Gulbin (2011a) and led to new specified equations minimizing the uncertainties in the determination of the temperature. Among the considered versions of the biotite-garnet geothermometers, the least-sloped trends are related to the calibration of Kaneko and Miyano (2004), as shown in equation (2)

$$(2)\quad T = \frac{12963.3 - (P-1)(-0.098 + W^{V,Grt}) - W^{H,Grt} + 5222.5(X_{Mg} - X_{Fe})^{Bt} + 85531.7X_{Al}^{Bt} + 103663.3X_{Ti}^{Bt}}{R\ln K_D + 2.627 - W^{S,Grt} + 4.079(X_{Mg} - X_{Fe})^{Bt} + 103.290X_{Al}^{Bt} + 123.463X_{Ti}^{Bt}},$$

where the corrections for the nonideality of the garnet solid solution $W^{H,Grt}$; $W^{S,Grt}$; and $W^{V,Grt}$ are calculated on the basis of the Berman model (Berman 1990; Kaneko and Miyano 2004). The ΔT_{Mn} and ΔT_{Ca} increments obtained from this calibration vary from -6 to 38°C and from -12 to 30°C, respectively. The temperature estimates are characterized by the minimal standard deviations (11–15°C) and ranges (37–63°C) (Gulbin 2011a; Gulbin 2011b). The calculated temperatures of coexisting garnet-biotite of sample 57A vary from 573°C to 617°C (Fig. 120).

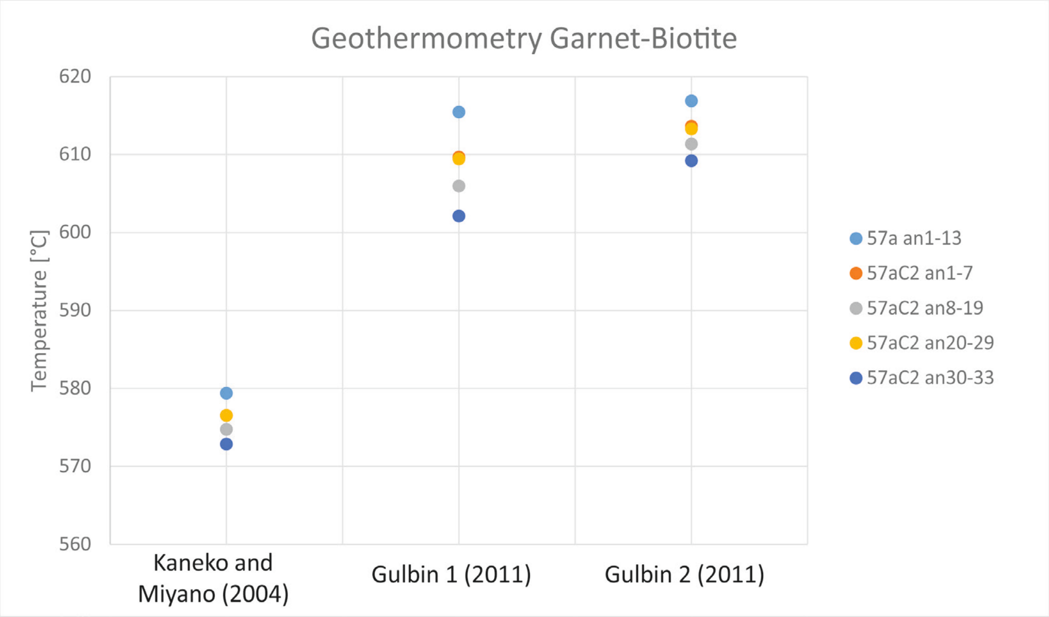

Fig. 120: The calculated temperatures of coexisting garnet-biotite in sample 57A; modified after Kaneko and Miyano (2004), Gulbin (2011a), Gulbin (2011b)

Altogether 58 analyses of the samples 57A and 65C were performed (Tab. A12 + A13 in the appendices). The electron microprobe analyses were calculated based on 12 anions (O atoms) for the garnets and biotites and an assumption of OH = 2 *apfu* (atoms per formula unit) was used for the biotites. Normalizations based on 8 cations were used for the recalculation of Fe^{3+} and for the calculation of the end-members of the garnets. All garnet analyses show enrichments in almandine (the iron-aluminium garnet) (Tab.4)

Tab. 4: Calculation of end-members of measured garnets, in percentage

Analysis	**57aan6**	**57aC2an7**	**57aC2an12**	**57aC2an18**	**57aC2an19**	**57aC2an20**	**57aC2an21**	**57aC2an24**	**57aC2an34**
Pyrope	3,07	3,32	2,76	3,24	3,41	3,32	3,36	2,58	2,90
Almandine	78,77	77,02	75,57	77,96	78,08	77,67	75,06	76,61	75,71
Spessartine	16,89	18,34	20,50	17,75	17,39	18,13	19,24	19,60	19,87
Andradite	1,77	2,98	0,55	6,49	0,44	1,17	2,58	0,76	0,18
Uvarovite	0,08	0,00	0,00	0,00	0,06	0,16	0,06	0,00	0,01
Grossular	0,00	0,00	0,62	0,00	0,61	0,00	0,00	0,39	1,33

7.3. Cordierite analyses

Five analyses of cordierite were performed with sample 72C (Tab. 5). The normalized structural formula which was calculated based on 18 anions (O atoms), displays the Mg analogue (cordierite) in the cordierite-sekaninaite series $(Mg,Fe)_2Al_3(AlSi_5O_{18})$. Na, Mn, Ti and Ca are impurities and show a possible alteration into pinite. Pegmatitic vein cordierites generally have more Na_2O, which fit to these cordierite samples.

Tab. 5: Chemical composition of cordierite and normalized structural formula

	72ccordan1	**72ccordan2**	**72ccordan3**	**72ccordan4**	**72ccordan5**
Na_2O	1,04	1,11	1,09	1,05	0,97
CaO	0,00	0,01	0,00	0,01	0,00
FeO	6,54	6,27	6,03	6,15	6,30
K_2O	0,03	0,01	0,01	0,03	0,04
MgO	7,50	7,71	7,79	7,71	8,04
SiO_2	48,25	48,36	48,29	49,19	48,51
TiO_2	0,00	0,01	0,00	0,01	0,00
Al_2O_3	32,56	32,82	32,72	32,20	32,09
MnO	0,62	0,59	0,57	0,58	0,57
Total	96,55	96,90	96,50	96,90	96,52
	Structural formula on the basis of 18 oxygens				
Si	5,042	5,029	5,035	5,104	5,063
Al	4,010	4,023	4,021	3,938	3,948
Ti	0,000	0,001	0,000	0,000	0,000
Mg	1,169	1,195	1,211	1,193	1,251
Fe	0,571	0,546	0,526	0,533	0,550
Mn	0,055	0,052	0,050	0,051	0,050
Ca	0,000	0,001	0,000	0,001	0,000
Na	0,211	0,224	0,221	0,211	0,196
K	0,004	0,002	0,001	0,003	0,005
Mg/(Mg+Fe+Mn)	0,651	0,667	0,678	0,671	0,676

7.4. Andalusite analyses

Altogether 52 analyses of pink and white andalusite of the samples 60A, 64A, 67E, 72C, 25A and 35B were performed (Tab. A14 in the appendices). The analyses were calculated based on 20 anions (O atoms). The pink colour is directly related to the Fe content and Fe is roughly negatively correlated with Al (Fig. 121).

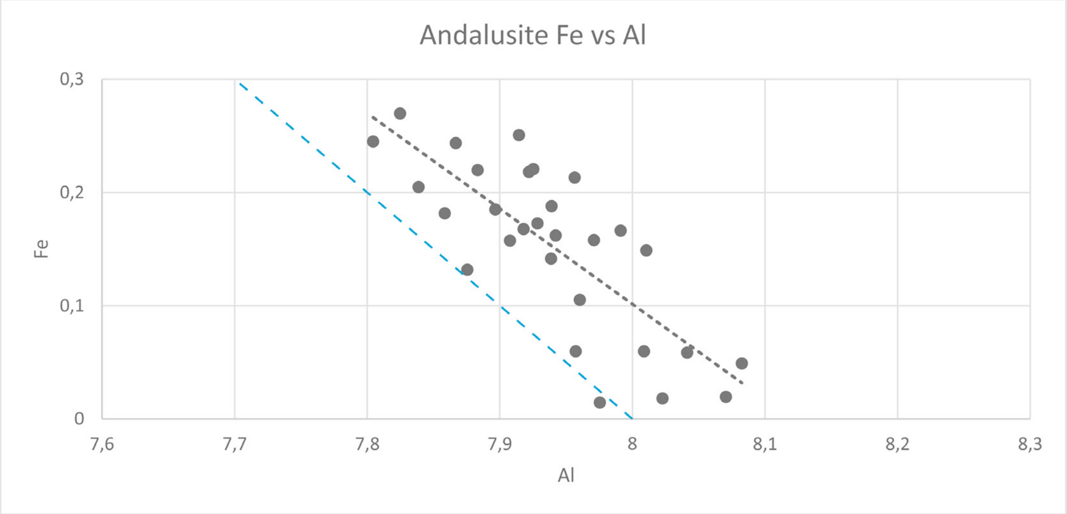

Fig. 121: Composition of Andalusite in a Fe vs Al diagram with a trend line (black) and the theoretical line (blue)

7.5. Oxide analyses

14 analyses of the samples 59B, 67E and 1J were performed. The analyses were calculated based on 2 anions (O atoms) (Tab. 6). The rutiles are a Nb-enriched and Fe-bearing variety of rutile, with the general formula (Ti,Nb,Fe,Ta,Sn)O_2. Aurisicchio et al. (2002) described these rutiles as niobian rutiles of granitic pegmatites, where Ti is the dominant element, attaining 0.8 *apfu*. The remaining 0.2 *apfu* consists of Fe, Nb, Sn, Al, W, Mn, Ta, Cr, Zr and Mg. Rutile contains up to 7.0 mass% Nb_2O_5, 4.3 mass% SnO_2, 3.9 mass% Ta_2O_5 and 11.5 mass% FeO.

Cassiterite was found several times, but the analysis with a total mass% of 83.6 led to the assumption that cassiterite is enriched by other trace elements (sample 59b cas of Tab. 6). Uraninite was also found several times, especially in sample 1J (Fig. 122) and is represented by purely UO_2. The other oxides were already discussed in other chapters.

Tab. 6: Representative compositions of niobian rutile and cassiterite (sample 59b cas)

	59b cas	59ban1	59ban2	59ban3	59ban4	59ban5	59ban6	67ean1	67ean2	67ean3	67ean4	67ean5	67ean6
MgO	0,09	0,00	0,00	0,00	0,00	0,00	0,00	0,00	0,00	0,00	0,00	0,00	0,00
Nb_2O_5	0,06	4,92	5,71	5,07	5,90	6,58	4,86	6,30	6,51	6,98	6,62	6,83	6,03
SnO_2	81,52	3,17	3,98	3,78	3,83	3,37	3,69	4,29	4,30	4,07	4,34	4,12	4,09
Cr_2O_3	0,00	0,41	0,29	0,17	0,20	2,46	0,11	0,01	0,01	0,06	0,01	0,00	0,01
TiO_2	1,21	78,57	76,63	78,82	75,20	73,72	77,54	74,09	73,20	73,79	73,36	73,87	75,34
Al_2O_3	0,00	0,21	0,17	0,17	0,20	0,19	0,23	0,27	0,24	0,22	0,21	0,25	0,18
ZrO_2	0,09	0,06	0,09	0,08	0,07	0,05	0,07	0,06	0,08	0,04	0,09	0,05	0,08
WO_3	0,00	1,57	0,65	0,70	0,61	1,38	1,48	0,30	0,30	0,27	0,45	0,48	0,31
FeO	0,15	8,84	9,90	9,00	10,44	9,03	9,43	10,75	11,55	11,49	11,10	10,85	10,21
MnO	0,38	0,13	0,14	0,15	0,17	0,11	0,21	0,20	0,16	0,18	0,22	0,17	0,15
Ta_2O_5	0,07	1,95	2,72	2,12	3,37	3,49	3,20	3,90	3,47	3,42	3,46	2,62	3,21
Total	83,56	99,82	100,28	100,07	99,99	100,37	100,82	100,17	99,82	100,51	99,84	99,24	99,60
				Structural formula on the basis of 2 oxygens (two anions and one cation)									
Mg	0,004	0,000	0,000	0,000	0,000	0,000	0,000	0,000	0,000	0,000	0,000	0,000	0,000
Nb	0,001	0,032	0,038	0,033	0,040	0,044	0,032	0,042	0,044	0,047	0,045	0,046	0,040
Sn	0,962	0,018	0,023	0,022	0,023	0,020	0,022	0,025	0,026	0,024	0,026	0,025	0,024
Cr	0,000	0,005	0,003	0,002	0,002	0,029	0,001	0,000	0,000	0,001	0,000	0,000	0,000
Ti	0,027	0,861	0,845	0,862	0,837	0,819	0,851	0,828	0,823	0,823	0,824	0,829	0,840
Al	0,000	0,004	0,003	0,003	0,004	0,003	0,004	0,005	0,004	0,004	0,004	0,004	0,003
Zr	0,001	0,000	0,001	0,001	0,001	0,000	0,001	0,001	0,001	0,000	0,001	0,000	0,001
W	0,000	0,006	0,003	0,003	0,002	0,005	0,006	0,001	0,001	0,001	0,002	0,002	0,001
Fe	0,004	0,108	0,121	0,110	0,129	0,112	0,115	0,134	0,144	0,142	0,139	0,136	0,127
Mn	0,010	0,002	0,002	0,002	0,002	0,001	0,003	0,003	0,002	0,002	0,003	0,002	0,002
Ta	0,001	0,008	0,011	0,008	0,014	0,014	0,013	0,016	0,014	0,014	0,014	0,011	0,013

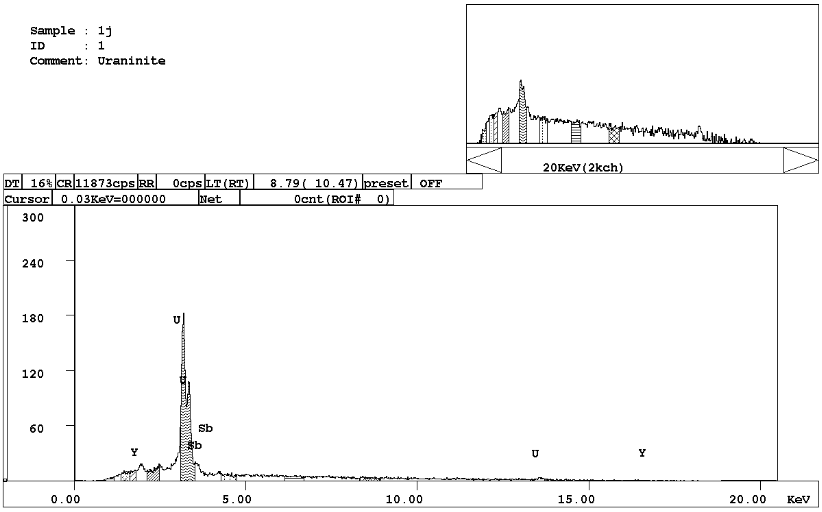

Fig. 122: EDS spectrum of uraninite

7.6. Nb-Ta oxide analyses

Six analyses of the samples 59B, 3A were performed. The analyses were calculated on the basis of 6 anions (O atoms).

Complex metamict Nb-Ta oxides occur as members of the euxenite-polycrase group, (Y,Ca,Ce,U,Th)$(Nb,Ta,Ti)_2O_6$. Aurisicchio et al. (2002) described the euxenite-(Y), a Nb-dominant phase, which occurs often in the pegmatites of Elba Island, associated with cassiterite and niobian rutile. Polycrase-(Y) occurs together with columbite and tourmaline and shows trends from Y-rich to U-rich compositions. The euxenite-polycrase group is represented by the samples 3Aan2REE and 35ban2REE and contains up to 34.0 mass% Nb, 22.0 mass% Y_2O_3, 11.8 mass% UO_2, 10.5 mass% WO_3 and 13.0 mass% Ta_2O_5. Semi-quantitative analyses of REE with the elements Sm, Gd, Dy, Ho, Er and Yb were also performed due to the low total mass% (Tab. 7).

Tab. 7: Chemical compositions of Nb - Ta oxides

	3A	**3Aan2REE**	**35b**	**35ban2REE**	**35b an3**	**35b an4**
SiO_2	0,25	0,56	0,48	2,49	0,22	0,27
Y_2O_3	0,13	22,03	1,96	14,62	0,06	0,11
TiO_2	4,88	1,22	5,24	1,14	5,44	1,85
Nb_2O_5	47,99	30,17	55,85	33,95	54,51	56,10
Ta_2O_5	15,66	12,99	6,67	4,16	9,29	11,94
CaO	0,00	1,45	2,14	2,48	0,00	0,00
UO_2	0,20	6,26	0,91	11,64	0,07	0,07
MnO	4,61	0,01	1,50	0,00	1,27	2,38
SnO_2	0,10	0,00	0,01	0,00	0,03	0,03
FeO	11,92	0,31	13,44	1,63	13,46	16,33
Sc_2O_3	2,17	0,19	2,36	0,09	5,00	0,37
WO_3	8,53	10,54	13,88	1,78	10,74	7,93
ZrO_2	0,32	0,04	0,31	0,00	0,89	0,11
HfO_2	0,02	0,00	0,01	0,00	0,08	0,01
Total	96,77	85,75	104,75	73,98	101,06	97,48
		Semi-quantitative analyses of REE				
Sm		0,969		2,108		
Gd		1,663		2,529		
Dy		3,319		3,218		
Ho		1,795		0,487		
Er		2,727		1,589		
Yb		4,433		1,923		
		Structural formula on the basis of 6 oxygens (3 cations)				
Si	0,015	0,044	0,027	0,213	0,013	0,017
Y	0,004	0,919	0,058	0,664	0,002	0,004
Ti	0,228	0,072	0,220	0,073	0,234	0,086
Nb	1,347	1,069	1,410	1,311	1,411	1,562
Ta	0,264	0,277	0,101	0,097	0,145	0,200
Ca	0,000	0,122	0,128	0,227	0,000	0,000
U	0,003	0,109	0,011	0,221	0,001	0,001
Mn	0,242	0,001	0,071	0,000	0,061	0,124
Sn	0,002	0,000	0,000	0,000	0,001	0,001
Fe	0,619	0,020	0,628	0,116	0,645	0,841
Sc	0,117	0,013	0,115	0,006	0,249	0,020
W	0,137	0,214	0,201	0,039	0,159	0,127
Zr	0,010	0,002	0,008	0,000	0,025	0,003
Hf	0,000	0,000	0,000	0,000	0,001	0,000

The columbite-tantalite group of Elba Island is represented by a composition of higher amounts of Nb, Ta, Fe, Mn and smaller quantities of Ti, W, Sc, Mg, Na as described by Aurisicchio et al. (2002). This group is represented by the samples 3A, 35B, 35Ban3 and 35Ban4 (Tab. 7). The samples contain up to 56.1 mass% Nb_2O_5, 15.7 mass% Ta_2O_5, 16.3 mass% FeO, 13.9 mass% WO_3, 5.0 mass% Sc_2O_3 and 4.6 mass% MnO. Only a few times Mn was a dominant phase, therefore often (Fe)-columbites were identified.

According to Aurisicchio et al. (2002), the presence of Ti, Y and REE is typical of the rare-element type of granitic pegmatite, because the parent granite derives from the mixing of peraluminous magma with batches of mantle-derived basic magma. A strong enrichment in boron during the entire evolution marks the LCT pegmatite. The presence of polychrome tourmaline, ranging from schorl to elbaite, testifies to the changing compositions of the pegmatitie-forming melt – fluid system with progressive crystallization, the stability of each composition being related to specific conditions of P, T and X. Two distinct stages of late crystallization have been recognized. The early saturation of the volatile-enriched melt in a vapour phase gave rise to pockets enriched in relatively primitive phases containing Ti-, Nb-, Fe-, Y and the heavy rare earth elements, whereas a later stage of vapour saturation gave rise to pockets containing an assemblage of evolved minerals of Mn, Ta and W.

7.7. Discussion of the results of the fluid inclusion research

The pressure-temperature conditions of pegmatites can be calculated based on fluid inclusions, but the more complex the inclusions are, the more complex is the calculation. One example for this calculation of one fluid inclusion is mentioned below.

A fluid inclusion enclosed in quartz (F19 in the sample 85A-QTZ1) shows a melting temperature at -3.9°C (T_m) and a homogenization temperature at 241.3°C (T_h). The vapour phase consists of CO_2 and CH_4 and the area bubble ratio is 17 vol%. The formation of clathrate can be observed at low temperatures (below -10°C).

The ice and the clathrate melting occur at approximately similar temperatures, so a Q1 melting of clathrate can be assumed. The gas composition is 0.9649 CO_2 and 0.0351 CH_4 and allows a specific Q1 calculation for this gas composition. The T_m of ice and the T_m of clathrate are corresponding to a specific salinity, which results in 0.7095 mol NaCl per kg H_2O (3.975 mass% NaCl) at Q1. The gas density at this condition is 2150.3 cm^3/mol (very low density). The liquid density at Q1 is approximately 18.26 cm^3/mol based on a binary H_2O-NaCl system (the gas solubility is very low and can be neglected). The calculated density of the total inclusion according to these numbers is 21.96 cm^3/mol. The fluid inclusion can be treated as a binary H_2O-NaCl system, consequently the calculation of Driesner and Heinrich (2007) can be used for the fluid properties at T_h and at trapping conditions. The T_h at 241.3°C corresponds to a density of 21.44 cm^3/mol, which is very similar to the previously calculated number (Bakker 2003).

At 600°C, this fluid has a pressure of 550 MPa. This temperature is taken from the garnet/biotite geothermometer, and the trapping conditions correspond to this 550 MPa.

These conditions correspond to similar P-T estimations of pegmatite formation at relative low pressure conditions (e.g. Sowerby and Keppler 2002).

London (2008) assumed approximately 300 MPa for the entrapment of the fluid components of the inclusions and temperatures of the main pegmatitic stage cluster between 550°C and 650°C (around the low-temperature end of their calibration).

Because of the identification of borate during the fluid inclusion research, following assumptions can be made: there are big amounts of borate in the fluid inclusions enclosed in tourmaline grains and minor amounts of borate in the fluid inclusions enclosed in quartz grains. Therefore, Boron-rich fluids should be migrated first, and at this time the tourmaline was formed. The quartz was formed later with Boron-poor fluids. In addition, this assumption corresponds to the higher T_h of tourmaline, because tourmaline was formed at higher temperatures. Both, fluid inclusions enclosed in tourmaline and in quartz, are related, but they belong to different generations.

8. References

Abbate E, Bortolotti V, Passerini P, Principi G, Treves B (1994) Oceanisation processes and sedimentary evolution of the Northern Apennine ophiolite suite: a discussion. *Memoire della Societa Geologica Italiana* 48:117–136.

Aurisicchio C, Ottolini L, Pezzotta F (1999) Electron- and ion-microprobe analyses, and genetic inferences of tourmalines of the foitite-schorl solid solution, Elba Island (Italy). *European Journal of Mineralogy* 11(2):217–226.

Aurisicchio C, Vito C de, Ferrini V, Orlandi P (2002) Nb and Ta Oxide Minerals in the Fonte del Prete Granitic Pegmatite Dike, Island of Elba, Italy. *The Canadian Mineralogist* 40:799–814.

Babbini A, Bortolotti V, Corti S, Dini C, Fazzuoli M, Pandeli E, Principi G (2001) Carta geologica dell'Elba Centrale e orientale; Consiglio Nazionale delle Ricerche. DB MAP, Firenze.

Bakker RJ (2003) Fluid package of computer programs for fluid inclusion studies, fluids.unileoben.ac.at

Berman RG (1990) Mixing Properties of Ca-Mg-Mn Garnets. *American Mineralogist* 75:328–344.

Bertini G, Cameli GM, Constantini FA, Decandia FA, Dini I, Elter FM, Lazzarotto A, Liotta D, Pandeli E, Sandrelli F (1994) Structural features of Southern Tuscany along the Monti di Campiglia-Rapolano Terme cross-section. *Memoire della Societa Geologica Italiana* 48:51–59.

Boccaletti M, Gianelli G, Sani F (1997) Tectonic regime, granite emplacement and crustal structure in the inner zone of the Northern Apennines (Tuscany, Italy): A new hypothesis. *Tectonophysics* 270(1-2):127–143.

Bortolotti V, Fazzuoli M, Pandeli E, Principi G, Babbini A, Corti S (2001) Geology of Central and Eastern Elba Island, Italy. *Ofioliti* 26(2a):97–150.

Burke, E. A. J. (2001) Raman microspectrometry of fluid inclusions. Fluid Inclusions: Phase Relationships - Methods - Applications. A Special Issue in honour of Jacques Touret 55(1–4):139–158.

Carmignani L, Kligfield R (1990) Crustal extension in the northern Apennines: The transition from compression to extension in the Alpi Apuane Core Complex. *Tectonics* 9(6):1275–1303.

Černý P (1991) Fertile granites of Precambrian rare-element pegmatite fields: is geochemistry controlled by tectonic setting or source lithologies? *Precambrian Research* 51(1-4):429–468.

Černý P, Ercit TS (2005) The classification of granitic pegmatites revisited. *The Canadian Mineralogist* 43(6):2005–2026.

Conticelli S, Bortolotti V, Principi G, Laurenzi MA, Antonio MD, Vaggelli G (2001) Petrology, mineralogy and geochemistry of a mafic dike from Monte Castello, Elba Island, Italy. *Ofioliti* 26:249–262.

Decandia FA, Lazzarotto A, Liotta D (2001) Structural features of Southern Tuscany, Italy. *Ofiolit*i 26(2a):287–300.

Dini A, Innocenti F, Rocchi S, Tonarini S, Westerman DS (2002) The magmatic evolution of the late Miocene laccolith–pluton–dyke granitic complex of Elba Island, Italy. *Geological Magazine* 139(03).

Driesner T, Heinrich CA (2007) The system H2O–NaCl. Part I: Correlation formulae for phase relations in temperature–pressure–composition space from 0 to 1000°C, 0 to 5000bar, and 0 to 1 XNaCl. *Geochimica et Cosmochimica Acta* 71(20):4880–4901.

Ferry JM, Spear FS (1978) Experimental calibration of the partitioning of Fe and Mg between biotite and garnet. *Contributions to mineralogy and petrology* 66(2):113–117.

Frisch W, Meschede M (2011) Plattentektonik. Kontinentverschiebung und Gebirgsbildung, 4., durchgesehene und aktualisierte Auflage *Wissenschaftliche Buchgesellschaft*, Darmstadt.

Frisch W, Meschede M, Kuhlemann J (2008) Elba. Geologie, Struktur, Exkursionen und Natur. Sammlung geologischer Führer, Bd. 98. *Borntraeger*, Berlin.

Gulbin YL (2011a) Optimization of the garnet-biotite geothermometer: I. Temperature trends. *Geology of Ore Deposits* 53(7):528–542.

Gulbin YL (2011b) Optimization of the garnet-biotite geothermometer: Part II. Calibration equations and accuracy of the estimation. *Geology of Ore Deposits* 53(7):543–557.

Hawthorne FC, Henry DJ (1999) Classification of the minerals of the tourmaline group. *European Journal of Mineralogy* 11(2):201–215.

Henry DJ, Guidotti CV (1985) Tourmaline as a petrogenetic indicator mineral: an example from staurolite-grade metapelites of NW Maine. *American Mineralogist* 70(1-2):1–15.

Henry DJ, Novak M, Hawthorne FC, Ertl A, Dutrow BL, Uher P, Pezzotta F (2011) Nomenclature of the tourmaline-supergroup minerals. *American Mineralogist* 96(5-6):895–913.

Innocenti F, Westerman DS, Rocchi S, Tonarini S (1997) The Montecristo monzogranite (Northern Tyrrhenian Sea, Italy): a collisional pluton in an extensional setting. *Geological Journal* 32(2):131–151.

Kaneko Y, Miyano T (2004) Recalibration of mutually consistent garnet–biotite and garnet–cordierite geothermometers. *Lithos* 73(3-4):255–269.

Keller J, Minelli G, Pialli G (1994) Anatomy of late orogenic extension: The Northern Apennines case. *Tectonophysics* 238(1-4):275–294.

Lavecchia G (1988) The tyrrhenian-apennines system: structural setting and seismotectogenesis. *Tectonophysics* 147(3-4):263–296.

London D (2008) Pegmatites. Canadian mineralogist: Special publication, vol 10. *Mineralogical Association of Canada.*

Maineri C, Benvenuti M, Costagliola P, Dini A, Lattanzi P, Ruggieri G, Villa I (2003) Sericitic alteration at the La Crocetta deposit (Elba Island, Italy): interplay between magmatism, tectonics and hydrothermal activity. *Mineralium Deposita* 38(1):67–86.

Marinelli G, Trevisan L (1967) Carta geologica dell'Isola d'Elba 1:25 000. E schema tettonico. *E.I.R.A*, Firenze

Minelli G, Keller JV (2003) Chapter 1. The Island of Elba: tectonic setting and geological evolution. *Periodico di Mineralogia* 72:65–72.

Musumeci G, Mazzarini F, Tiepolo M, Di Vincenzo G (2011) U - Pb and ^{40}Ar - ^{39}Ar geochronology of Palaeozoic units in the northern Apennines: determining protolith age and alpine evolution using the Calamita Schist and Ortano Porphyroid. *Geological Journal* 46(4):288–310.

OpenStreetMap (2014) OpenStreetMap.org. CC-BY-SA 2.0. Web. 1 Aug. 2014 <http://www.openstreetmap.org/#map=12/42.7973/10.2832&layers=C>.

Pandeli E, Bartolini C, Dini A, Antolini E (2010) New data on the paleogeography of Southern Tuscany (Italy) since Late Miocene time. *International Journal of Earth Sciences (Geologische Rundschau)* 99(6):1357–1381.

Pandeli E, Santo AP, Morelli M, Orti L (2006) Petrological and geological data of porphyritic dikes from the Capo Arco area (Eastern Elba Island, northern Tyrrhenian Sea). *Periodico di Mineralogia* 75(2-3):241–254.

Pezzotta F (2000) Internal structures, parageneses and classification of the miarolitic (Li-bearing) complex pegmatites of Elba Island (Italy). *In* Mineralogy and Petrology of Shallow Depth Pegmatites (F. Pezzotta, ed.). *Memorie della Società Italiana di Scienze Naturali e del Museo Civico di Storia Naturale di Milano* 30(1):29–43.

Poli G (1992) Geochemistry of Tuscan Archipelago Granitoids, Central Italy: The Role of Hybridization Processes in Their Genesis. *Journal of Geology* 100(1):41–56.

Regione Toscana (2014) Carta geologica. CC-BY-SA. Web. 1 Aug. 2014 <http://www.regione.toscana.it/-/carta-geologica>.

Rocchi S, Dini A, Innocenti F, Tonarini S, Westerman DS (2003) Chapter 2. Elba Island: intrusive magmatism. *Periodico di Mineralogia* 72:73–104.

Ruggieri G, Lattanzi P (1992) Fluid inclusion studies on Mt. Capanne pegmatites, Isola d'Elba, Tuscany, Italy. *European Journal of Mineralogy* 4(5):1085–1096.

Serri G, Innocenti F, Manetti P (1993) Geochemical and petrological evidence of the subduction of delaminated Adriatic continental lithosphere in the genesis of the Neogene-Quaternary magmatism of central Italy. *Tectonophysics* 223(1-2):117–147.

Sowerby JR, Keppler H (2002) The effect of fluorine, boron and excess sodium on the critical curve in the albite–H2O system. *Contributions to mineralogy and petrology* 143(1):32–37.

Trevisan L (1950) L'Elba orientale e la sua tettonica di scivolamento per gravità. *Memorie dell'Istituto Geologico dell'Università di Padova* 16:1–30.

Westerman DS, Dini A, Innocenti F, Rocchi S (2004) Rise and fall of a nested Christmas-tree laccolith complex, Elba Island, Italy. *Geological Society, London, Special Publications* 234(1):195–213.

9. Appendix

Tab. A 1: Overview of all studied localities, country rocks, samples and preparation

Nr.	GPS North	GPS East	locality	country rock	samples	thin section	thick section
456	42°44'48.3"	10°12'31.7"	quarry near San Piero in Campo	monzogranite	8	no	no
457	42°44'54.4"	10°12'35.1"	in front of the quarry	metasediment	3	yes	no
458	42°44'46.3"	10°12'35.5"	along the road to San Piero	metasediment	0	no	no
459	42°44'47.2"	10°12'41.6"	along the road to San Piero	metasediment	3	yes	yes
460	42°44'46.5"	10°12'44.4"	along the road to San Piero	metasediment	2	yes	no
461	42°44'57.9"	10°12'48.3"	along the road to San Piero	serpentinite monzogranite	0	no	no
462	42°44'53.0"	10°12'46.9"	above the road to San Piero	metasediment	1	yes	no
463	42°44'58.4"	10°12'46.1"	above the road to San Piero	serpentinite	0	no	no
464	42°45'11.7"	10°12'59.9"	path down to Grotta d'Oggia	monzogranite	1	yes	no
465	42°45'20.8"	10°12'55.2"	Grotta d'Oggia	monzogranite	6	yes	no
466	42°45'18.1"	10°12'55.3"	path back to the road	serpentinite	2	no	no
467	42°45'15.4"	10°12'58.6"	path back to the road	metasediment	5	yes	yes
468	42°46'45.3"	10°13'14.4"	near Pietra Acuta	monzogranite	1	no	no
469	42°46'40.8"	10°13'08.1"	along road near Pietra Acuta	monzogranite	0	no	no
470	42°46'51.6"	10°12'57.5"	next to hiking trail 18 near P. Acuta	monzogranite	2	no	no
471	42°46'09.5"	10°13'43.9"	La Pila, path to Gorgolinato	metasediment	1	no	no
472	42°46'14.6"	10°13'36.8"	above La Pila, Catri	serpentinite	3	yes	no
473	42°46'16.8"	10°13'34.1"	near Catri	serpentinite	0	no	no
474	42°46'17.2"	10°13'32.3"	near Catri	monzogranite	0	no	no
475	42°46'18.5"	10°13'30.2"	near Catri	monzogranite	5	yes	no
476	42°46'20.4"	10°13'26.7"	near Catri	monzogranite	1	no	no
477	42°46'19.7"	10°13'21.3"	near Catri	monzogranite	1	no	no
479	42°46'12.2"	10°13'16.5"	near Catri	monzogranite	0	no	no
480	42°46'09.4"	10°13'18.5"	near Catri	monzogranite	0	no	no
481	42°46'08.7"	10°13'19.6"	near Catri	monzogranite	0	no	no
482	42°46'06.9"	10°13'22.8"	near Catri	serpentinite	0	no	no
483	42°46'06.6"	10°13'24.4"	near Catri	serpentinite	2	no	no
484	42°46'04.9"	10°13'25.4"	near Catri	serpentinite	1	no	no
485	42°46'04.2"	10°13'25.9"	near Catri	serpentinite	1	yes	yes
486	42°46'05.4"	10°13'27.5"	near Catri, magnesite dome	magnesite	0	no	no
487	42°46'03.6"	10°13'26.9"	near Catri, below magnesite dome	monzogranite	0	no	no
488	42°46'03.0"	10°13'27.9"	near Catri, below magnesite dome	metasediment	0	no	no
489	42°46'02.4"	10°13'28.4"	near Catri	serpentinite	0	no	no

Nr.	GPS North	GPS East	locality	country rock	samples	thin section	thick section
490	42°46'01.6"	10°13'29.6"	near Catri	serpentinite	1	no	no
491	42°46'00.3"	10°13'30.9"	near Catri, downwards	serpentinite	0	no	no
493	42°45'47.9"	10°13'25.8"	along the road to San Illario	serpentinite	2	no	no
494	42°45'48.9"	10°13'15.9"	above the road to San Illario	serpentinite	2	no	no
496	42°45'42.2"	10°13'22.2"	along the road to San Illario	serpentinite	1	no	no
497	42°45'44.9"	10°13'24.3"	along the road to San Illario	serpentinite	1	no	no
498	42°45'46.0"	10°13'24.7"	along the road to San Illario	serpentinite	2	no	no
500	42°45'45.9"	10°13'25.6"	along the road to San Illario	serpentinite	1	yes	yes
501	42°47'20.3"	10°14'04.6"	Spiaggia Spartaia, near Procchio	lime silicate	11	yes	yes
502	42°47'19.8"	10°14'16.9"	Spiaggia Spartaia, near Procchio	lime silicate	1	no	no
503	42°47'19.5"	10°14'08.3"	Spiaggia Spartaia, near Procchio	lime silicate	2	yes	no
504	42°47'19.0"	10°13'51.4"	Spiaggia Pauline (Paolina)	radiolarite	1	no	no
505	42°47'18.9"	10°13'52.6"	Spiaggia Pauline (Paolina)	radiolarite	2	yes	no
506	42°47'18.1"	10°13'52.7"	Spiaggia Pauline (Paolina)	radiolarite	1	no	no
507	42°44'41.0"	10°07'19.7"	south of Pomonte, westcoast	metasediment	8	no	no
508	42°44'40.7"	10°07'20.0"	south of Pomonte, westcoast	metasediment	3	no	no
509	42°44'40.3"	10°07'20.2"	south of Pomonte, westcoast	metasediment	3	yes	no
510	42°44'43.6"	10°07'11.1"	at beach south of Pomonte	serpentinite	2	no	no
511	42°44'44.1"	10°07'12.0"	at beach south of Pomonte	Fe skarn	0	no	no
512	42°46'00.4"	10°06'20.8"	north of Chiessi, westcoast	serpentinite	1	no	no
513	42°45'54.1"	10°06'23.5"	north of Chiessi, westcoast	metasediment	5	no	no
514	42°45'52.8"	10°06'23.6"	north of Chiessi, westcoast	granite	0	no	no
515	42°46'23.8"	10°06'18.2"	north of Chiessi, downwards	serpentinite	1	yes	yes
516	42°46'07.3"	10°24'23.8"	Spiaggia Barbarossa (Porto Azzurro)	calamita schist and granite	5	no	no
517	42°46'09.5"	10°24'31.8"	Spiaggia Barbarossa (Porto Azzurro)	calamita schist	1	yes	yes
518	42°46'13.8"	10°24'55.8"	Spiaggia Reale	calamita schist	1	no	no
519	42°46'16.6"	10°24'59.2"	Spiaggia Reale	calamita schist	2	no	no
520	42°46'22.5"	10°25'07.7"	beach near Lake Terranera	Zuccale fault	2	no	no
521	42°45'12.8"	10°24'23.3"	beach Naregno, Calamita	calamita schist	1	no	no
522	42°45'24.6"	10°24'08.0"	beach Naregno, Calamita	calamita schist	5	no	no

Nr.	GPS North	GPS East	locality	country rock	samples	thin section	thick section
523	42°44'45.5"	10°24'29.1"	beach Ferrato, Calamita	calamita schist	6	yes	no
524	42°44'37.1"	10°24'52.6"	Spiaggio di Istia, Calamita	calamita schist	4	no	no
525	42°44'33.4"	10°25'11.9"	next beach after Istia, Calamita	calamita schist	7	yes	yes
527	42°44'18.6"	10°25'34.6"	Miniera Sassi Neri, Calamita	calamita schist, Fe skarn	1	no	no
528	42°43'50.5"	10°25'55.0"	beach Stagnano, Calamita	calamita schist	7	no	no
529	42°43'48.8"	10°25'52.9"	beach Stagnano, Calamita	calamita schist	4	yes	no
531	42°43'30.9"	10°26'03.6"	Ginepro; P.ta Bianco, Calamita	calamita schist	6	no	no
532	42°43'29.7"	10°26'01.0"	Ginepro; near P.ta Bianco, Calamita	calamita schist	2	no	no
533	42°43'25.5"	10°26'01.0"	Ginepro; near P.ta Bianco, Calamita	calamita schist	0	no	no
534	42°43'23.3"	10°26'02.5"	Ginepro; near P.ta Bianco, Calamita	calamita schist	0	no	no
535	42°43'12.7"	10°26'06.8"	Ginepro; near mine, Calamita	calamita schist, Fe skarn	1	yes	yes
536	42°43'38.9"	10°23'13.8"	road back to Capoliveri, Calamita	calamita schist	4	no	no
537	42°43'56.2"	10°22'17.5"	Spiaggio Marcone, Calamita	calamita schist	0	no	no

Tab. A 2: Description and dip / dip direction of all studied dykes

Number	country rock	what?	dip direction	dip	thickness [cm]	petrographical description
456	monzogranite	dyke	260	57		symmetric, fine-grained tourmaline in centre
		tourmaline needles	215	85		
		country rock	278	70		mafic xenoliths, abundance of tourmaline
		country rock	262	75		large (5-10cm) K-feldspar crystals
457	metasediment	dyke	E-W strike			tourmaline "suns", abundance of garnet and mica
						abundant of quartz, K-feldspar
458	metasediment	country rock				large (5-10cm) K-feldspar crystals
459	metasediment	dyke	N-S strike		4 - 100	abundance of mica and garnet, tourmaline
						recrystallized quartz, K-feldspar
460	metasediment	dyke	N-S strike		20	tourmaline, and zoned or columnar pinnk andalusite
						recrystallized quartz, big K-feldspar, mica
461	serpentinite	country rock				greenish, fine-grained, abundance of garnet
	monzogranite	country rock				weathered; large (5-10cm) K-fsp crystals, "leucogranite"
		dyke	275	78	0,5	fine-grained dyke
462	metasediment	mafic sample				exsolutions of quartz, fsp; green spinel (hercynite)
463	serpentinite	country rock				weathered; abundance of nodular magnesite, eroded
464	monzogranite	dyke				little quartz; K-fsp; fractured tourmaline and pink andalusite
465	monzogranite	dyke 2nd generation	100	60		
		dyke 2nd generation	95	65		coarse-grained tourmaline
		dyke	122	40		symmetrical zoned; coarse quartz, tourmaline; fsp; biotite
466	serpentinite	country rock				nodular magnesite, eroded
467	metasediment	dyke	70	70		abundant coarse quartz (fluid inclusions), K-fsp, andalusite
468	monzogranite	dyke	N-S strike		5 - 10	country rock is highly weathered, no large K-fsp crystals
469	monzogranite	dyke	NE-SW strike		1 - 10	country rock is highly weathered, no large K-fsp crystals
470	monzogranite	dyke	N-S strike		20	dyke with coarse-grained tourmaline
471	metasediment	dyke	N-S strike			quite coarse sample
472	serpentinite	dyke	N-S strike	53	20 - 50	irregular dyke; weathered; recrystallized quartz, Fsp; sillimanite
						zoned tourmaline, pink andalusite, coarse cordierite; xenotime
473	serpentinite	dyke	N-S strike		5	highly weathered pegmatite
474	monzogranite	country rock				transition zone of serpentinite / granite country rock
475	monzogranite	dyke	NE-SW strike		50	zoned; coarse fsp, tourmaline; faint biotite; polycrystalline qtz
476	monzogranite	dyke	300	45	10	brownish dyke filled with tourmaline
477	monzogranite	dyke	320	50	5	country rock is highly weathered

Number	country rock	what?	dip direction	dip	thickness [cm]	petrographical description
		dyke	356	30	10	brownish dyke without tourmaline
480	monzogranite	country rock				no more large k-fsp crystals in the country rock
481	monzogranite	dyke			12	zoned dyke (coarse-fine-coarse)
482	serpentinite	country rock				transition zone of granite / serpentinite country rock
483	serpentinite	dyke				abundance of coarse-grained tourmaline
484	serpentinite	dyke	150	70	200	zoned dyke (coarse-fine-coarse; more-less tourmaline)
485	serpentinite	dyke			0,5	eroded magnesite; sample with coarse qtz, tourmaline, albite
486	magnesite	country rock				eroded magnesite and nodular magnesite
487	monzogranite	country rock				transition zone of magnesite / granite (no big K-fsp) country rock
488	metasediment	country rock				transition zone of granite / metasediment country rock
489	serpentinite	country rock				transition zone of metasediment / serpentinite country rock
490	serpentinite	dyke				big pegmatitic dyke, abundance of tourmaline
491	serpentinite	dyke	310	65	200	big dyke; 20m downwards pegmatitic dykes within granite
493	serpentinite	dyke	E-W strike		30	dyke with a different texture
494	serpentinite	dyke			40 - 80	irregular dyke; weathered
496	serpentinite	dyke			40	abundance of coarse-grained tourmaline
497	serpentinite	dyke				abundance of coarse-grained tourmaline (schorl)
498	serpentinite	dyke	NE-SW strike		10	fine-grained tourmaline; brownish fine-grained (mm) crystals
500	serpentinite	dyke				zoned dyke; fine- and coarse-grained qtz, fsp and tourmaline
501	lime silicate	dyke			100	big aplitic dyke with heaps of quartz-/tourmaline rich veins
		dyke	315	15	100	aplitic dyke, above marble and lime silicate
		country rock				metamorphic lime with vesuvianite (red), calcite, diopside
		dyke	270	50	25	many inclusions (and needles) in qtz; red andalusite; fsp
502	lime silicate	dyke	270	80	30 - 50	irregular dyke; highly weathered
		joint	350	80		joint system in marble, very steep
503	lime silicate	dyke	270	80	200 - 300	weathered, but zoned (fine-coarse-fine); qtz, fsp, tourmaline
		dyke	275	80	10 - 20	weathered
504	radiolarite	dyke	215	80		large aplitic dyke with heaps of quartz-/tourmaline rich veins
		dyke	315	78	5 - 10	quartz-/tourmaline rich vein, most of them are parallel
		dyke 2nd generation	188	70	3	symmetric; columnar tourmaline at the margin
		dyke 2nd generation	138	80	10	coarse-grained crystals and muscovite
505	radiolarite	dyke	195	68		symmetric zoned; coarse-grained qtz, fsp, tourmaline; muscovite
		dyke 3rd generation	90	80	10	asymmetric; no columnar tourmaline at the margin

Number	country rock	what?	dip direction	dip	thickness [cm]	petrographical description
507	metasediment	dyke	5	45	10 - 20	pegmatitic dyke, weathered and folded
		dyke	5	80	10 - 20	pegmatitic dyke, weathered and folded
		dyke 2nd generation	154	25	10	tourmaline rich vein
		dyke	345	75		irregular dyke; weathered
508	metasediment	dyke 2nd generation	120	40	20 - 30	zoned (fine-coarse; more-less tourmaline)
		dyke	305	15	5	symmetric; columnar tourmaline at the margin; muscovite
		dyke				thin dyke with pink andalusite
509	metasediment	dyke	105	70	5	thin dyke with pink andalusite and muscovite
		dyke				thin dyke with qtz, fsp; fractured tourmaline, sillimanite
510	serpentinite	dyke	318	45	30	zoned dyke; fine-coarsed at the rim; coarse at the centre
511	Fe skarn	skarn	N-S strike		40	skarn with hedenbergite, large crystals of epidote
512	serpentinite	dyke	N-S strike		2000	aplitic, steep dyke; abundance of fsp
513	metasediment	dyke	N-S strike		800	aplitic, steep dyke; bright in centre; much biotite, qtz at the rim
514	granite	dyke			2500	many thick parallel pegmatitic dykes with tourmaline/qtz
515	serpentinite	dyke			100	grey, weathered; Qtz-matrix with fsp, biotite, partly chloritisized
516	calamita schist	dyke			300	many aplitic; some pegmatitic dykes
	and granite	tourmaline dyke			100 - 200	black, pure tourmaline; near fault zone
		tourmaline needles	300	50	0,5	with reaction rims; they often go through dykes/mafic inclusions
517	calamita schist	dyke	295	35		aplitic; near faultzone; abundance of fsp; exsolution/transform.
		fault	175	35		fault zone dislocates some dykes, underneath more trm dykes
518	calamita schist	dyke	275	75	10 - 50	aplitic; fine- /straightened tourmaline and weathered minerals
		fault	340	15		near fault zone slight deformation, straightening, thinning
		joint	40	40		
519	calamita schist	dyke				pegmatitic; zoned (fine-coarse); stratification noticeable
		fault	60	65		several fault zones with dislocation, thinning, transf. near them
520	Zuccale fault	dyke				coarse-grained tourmaline and "suns" like Capo Bianco aplite
521	calamita schist	dyke			1 - 5	pegmatitic; zoned (fine-coarse); due to faults often dislocation
		dyke	235	67		irregular dyke due to fault zones
522	calamita schist	dyke			1 - 10	pegmatitic; zoned (fine-coarse; more-less trm); muscovite
523	calamita schist	dyke	280	40	5	pegmatitic; weathered qtz, fsp; fractured trm; pink andalusite
524	calamita schist	dyke	330	20		pegmatitic; zoned (red andalusite in lower parts); schorl
		tourmaline dyke	80	85		pure tourmaline veins; going through other dykes
525	calamita schist	dyke			40 - 150	pegmatitic; zoned (fine-coarse trm/qtz), coarse pink andalusite

Number	country rock	what?	dip direction	dip	thickness [cm]	petrographical description
		dyke 3rd generation			5 - 10	deeper than the pegmatitic dykes; intruded into fractures
		dyke 2nd generation	315	18	20 - 30	symmetrical (coarse-grained at margin); formed due to escape
		tourmaline dyke	275	85		last phase; highly altered; pure tourmaline vein
527	calamita schist	tourmaline dyke	235	85		intruded into fractures in skarn; but no alteration/mineralisat.
	Fe skarn	dyke				pegmatitic; with tourmaline; folded
528	calamita schist	dyke	75	70	30 - 50	pegmatitic; very steep; zoned (fine-coarse trm), pink andalusite
		tourmaline dyke	195	20	0,5 - 1	now shallow; perpendicular to folded calamita schist
		quartz vein	328	85	0,1 - 0,5	perpendicular to the tourmaline dykes
		dyke	55	55	20	very coarse qtz; pegmatitic in centre; tourmaline "suns"
		dyke			10 - 20	massive trm at the margin; coarse qtz in centre; green mineral
529	calamita schist	dyke	55	85	200	zoned (fine-coarse; more-less tourmaline); pink andalusite
		dyke			10	symmetrical (coarse qtz in centre pegmatitic at the margin)
		brownish vein			0,1 - 0,5	brownish matrix (pure tourmaline) with fragments
531	calamita schist	dyke	235	60	500	all types of zoning and flow textures (transform.), pink andalus.
		flow structure in dyke	240	35	50	coarse-grained at rim; with lenses/pods; turning to single vein
		dyke 2nd generation	250	15	10	many parallel, zoned (all types) dykes; even tourmaline "suns"
532	calamita schist	dyke	225	25	200	pegmatitic; zoned (coarse/fine qtz; pink andalusite); muscovite
		dyke	190	55	50	zoned (coarse/fine tourmaline); straightened crystals
533	calamita schist	dyke 2nd generation	145	25		pegmatitic; zoned (coarse/fine); pink andalusite
		brownish vein	105	35	0,1 - 0,5	brownish matrix (pure tourmaline) with fragments
		tourmaline dyke	105	50	1 - 5	many parallel dykes; due to network of shear movement?
		tourmaline dyke	105	85	5	steep; many parallel dykes; due to network of shear movement?
534	calamita schist	dyke	125	25	1 - 50	pegmatitic; zoned (coarse/fine qtz; pink andalusite)
535	calamita schist	dyke				near mineralisation, deformation; qtz, fsp, trm, andal., garnet
	Fe skarn	skarn				skarn with hedenbergite, epidote, magnetite, ...
536	calamita schist	dyke	230	25	10	many parallel, aplitic dykes; fine-coarsed tourmaline
		dyke	115	85	5	few pegmatitic, steep dykes
		dyke			20 - 100	shallow, thick dykes; near fault zone; qtz + fragments; brownish
		fault	60	40		fault zone dislocates some dykes
537	calamita schist	dyke			1 - 5	few aplitic and pegmatitic dykes
		tourmaline dyke	234	80	0,5 - 2	black, pure tourmaline; sometimes together with quartz

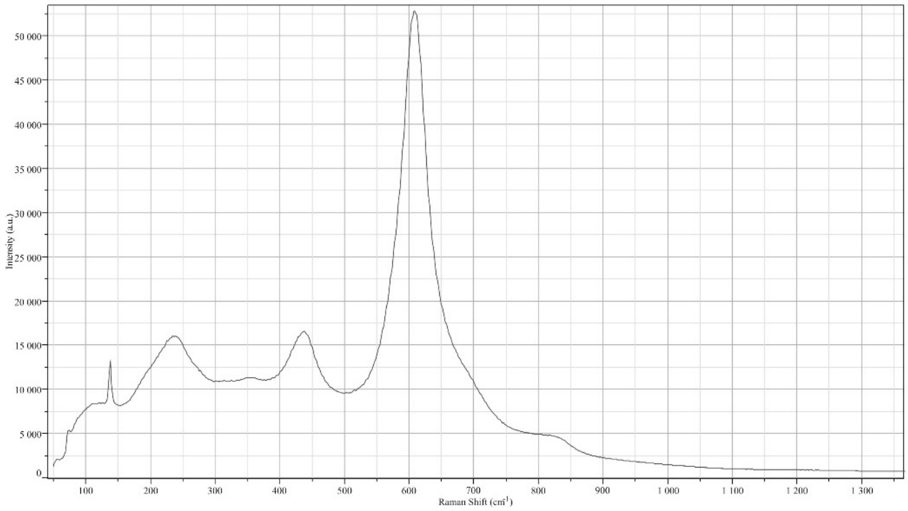

Fig. A 1: Raman spectrum of rutile, found in sample 57A

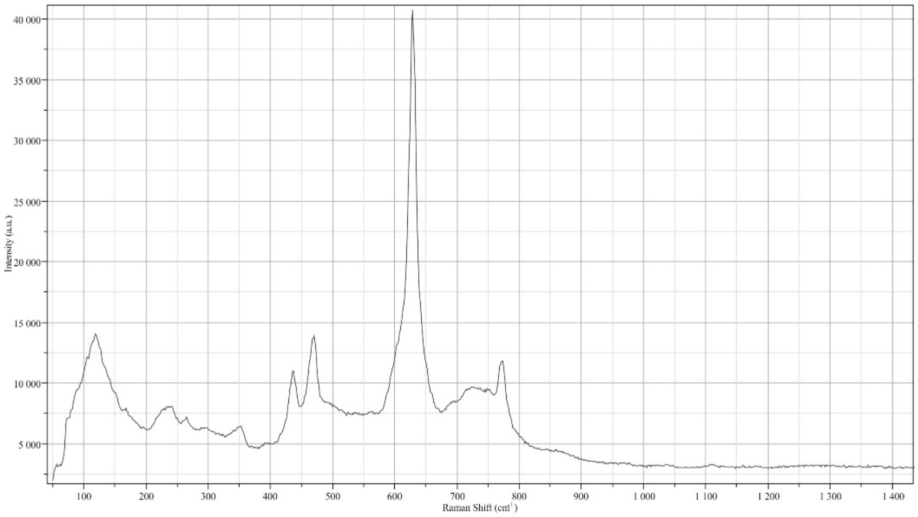

Fig. A 2: Raman spectrum of cassiterite, found in sample 59B

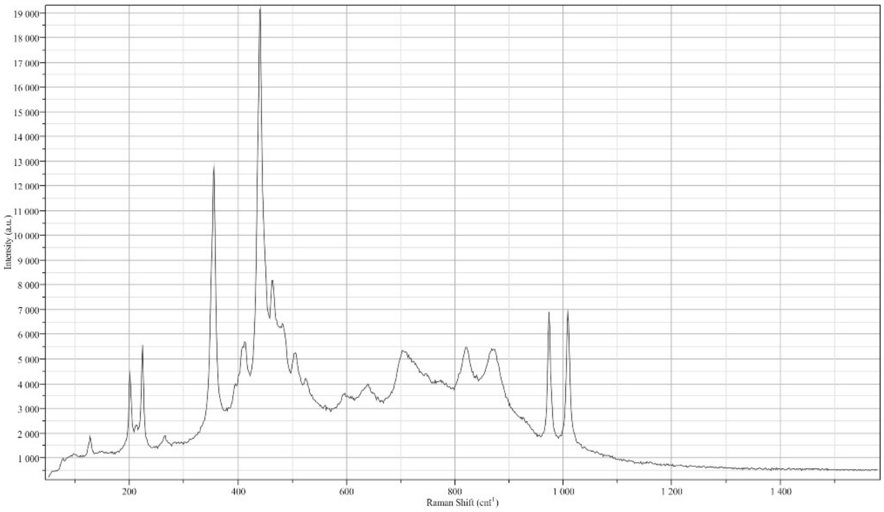

Fig. A 3: Raman spectrum of zircon, found in sample 67E

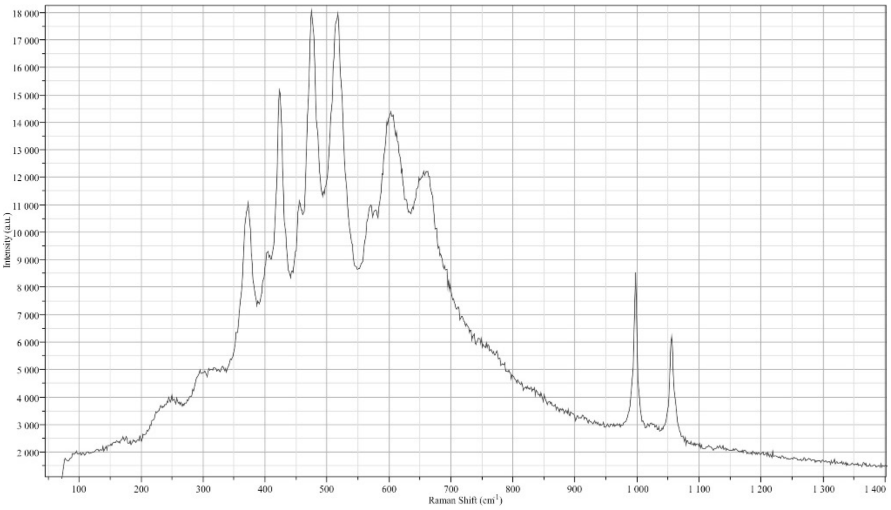

Fig. A 4: Raman spectrum of xenotime, found in sample 72C

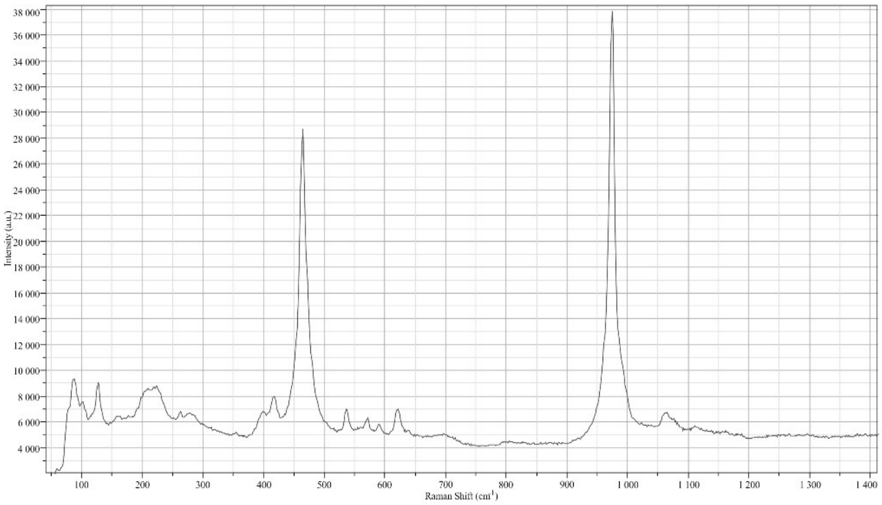

Fig. A 5: Raman spectrum of monazite-(Ce), found in sample 0A

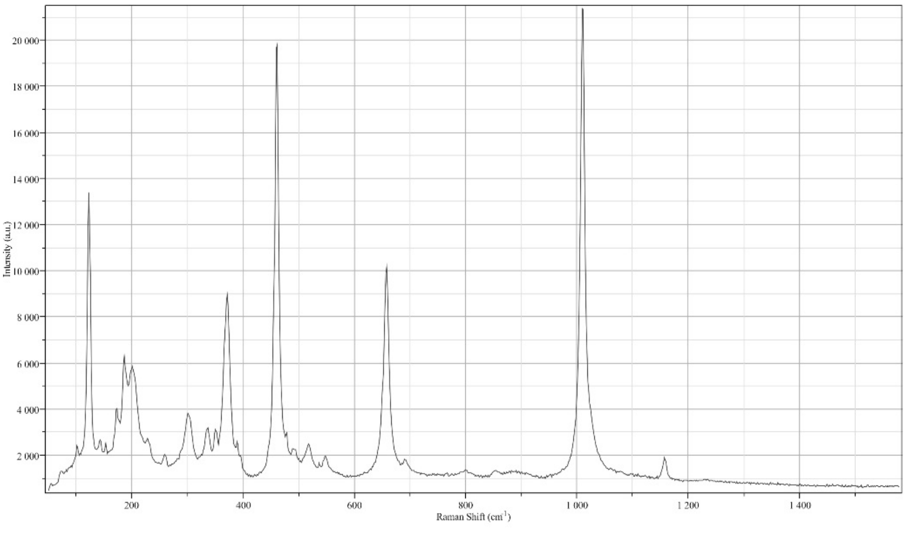

Fig. A 6: Raman spectrum of hedenbergite, found in sample 1J

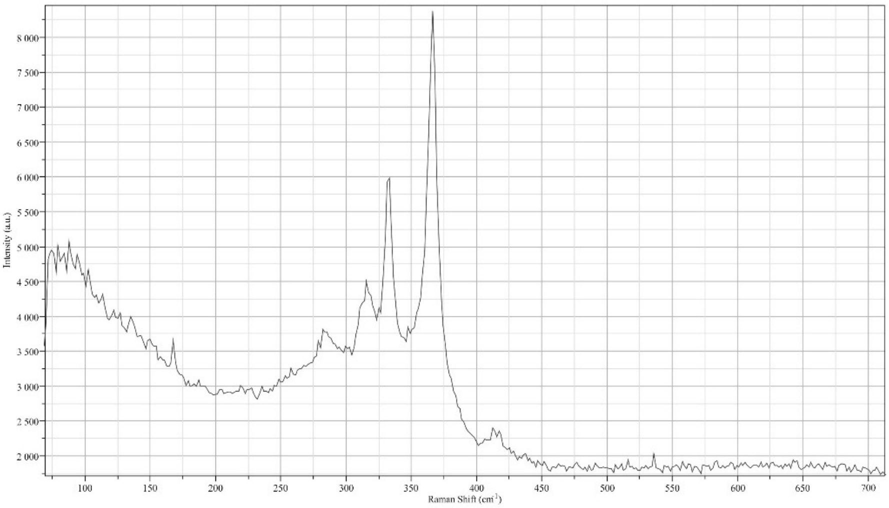

Fig. A 7: Raman spectrum of smithite, found in sample 1J

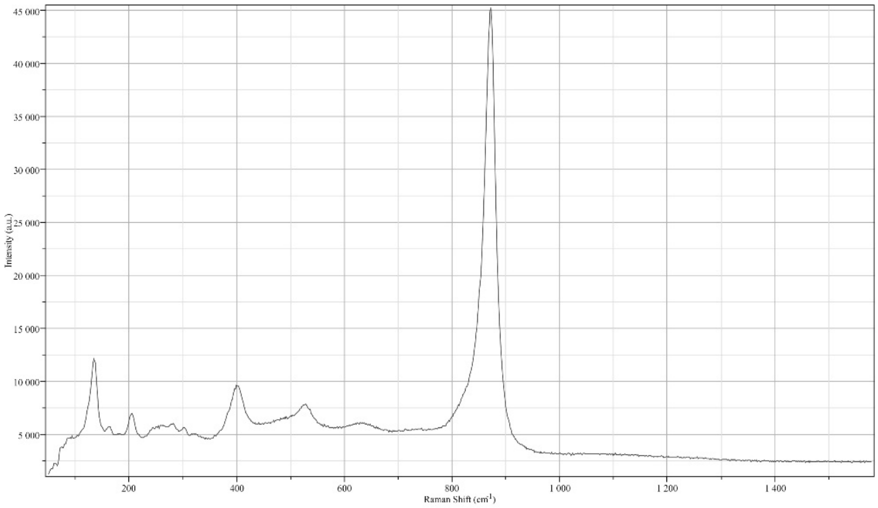

Fig. A 8: Raman spectrum of columbite-(Fe), found in sample 3A

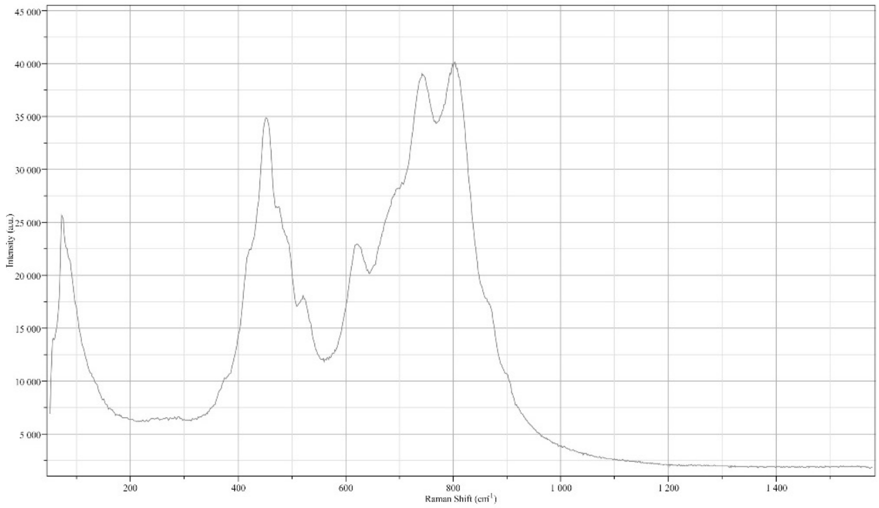

Fig. A 9: Raman spectrum of columbite-(Mn), found in sample 3A

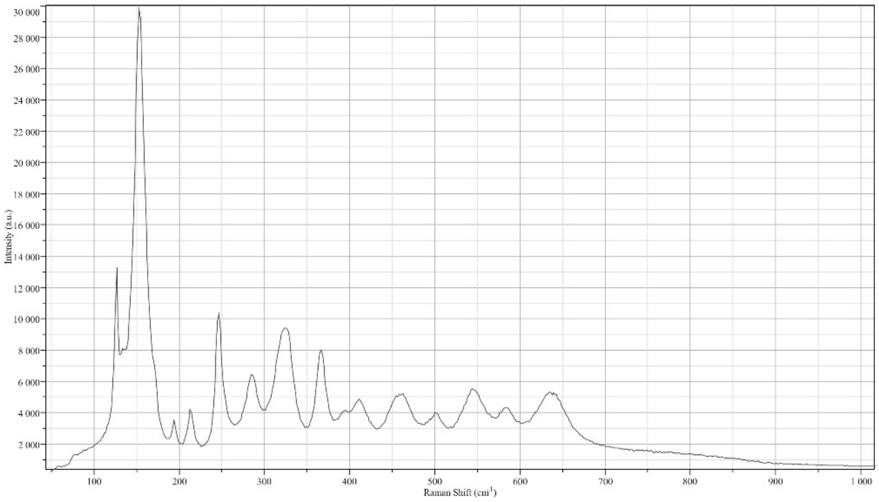

Fig. A 10: Raman spectrum of brookite, found in sample 15A

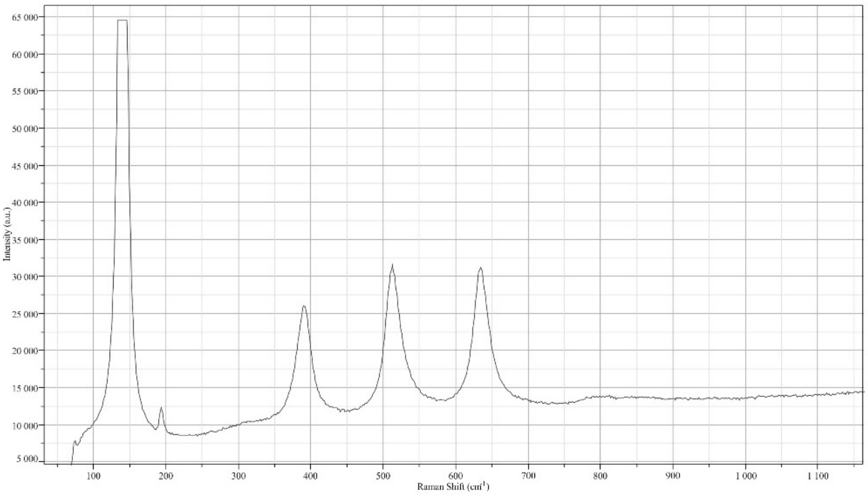

Fig. A 11: Raman spectrum of anatase, found in sample 25A

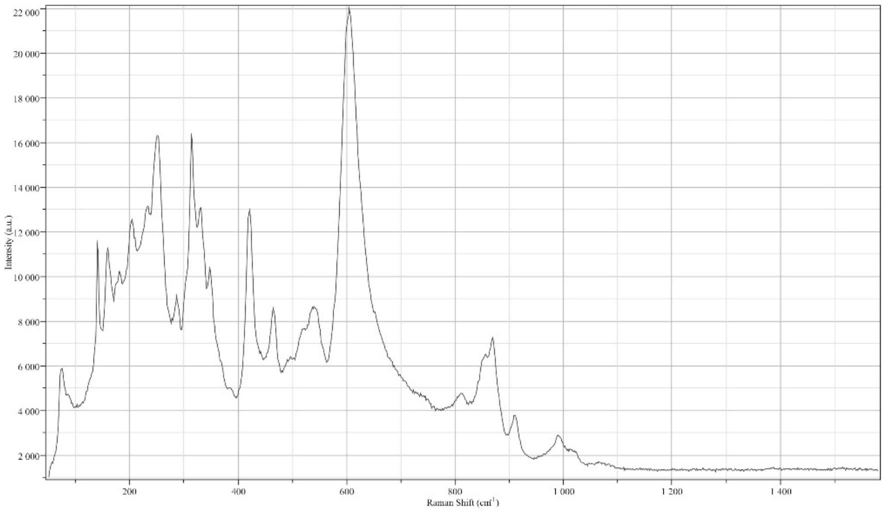

Fig. A 12: Raman spectrum of titanite, found in sample 29D

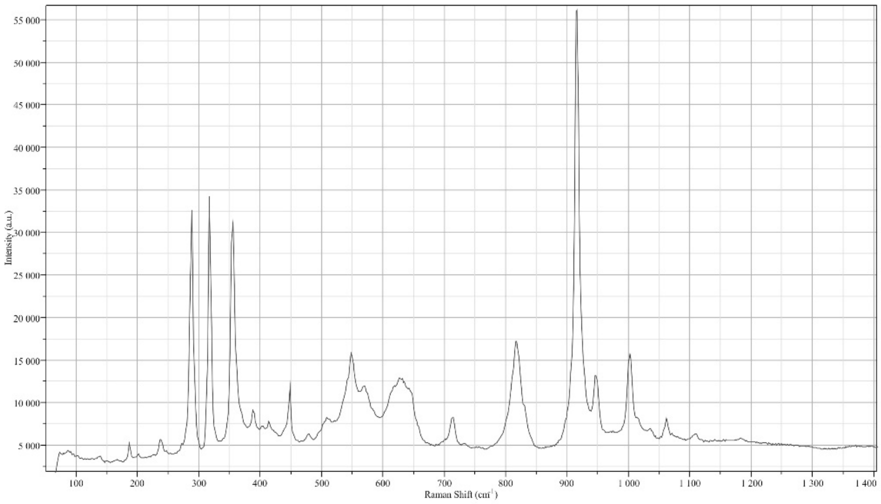

Fig. A 13: Raman spectrum of andalusite, found in sample 35B

Tab. A 3: Microthermometry and Raman results of sample 67E-QTZ3 (T_n= nucleation temperature; T_m= melting temperature; T_h= homogenization temperature; (x)= minor amounts; Cld= cloud)

Nr.	Typ	T_n1	T_n2	T_m1	T_m2	T_h	[°C]	Borate	H_2	N_2	CO_2	CH_4	Clathrate
F1	1	-29,1	-38	-6,9	5,5	365,5	20	x	x	x	x	x	
							-150	x	x	x	x		x
							-20	x	x	x	x		x
							0	x	x	x	x		x
F5	1	-37	-46	-6,9	6,6	365,2	20			(x)	x	x	
							-20				x		x
F7	1	-29	-38	-6	7,5	381,3	20	x	(x)	(x)	x	x	
							-32	x	(x)		x		x
							-100	x	(x)		x		x
							-50	x	(x)		x		x
							-20	x	(x)		x		x
							-10	x	(x)		x		x
							0	x	(x)		x		x
							10	x	(x)		x	x	
F6	1	-29	-39	-6,2		377,2	20		x	(x)	x	x	
F3	1	-31,5		1,4		370,8	20		(x)		x	x	
F4	1	-28	-39	-6,5	6,6	371,9	20	x	x	x	x	x	
F8	1	-29	-40	-6,2	6,1	378,2	20		x	(x)	x	x	
F9	1	-28	-38	-7,2	6,8	370,9	20		x	x	x	x	
F18	1	-29,5		-1		281,2							
F19	1	-31	-36	-3,7	11,3	323,7	20	x	x	x	x	x	
F21	1	-33		-2,4		352,3	20		x	(x)	x	x	
F22	1	-32		-1,4	5,5	367,7							
F23	1	-31,9	0,42	-2,4	7,2	313,6	20		x	x		x	

Nr.	Typ	T_n1	T_n2	T_m1	T_m2	T_h	[°C]	Borate	H_2	N_2	CO_2	CH_4	Clathrate
F29	1	-35		-5,6	-0,8	282							
F34	1	-30	-41	-7,6	5,7	363,4	20		x	(x)	x	x	
F35	1	-36		-4	6	372,8							
F37	1	-30	-39	-7,7	7,3	365,7	20		x	x	x	x	
F38	1	-27	-37	-7,2	6,6	369,6							
F41	1	-26,5	-37	-5,7	6,5	366,8							
F43	1	-31	-39	-5,4	6,6	366,1	20		x		x	x	
F44	1	-34	-39	-6,9	5,5	376,7							
F45	1	-32	-46	-4	3,7	317							
F2	3	-30,4		-0,5		207,7	20		(x)			(x)	
							-100		(x)			(x)	
							-20		(x)			(x)	
							0		(x)			(x)	
							20		(x)			(x)	
F10	3	-41		-1		271,2	20		x			x	
F11	3	-28		-0,8		288,8							
F12	3			-0,7		316,7	20		x			x	
F15	3	-40		-0,6		242,9	20		x			x	
F20	3	-26		-1		277,7							
F24	3	-29		-0,1		232							
F25	3	-29		1			20					x	
F28	3	-38,5		-0,9		291,4							
F31	3	-35		-0,6		234							
F36	3	-38		-0,4		194,8							
F42	3	-37		-0,8		262,7	20		x			x	
F46	3	-40		-0,4		202							
F47	3	-39		0		149,3							
F50	3	-38		-0,2		131,4							
F51	3	-39		-0,4		184,5							
F52	3	-35		-2,6		313,3							
F53	3	-36,8		-0,7		277,2							
F54	3	-35		-0,4		201							
F55	3	-39		0,1		146,8							
F56	3	-37		-0,8		142,7							
F57	3	-36		-0,3		151,4	20		x			x	
F58	3	-37		-0,6		214,6	20		x			(x)	
F60	3	-39		-0,5		212,2							
F61	3	-39		-1,8									
F62	3	-40		-0,7		232,5	20		x			x	
F63	3	-39		-0,3		187,6	20		x				
F67	3						20		x	(x)		x	
F68	3					200,4							
F69	3					189,5							
F70	3					196,3							
F71	3					219							

Nr.	Typ	T_n1	T_n2	T_m1	T_m2	T_h	[°C]	Borate	H_2	N_2	CO_2	CH_4	Clathrate
F72	3					187,6							
F73	3					189,6							
F74	3					194							
F75	3					195							
F13	2	-35		4,1		157,8							
F14	2	-37		-0,5		192	20		x			(x)	
F16	2	-30		-0,4		187	20		x			(x)	
F17	2	-32		-0,4		373,6							
F26	2	-31		-0,4		189							
F27	2	-39		-0,3			20		x				
F30	2	-35		-0,9		221							
F32	2	-31		-0,5		232,2							
F33	2	-37		-0,3		188,9							
F39	2	-33		-2,4		358,1	20		x		x	x	
F40	2	-35		-0,3		239,1							
F48	2	-34		-0,5		247,3							
F49	2	-40		-0,2		126,8							
F59	2	-31		-0,4		197							
F64	2	-38		4		389,5	20		x		x	x	
F65	2						20					x	
F66	2						20					x	
Cld 1	4						20	Mica	(x)				
Cld 2	4						20	Mica	x		x	(x)	
Cld 3	4						30	Mica	x		x		

Tab. A 4: Composition of the studied fluid inclusions of sample 67E-QTZ3

Number	$x(H_2)$	$x(N_2)$	$x(CO_2)$	$x(CH_4)$
F1	0,0065	0,0170	0,8894	0,0870
F5	0,0000	0,0237	0,4840	0,4922
F7	0,0153	0,0235	0,6783	0,2829
F6	0,0517	0,0103	0,6780	0,2600
F3	0,0243	0,0000	0,8307	0,1450
F4	0,0461	0,0148	0,8152	0,1239
F8	0,0128	0,0101	0,8256	0,1516
F9	0,0130	0,0123	0,8316	0,1431
F19	0,0341	0,0211	0,2482	0,6966
F21	0,1175	0,0219	0,1761	0,6845
F23	0,0662	0,0381	0,0000	0,8957
F34	0,0118	0,0229	0,9151	0,0502

Number	$x(H_2)$	$x(N_2)$	$x(CO_2)$	$x(CH_4)$
F37	0,0128	0,0300	0,9128	0,0443
F43	0,0483	0,0000	0,7878	0,1639
F2	0,5844	0,0000	0,0000	0,4156
F10	0,5930	0,0000	0,0000	0,4070
F12	0,8692	0,0000	0,0000	0,1308
F15	0,7939	0,0000	0,0000	0,2061
F42	0,7034	0,0000	0,0000	0,2966
F57	0,7472	0,0000	0,0000	0,2528
F58	0,8932	0,0000	0,0000	0,1068
F62	0,7083	0,0000	0,0000	0,2917
F63	1,0000	0,0000	0,0000	0,0000
F67	0,6622	0,1937	0,0000	0,1441
F14	0,8349	0,0000	0,0000	0,1651
F16	0,8331	0,0000	0,0000	0,1669
F27	1,0000	0,0000	0,0000	0,0000
F39	0,0951	0,0000	0,5315	0,3733
F64	0,0346	0,0000	0,7964	0,1690
F65	0,0000	0,0000	0,0000	1,0000
F66	0,0000	0,0000	0,0000	1,0000
Cloud 1	1,0000	0,0000	0,0000	0,0000
Cloud 2				
Cloud 3				

Tab. A 5: Microthermometry and Raman results of sample 85A-QTZ1 (T_n= nucleation temperature; T_m= melting temperature; T_h= homogenization temperature; (x)= minor amounts)

Nr.	Typ	T_n	T_m	T_h	[°C]	Water	Ice	Borate	Arsenolite	CO_2	CH_4	Clathrate
F1	1	-32,8	-2,6	227,0	20	x			Mica			
F2	1	-36,8	-3,8	220,1	20	x						
F3	1	-38,1	-3,9	239,0	20	x						
F4	1	-37,6	-4,2	238,0	20	x				x		
F5	1	-33,1	-2,7	236,2	20	x					x	
F6	1	-37,2	-4,1	236,3	20	x					(x)	
F7	1	-33,5	-3,4	227,1	20	x						
F8	1	-37,0	-2,5	241,6	20	x		x		x	(x)	
F9	1	-35,5	-4,0	211,7	20	x				x	x	
F10	1	-32,1	-0,6	221,2	20	x					x	
F11	1	-30,9	-2,4	227,7	20	x				x	(x)	
F12	1	-29,0	-0,7	227,5	20	x					x	
F13	1	-34,2	-0,6	191,2								
F14	1	-32,3	-4,4	252,0								
F15	1	-34,9	-3,6	247,2								

Nr.	Typ	T_n	T_m	T_h	[°C]	Water	Ice	Borate	Arsenolite	CO_2	CH_4	Clathrate
F16	1	-34,6	-2,9	235,4	20	x				x		
F17	1	-31,7	-0,4	222,9	20	x					(x)	
F18		-31,7	-0,6									
F19	1	-40,5	-3,9	241,3	20	x				x	x	
					-100		x			x		x
					-50		x			x		x
					-10		x			x		x
					0	x				x	x	
F20	1	-37,7	-4,3	204,3	20	x				x	x	
F21	1	-41,8	-3,2	245,1	20	x				x	(x)	
F22	1	-38,2	-3,4	235,8	20	x				x		
F23	1	-34,0	-3,1	248,0	20	x				x	(x)	
F24	1	-38,0	-3,6	257,3	20	x				x	x	
F25	1	-31,9	-3,7	239,4	20	x				x	x	
F26		-33,5	-3,4									
F27	1	-37,6	-2,7	228,7	20	x				x	x	
F28	1	-38,8	-2,3	228,4	20	x					x	
F29	1	-33,0	-1,5	204,1	20	x				x	x	
F30	1	-32,8	-1,3	232,9	20	x				x		
F31	1				20	x				x		
F32	1				20	x				x	x	
F33	1				20	x						
F34	1				20	x				x	x	
F35	1				20	x		x		(x)		
F36	1				20	x			x	x		

Tab. A 6: Composition of the studied fluid inclusions of sample 85A-QTZ1

Number	$x(CO_2)$	$x(CH_4)$
F4	1,0000	0,0000
F5	0,0000	1,0000
F8	0,9859	0,0141
F9	0,9861	0,0139
F10	0,0000	1,0000
F11	0,9827	0,0173
F12	0,0000	1,0000
F16	1,0000	0,0000
F17	0,0000	1,0000
F19	0,9649	0,0351
F20	0,9619	0,0381
F21	0,9755	0,0245

Number	x(CO_2)	x(CH_4)
F22	0,9724	0,0276
F23	0,9930	0,0070
F24	0,9546	0,0454
F25	0,9737	0,0263
F27	0,8502	0,1498
F28	0,0000	1,0000
F29	0,9006	0,0994
F30	1,0000	0,0000
F31	1,0000	0,0000
F32	0,9486	0,0514

Tab. A 7: Microthermometry and Raman results of sample 85A-QTZ2 (T_n= nucleation temperature; T_m= melting temperature; T_h= homogenization temperature; (x)= minor amounts)

Nr.	Type	T_n	T_m	T_h	[°C]	Water	Ice	Borate	CO_2	CH_4	Chlathrate
F1	1	-31,9	-2,8	243,6	20	x			x	x	
					-130		x				x
					-30		x				x
					-10		x				x
					0	x				x	
F2	2	-32,8	-2,7	245,1	20	x		x			
F3	1	-31,9	-2,8	201,4	20	x			x	x	
F4	1	-32,9	-2,9	239,3	20	x			x	x	
F5	1	-32,4	-2,7	239,6	20	x			x	x	
F6	1	-33,9	-3,1	247,2	20	x			x	x	
F7	1	-32,4	-2,9	238,3	20	x			x	x	
F8	1	-32,5	-2,7	237,5	20	x			x	x	
F9	1	-32,6	-3,0	269,4	20	x			x	x	
F10	1	-32,7	-2,5	245,1	20	x				x	
F11	1				20	x			x	x	
F12	1	-36,4	-3,2	287,8	20	x			x	x	
F13	1	-31,9	-2,7	254,3	20	x			x	x	
F14											
F15											
F16	1	-29,9	-2,6	247,1	20	x			x	x	
F17											
F18	1				20	x			x	x	
F19		-34,5	-4,1								
F20		-34,5	-3,0								
F21	1	-34,3	-3,0	212,8	20	x			x	x	
F22		-34,5	-3,0								

Nr.	Type	T_n	T_m	T_h	[°C]	Water	Ice	Borate	CO_2	CH_4	Chlathrate
F23	2	-33,9	-2,7	198,7	20	x		x			
F24	1	-32,9	-2,8	208,9	20	x			x	x	
F25		-34,6	-3,1								
F26	1	-37,8	-3,0	215,4	20	x			x	x	
F27	1	-33,9	-2,7	207,8	20	x			x	x	
F28	1	-34,5	-2,2	205,7	20	x			x	x	
F29	2	-33,7	-3,1	207,8	20	x		x			
F30	1	-33,8	-3,1	217,4	20	x			x	x	
F31	2	-35,2	-3,2	235,0	20	x		x			
F32	1	-36,6	-3,4	199,0	20	x			x	x	
F33	1	-35,9	-3,3	217,4	20	x			x	x	
F34	1	-31,9	-2,7	235,7							
F35	1	-32,4	-2,7	243,3	20	x			x	x	
F36	1	-32,9	-3,0	241,3							
F37	1	-43,9	-2,8	218,4	20	x			x		
F38	1	-33,9	-2,8	238,7	20	x			x	x	
F39	2	-35,9	-2,5	235,6	20	x		x			
F40	1	-44,9	-2,9	230,2	20	x			x	x	

Tab. A 8: Composition of the studied fluid inclusions of sample 85A-QTZ2

Number	$x(CO_2)$	$x(CH_4)$
F1	0,8850	0,1150
F3	0,8849	0,1151
F4	0,9194	0,0806
F5	0,9115	0,0885
F6	0,9151	0,0849
F7	0,9191	0,0809
F8	0,9183	0,0817
F9	0,9403	0,0597
F10	0,0000	1,0000
F11	0,9721	0,0279
F12	0,9746	0,0254
F13	0,7592	0,2408
F16	0,9293	0,0707
F18	0,9829	0,0171
F21	0,9741	0,0259
F24	0,9789	0,0211
F26	0,9834	0,0166
F27	0,9681	0,0319
F28	0,9532	0,0468

Number	x(CO_2)	x(CH_4)
F30	0,9696	0,0304
F32	0,9383	0,0617
F33	0,9696	0,0304
F35	0,9203	0,0797
F37	1,0000	0,0000
F38	0,9199	0,0801
F40	0,9526	0,0474

Tab. A 9:Microthermometry and Raman results of sample 85A-TUR1 (T_n= nucleation temperature; T_m= melting temperature; T_h= homogenization temperature; (x)= minor amounts)

Nr.	Type	T_m1	T_m2	T_h	[°C]	Water	Ice	Borate	Arsenolite	CO_2	CH_4	Chlathrate
F1	1	-7,7	22,3	374,3	20	x		(x)		(x)		
F2	2	-7,1	20,8	359,8	20	x		x		x	x	
					-100		x					x
					-50		x					x
					-30		x					x
					-20	x					x	
					-10	x					x	
F3	2	-7,9	16,4	376,4	20	x		x		x		
F4	2	-7,4	17,6	-	20	x		x		x	x	
					-100		x					x
					-150		x					x
					-30		x					x
					-10	x		x				x
					30	x				x	x	
F5	1	-7,5	15,8	381,8	20	x						
F6	2	-7,1	18,3	381,3	20	x		x	x	(x)		
					-150		x	x				
					-100		x	x				
					-50		x	x		(x)		
					-20	x		x				
					30	x		x	x			
F7	2	-9,0	24,9	379,8	20	x		x	x			
					-100		x					
					-50		x					
					-30		x					
					-20		x	x				
					-10	x		x				
					0	x		x				
					10	x		x				

Nr.	Type	T_m1	T_m2	T_h	[°C]	Water	Ice	Borate	Arsenolite	CO_2	CH_4	Chlathrate
F8	1	-6,6		377	20	x						
F9	1	-5,1	15,4	374,9	20	x				(x)		
F10	1	-7,6		376,4	20	x						
F11	2	-7,1	25,7	378,8	20	x		x		(x)		
F12	2	-7,2		377,6	20	x		x	x	x		
F13	1	-4,7		216,3	20	x				(x)		
F14	1	-7,2		250,9	20	x						
F15	2	-7,1	8,6	378,2	20	x		x				
F16	2	-7,0	22,0	377,4	20	x		x		(x)		
F17	2	-6,9	17,0	376,1	20	x		x				
F18		-6,6		376,7								
F19	1	-7,0		377,8	20	x				(x)		
F20		-8,1	4,3	356,7								
F21	2	-9,3		375,1	20	x		x		x		
F22	1	-8,1		375	20	x				x		
F23	1	-6,2		378,2	20	x						
F24	1	-6,5		286	20	x					x	
F25	1	-1,3		363,6	20	x				x		
					-150		x			x		x
					-50		x					x
					0	x				x		
F26	2	-6,4	25,8	379,1	20	x		x				
F27	2	-6,5	23,6	375,5	20	x		x			x	
F28	2	-6,2		378,6	20	x		x				
F29	1	-6,0		378,7	20	x		(x)		(x)		
F30	2	-6,3	25,3	379,9	20	x		x		x		
F31	1	-5,9		369,8	20	x						
F32	1	-6,1		369,9	20	x						
F33	1	-6,5		370,9	20	x						
F34	1	-5,1		370,4	20	x						
F35	1	-5,4		375,6	20	x						
F36	1	-2,8		359,8	20	x				x		
F37	1	-5,0		370,5	20	x				x		
F38	1	-9,3		373,4	20	x				x		
F39	1	-0,2		362,5	20	x				x		
F40	1	-0,4		365,9	20	x				x	x	
F41	1	0,2		361,5	20	x				x		

Tab. A 10: Composition of the studied fluid inclusions of sample 85A-TUR1

Number	x(CH_4)	x(CO_2)
F2	0,95	0,05
F3	0,00	1,00
F4	0,99	0,01
F9	0,00	1,00
F11	0,00	1,00
F12	0,00	1,00
F13	0,00	1,00
F16	0,00	1,00
F19	0,00	1,00
F21	0,00	1,00
F22	0,00	1,00
F24	1,00	0,00
F25	0,97	0,03
F27	1,00	0,00
F29	0,00	1,00
F30	0,01	0,99
F36	0,00	1,00
F37	0,00	1,00
F38	1,00	0,90
F39	0,00	1,00
F40	0,05	0,95
F41	0,01	0,99

Tab. A 11: Microprobe analyses of tourmaline in mass%

Analyses	F	Na_2O	CaO	FeO	K_2O	B_2O_3	MgO	SiO_2	TiO_2	Al_2O_3	MnO	Total
85aan1	0	1,481	0,139	9,813	0,037	10,144	1,966	35,77	0,456	36,599	0,149	96,554
85aan2	0	1,669	0,2	10,81	0,036	12,337	2,025	34,878	0,901	34,978	0,112	97,946
85aan4	0	1,716	0,164	11,035	0,031	11,951	1,732	34,699	0,685	35,399	0,174	97,586
85aan5	0	1,484	0,112	9,646	0,027	10,014	1,93	35,162	0,422	36,649	0,123	95,569
85aan6	0	1,358	0,072	9,631	0,033	11,063	1,927	35,517	0,269	35,582	0,131	95,583
85aan7	0	1,375	0,074	9,959	0,03	12,183	1,949	36,316	0,266	35,682	0,164	97,998
85aan8	0	1,774	0,209	10,997	0,038	12,568	1,896	33,574	0,741	35,496	0,186	97,479
85aan9	0	1,786	0,239	10,221	0,042	12,029	3,056	34,845	0,647	33,948	0,1	96,913
85aan10	0	1,414	0,057	9,808	0,024	12,075	1,899	35,195	0,335	34,789	0,167	95,763
85aan12	0	1,67	0,209	10,669	0,029	12,536	1,951	33,705	0,727	34,438	0,149	96,083
85aan13	0	1,714	0,194	11,232	0,035	9,786	1,955	34,362	0,815	34,69	0,138	94,921
85aan15	0	1,738	0,23	10,855	0,043	11,819	1,936	34,291	0,744	34,404	0,137	96,197
60aandark1	0	2,018	0,654	8,876	0,048	10,803	5,607	34,423	0,544	31,989	0,043	95,005
60aandark2	0	1,909	0,68	8,596	0,052	10,536	5,585	34,385	0,676	32,429	0,032	94,88
60aanbright4	0	1,886	0,409	8,675	0,044	12,174	5,077	34,402	0,439	32,939	0,066	96,111
25aan1	0	1,905	0,181	12,941	0,052	11,05	1,768	33,991	1,174	33,383	0,071	96,516
25aan2	0	1,849	0,148	13,283	0,046	10,572	1,144	34,426	0,812	34,277	0,153	96,71
25aan3	0	1,585	0,166	13,178	0,065	12,058	1,145	34,006	1,008	34,41	0,099	97,72
25aan5	0	1,986	0,197	13,16	0,052	11,228	1,599	33,599	0,632	33,535	0,103	96,091
25aan6	0	1,754	0,176	13,268	0,045	10,904	1,232	33,962	0,706	33,815	0,136	95,998
25aan7	0	1,892	0,199	12,805	0,04	10,668	1,884	33,75	0,978	33,994	0,078	96,288
25aan8	0	1,865	0,165	12,955	0,043	11,664	1,498	33,794	0,337	34,538	0,108	96,967
72can1	0	1,734	0,278	6,027	0,031	10,931	5,422	35,331	0,664	34,968	0,054	95,44
72can2	0	1,594	0,135	5,475	0,029	10,923	5,572	36,125	0,365	35,72	0,074	96,012
72can3	0	1,662	0,206	5,733	0,033	11,518	5,505	34,713	0,553	35,616	0,018	95,557
72can5	0	1,648	0,162	5,448	0,023	11,884	5,727	35,302	0,295	35,714	0,044	96,247
72can7	0	1,828	0,37	5,014	0,026	11,743	5,803	34,973	0,71	35,634	0,03	96,131
72can8	0	1,948	0,339	6,028	0,044	10,331	5,712	34,634	0,751	33,785	0,025	93,597
72can9	0	1,793	0,288	5,717	0,042	11,466	5,457	35,558	0,733	34,249	0,016	95,319
9can1	0	1,616	0,077	10,785	0,021	11,712	1,665	35,73	0,465	35,058	0,185	97,314
9can2	0	1,511	0,061	14,925	0,033	11,211	0,144	34,807	0,054	33,947	0,278	96,971
9can3	0	1,127	0,428	13,517	0,025	11,621	0,405	33,774	0,105	34,976	0,629	96,607
9can4	0	1,183	0,27	11,349	0,032	11,347	0,336	34,812	0,096	37,219	0,337	96,981
9can5	0	1,271	0,528	10,247	0,023	9,96	1,002	34,115	0,101	37,475	0,325	95,047
9can6	0	1,768	0,18	11,472	0,027	10,991	1,544	34,526	0,826	34,575	0,249	96,158
9can7	0	1,665	0,023	11,183	0,049	10,464	1,433	35,173	0,451	35,166	0,228	95,835
9can8	0	1,5	0,069	15,344	0,026	10,616	0,077	34,243	0,03	33,563	0,272	95,74
9can9	0	1,79	0,196	11,701	0,045	10,382	1,597	33,422	0,554	35,372	0,24	95,299
0aan1	0	1,587	0,154	11,265	0,045	9,847	1,329	34,447	0,36	35,673	0,24	94,947
0aan2	0	1,836	0,27	11,525	0,055	11,035	2,529	33,853	0,959	33,172	0,129	95,363
0aan3	0	1,946	0,299	9,815	0,048	11,444	4,018	34,426	0,783	32,388	0,05	95,217
0aan4	0	1,515	0,085	11,25	0,042	9,923	1,917	35,662	0,268	34,566	0,123	95,351
0aan6	0	1,868	0,236	11,471	0,058	11,274	2,534	34,087	0,87	33,477	0,124	95,999
0aan7	0	1,688	0,133	9,524	0,033	11,072	3,675	34,413	0,415	33,88	0,069	94,902
0aan10	0	1,895	0,354	11,667	0,054	9,944	2,403	33,424	1,012	34,044	0,148	94,945
0aan11	0	1,785	0,186	12,409	0,032	11,326	1,639	34,849	0,803	34,176	0,14	97,345
0aan12	0	1,916	0,171	12,299	0,042	12,384	1,907	33,608	0,906	33,467	0,156	96,856
0aan13	0	1,815	0,21	12,418	0,043	10,987	1,492	34,284	0,966	33,962	0,134	96,311
23fan2	0	1,687	0,055	13,841	0,024	10,37	0,585	33,472	0,776	34,66	0,11	95,58
23fan4	0	1,559	0,099	13,272	0,036	11,234	0,681	34,249	0,957	34,467	0,065	96,619
23fan5	0	1,306	0,049	13,029	0,028	10,185	0,683	34,973	0,746	35,439	0,065	96,503
23fan6	0	1,641	0,122	14,083	0,035	12,417	0,71	33,65	0,482	34,463	0,127	97,73

Analyses	F	Na_2O	CaO	FeO	K_2O	B_2O_3	MgO	SiO_2	TiO_2	Al_2O_3	MnO	Total
23fan7	0	1,547	0,156	12,499	0,044	10,069	0,603	34,403	1,237	35,242	0,053	95,853
23fan8	0	1,65	0,205	14,009	0,036	11,683	0,584	33,488	0,4	34,996	0,147	97,198
23fan9	0	1,299	0,027	13,234	0,038	9,687	0,409	34,419	0,363	35,186	0,091	94,753
23fan10	0	1,343	0,057	13,225	0,055	13,078	0,453	34,355	0,336	34,912	0,13	97,944
23fan11	0	1,286	0,01	12,993	0,027	11,157	0,433	35,105	0,362	35,277	0,04	96,69
23fan13	0	1,278	0	13,358	0,027	11,486	0,402	34,857	0,315	35,505	0,132	97,36
5ban1	0	1,955	0,103	13,291	0,03	11,573	0,916	33,273	0,765	32,792	0,525	95,223
5ban2	0	2	0,17	13,63	0,054	12,255	1,401	33,678	0,827	32,705	0,356	97,076
5ban3	0	1,858	0,107	12,403	0,052	10,12	0,539	33,969	0,719	34,01	0,897	94,674
5ban5	0	1,912	0,118	12,757	0,044	10,471	0,865	33,655	0,72	33,589	0,725	94,856
5ban6	0,848	2,236	0,82	1,387	0,027	11,729	0,051	34,8	0,415	37,984	5,236	95,176
5ban7	1,032	2,325	0,879	1,249	0,008	12,54	0	35,396	0,277	37,612	4,933	95,816
5ban8	0	2,039	0,118	13,323	0,046	11,159	0,932	34,266	0,661	33,172	0,615	96,331
5ban9	0	1,556	0,071	13,298	0,037	12,549	0,661	34,066	0,467	33,84	0,568	97,113
5ban12	0,984	2,152	0,845	1,253	0,02	10,089	0,073	35,102	0,372	38,107	5,084	93,667
5ban13	0,62	2,21	0,591	2,477	0,022	10,286	0,066	34,139	0,483	37,221	4,462	92,316
5ban14	0,783	1,656	1,343	0,572	0,019	12,124	0	35,025	0,18	40,66	1,712	93,744
5ban15	0,694	1,791	1,109	0,787	0,003	10,335	0,04	35,046	0,191	40,414	1,918	92,036
5ban16	0	1,391	0,033	12,739	0,031	11,483	0,564	34,557	0,249	34,591	0,691	96,329
5ban17	0	1,68	0,129	11,978	0,035	10,439	0,468	34,183	0,749	34,539	1,081	95,281
5ban18	0,481	2,207	0,348	5,128	0,021	12,414	0,162	35,807	0,489	36,924	3,175	96,953
TURan1	0	1,947	0,198	8,301	0,021	12,163	4,898	35,624	0,031	33,675	0,022	96,88
TURan2	0	1,852	0,177	8,448	0,036	10,67	4,808	36,106	0,002	33,16	0,048	95,307
TURan3	0	1,797	0,43	8,851	0,05	12,368	4,086	35,011	1,326	32,483	0,016	96,418
TURan4	0	1,909	0,447	8,505	0,025	12,779	4,556	35,169	1,199	32,639	0,002	97,23
TURan6	0	2,034	0,463	8,887	0,038	12,114	4,569	34,365	1,216	33,308	0,007	97,001
TURan7	0	1,827	1,29	11,482	0,031	12,467	4,607	34,147	0,903	30,476	0	97,23
TURan8	0	1,739	1,995	2,045	0,027	11,586	10,165	36,202	0,558	31,497	0,007	95,821
TURan9	0	1,688	2,385	1,934	0,038	13,487	10,506	36,079	0,666	31,095	0	97,878
TURan10	0	1,781	1,714	2,137	0,036	12,003	9,893	36,148	0,699	31,899	0	96,31
TURan11	0	1,837	1,554	1,725	0,021	11,799	10,045	36,831	0,354	31,575	0	95,741
TURan12	0	1,495	0,123	10,149	0,023	12,897	2,976	35,249	0,485	34,568	0,031	97,996
TURan14	0	1,857	0,503	15,969	0,036	11,443	1,006	34,16	0,693	30,743	0,058	96,468
TURan15	0	1,879	0,427	15,644	0,041	11,955	0,885	33,88	0,745	31,45	0,075	96,981
TURan16	0	1,353	3,126	2,18	0,043	13,606	10,891	35,144	1,531	29,589	0,008	97,471
TURan17	0	1,94	1,108	2,033	0,015	12,371	9,546	35,797	0,565	32,117	0,006	95,498
TURan18	0	1,103	3,473	2,42	0,03	11,706	11,09	36,008	1,649	28,504	0,014	95,997
TURan19	0	1,804	1,874	2,543	0,023	11,357	9,632	35,847	0,642	31,761	0	95,483
35ban1	0	1,458	0,013	13,317	0,033	11,219	0,769	35,257	0,355	34,358	0,16	96,939
35ban2	0	1,746	0,154	13,935	0,074	11,708	0,883	34,143	0,529	33,534	0,15	96,856
35ban4	0	1,244	0,007	13,017	0,018	10,06	0,493	34,767	0,321	34,815	0,149	94,891
35ban5	0	1,431	0,016	13,129	0,045	9,379	0,533	35,527	0,331	34,841	0,128	95,36
35ban8	0	1,67	0,126	13,39	0,041	11,804	0,823	34,543	0,813	33,622	0,115	96,947
35ban9	0	1,646	0,092	13,445	0,046	12,214	0,775	34,683	0,812	33,747	0,109	97,569
35ban10	0	1,688	0,099	13,195	0,035	11,299	0,771	34,356	0,867	33,688	0,116	96,114
35ban12	0	1,62	0,064	13,52	0,044	9,311	0,693	34,486	0,851	33,961	0,162	94,712
35ban13	0	1,348	0,022	12,992	0,022	8,907	0,561	36,066	0,324	35,44	0,153	95,835
35ban14	0	1,334	0,01	12,918	0,036	9,589	0,586	36,099	0,325	35,374	0,13	96,401
35ban15	0	1,754	0,098	13,745	0,058	11,387	0,636	33,908	0,796	34,74	0,162	97,284
35ban16	0	1,609	0,102	13,857	0,045	12,058	0,718	34,787	0,693	33,612	0,146	97,627
35ban17	0	1,586	0,047	13,074	0,035	10,659	0,756	35,33	0,752	34,074	0,126	96,439
59ban3	0	2,176	0,345	4,829	0,038	11,022	7,33	36,684	0,134	33,07	0,057	95,685

Analyses	F	Na_2O	CaO	FeO	K_2O	B_2O_3	MgO	SiO_2	TiO_2	Al_2O_3	MnO	Total
59ban4	0	2,222	0,301	3,217	0,031	9,11	8,116	37,318	0,074	33,989	0,073	94,451
59ban5	0,126	2,495	0,141	2,51	0,033	12,603	9,398	37,28	0,058	32,639	0,038	97,268
59ban6	0	2,08	0,772	4,967	0,045	12,421	8,076	36,498	0,105	32,705	0,031	97,7
59ban7	0	2,329	0,147	3,633	0,029	10,89	8,15	37,322	0,077	33,51	0,038	96,125
59ban8	0	2,194	0,056	2,961	0,016	12,548	8,134	37,142	0,115	33,528	0,064	96,758
59ban9	0	2,376	0,26	3,613	0,039	12,171	8,512	36,643	0,065	32,81	0,083	96,572
59ban10	0,151	2,283	0,273	3,357	0,04	9,249	8,778	37,132	0,012	32,775	0,071	94,057
75dan2	0	1,918	1,021	10,38	0,063	10,025	4,732	35,779	1,445	31,398	0,104	96,865
75dan3	0	2,084	0,899	11,053	0,042	9,868	4,632	35,462	1,693	31,027	0,127	96,887
75dan5	0	1,992	1,062	10,895	0,066	10,57	4,771	35,507	1,714	30,714	0,094	97,385
3aan2	0	1,791	1,071	15,664	0,055	9,843	1,875	35,103	0,495	29,551	0,035	95,483
3aan3	0	1,528	0,367	14,724	0,022	8,619	1,011	35,54	0,122	33,619	0,144	95,696
3aan4	0	1,649	0,189	12,769	0,04	8,918	1,022	35,316	1,003	34,434	0,129	95,469
3aan5	0	1,654	0,21	12,618	0,033	10,093	1,14	35,189	0,906	34,437	0,085	96,365
3aan6	0	1,851	0,199	12,985	0,033	10,008	1,036	34,696	0,753	34,275	0,324	96,16
3aan8	0	1,168	0,024	10,174	0,014	9,431	2,48	36,587	0,087	34,514	0,052	94,531
29dan1	0	1,441	2,55	4,598	0,046	11,363	9,518	36,024	2,665	28,361	0	96,566
29dan2	0	1,545	1,773	4,105	0,037	9,236	8,652	36,824	1,574	31,77	0	95,516
29dan3	0	1,612	1,225	2,43	0,03	10,764	9,047	37,7	0,438	32,73	0,035	96,011
29dan4	0	1,595	1,47	2,469	0,019	11,298	9,175	37,298	0,698	32,412	0	96,434
29dan5	0	1,697	1,506	2,151	0,03	10,656	9,54	37,514	0,493	32,661	0	96,248
29dan6	0	1,715	1,373	1,866	0,025	12,317	9,619	37,446	0,353	32,86	0,03	97,604
29dan8	0	1,554	1,846	2,347	0,035	11,586	9,74	37,415	1,052	31,583	0,004	97,162
29dan10	0	1,461	2,497	2,357	0,03	11,771	10,435	36,735	0,832	30,1	0	96,218
65can1	0	1,967	0,416	13,803	0,047	11,545	1,815	35,422	0,42	32,627	0,432	98,494
65can2	0	1,884	0,382	12,912	0,061	10,998	1,742	35,604	0,395	33,599	0,381	97,958
65can6	0	1,5	0,135	13,075	0,024	10,893	1,301	35,921	0,106	34,242	0,395	97,592
65can8	0	1,835	0,179	12,775	0,038	11,568	1,484	35,403	0,507	33,494	0,502	97,785
65can9	0	2,014	0,326	12,984	0,054	11,074	1,815	34,987	0,961	32,969	0,511	97,695
65can10	0	1,959	0,319	13,154	0,04	10,867	1,589	35,333	0,887	32,619	0,528	97,295

Tab. A 12: Microprobe analyses of garnet in mass%

Analyses	MgO	Na_2O	FeO	CaO	Cr_2O_3	Al_2O_3	SiO_2	TiO_2	MnO	Total
57aan1	0,786	0,022	34,598	0,356	0	20,543	37,508	0	7,603	101,421
57aan2	0,625	0,01	30,785	0,548	0,009	20,045	36,073	0,08	8,888	97,078
57aan3	0,627	0,003	33,618	0,482	0,024	20,799	36,935	0,004	8,528	101,022
57aan4	0,755	0,062	32,905	0,533	0	20,392	36,827	0,057	7,893	99,439
57aan5	0,829	0,027	32,368	0,54	0	20,4	36,682	0,037	7,654	98,55
57aan6	0,754	0,069	35,044	0,434	0,026	20,75	36,921	0	7,309	101,309
57aan7	0,604	0,007	33,116	0,462	0,006	20,509	37,413	0,035	9,044	101,215
57aC2an4	0,688	0,065	32,516	0,361	0	20,619	37,618	0	7,995	99,868
57aC2an5	0,779	0,029	33,54	0,373	0	20,523	36,406	0,037	7,674	99,363
57aC2an6	0,795	0,02	33,236	0,437	0,035	20,652	37,326	0,045	8,002	100,567
57aC2an7	0,809	0,037	34,348	0,45	0	20,453	36,486	0	7,868	100,451
57aC2an8	0,76	0,032	31,916	0,423	0,009	20,525	36,739	0	7,95	98,354
57aC2an9	0,774	0,013	31,46	0,422	0,004	20,368	36,65	0,016	8,04	97,748
57aC2an10	0,674	0,018	31,416	0,385	0,01	20,583	36,013	0,008	8,831	97,938

Analyses	MgO	Na_2O	FeO	CaO	Cr_2O_3	Al_2O_3	SiO_2	TiO_2	MnO	Total
57aC2an12	0,671	0	32,879	0,395	0	20,642	36,294	0	8,762	99,676
57aC2an14	0,683	0	30,954	0,366	0	20,403	37,182	0	8,714	98,307
57aC2an16	0,59	0,015	31,966	0,388	0,016	20,632	36,657	0,014	9,461	99,748
57aC2an18	0,801	0,042	36,295	0,359	0	20,616	36,969	0,01	7,714	102,806
57aC2an19	0,852	0	34,879	0,387	0,02	20,966	37,217	0	7,641	101,962
57aC2an20	0,813	0,034	34,216	0,296	0,05	20,469	36,676	0,016	7,808	100,411
57aC2an21	0,823	0,034	33,488	0,792	0	20,334	36,558	0,055	8,285	100,369
57aC2an22	0,694	0,047	32,177	0,593	0,006	20,323	37,198	0,01	8,621	99,669
57aC2an23	0,76	0,003	33,589	0,747	0	20,44	37,131	0,018	8,202	100,893
57aC2an24	0,638	0,015	33,942	0,414	0,018	20,478	36,877	0	8,519	100,904
57aC2an26	0,724	0,015	32,23	0,514	0,01	20,226	37,401	0,037	8,393	99,55
57aC2an28	0,743	0,045	30,231	0,538	0	20,086	36,749	0,033	8,468	96,903
57aC2an30	0,65	0,008	32,517	0,405	0,013	20,934	36,343	0,014	8,995	99,89
57aC2an31	0,659	0,013	31,435	0,431	0	20,515	35,859	0,016	9,107	98,049
57aC2an34	0,705	0,069	32,813	0,513	0,003	20,472	36,468	0,014	8,489	99,554
57aC2an35	0,7	0	32,435	0,306	0	20,558	35,794	0,006	8,604	98,403
57aC2an36	0,768	0,02	33,002	0,377	0	20,633	36,009	0	7,805	98,631

Tab. A 13: Microprobe analyses of biotite in mass%

Analyses	MgO	Na_2O	FeO	CaO	Al_2O_3	SiO_2	TiO_2	K_2O	MnO	Total	H_2O
57aan8	3,052	0,087	26,976	0,003	18,81	34,098	1,999	8,17	0,539	93,734	3,748
57aan11	2,652	0,072	25,963	0,024	18,678	33,644	2,641	9,277	0,432	93,4	3,714
57aan12	2,824	0,102	22,729	0,001	19,433	34,222	1,906	9,26	0,382	90,866	3,683
57aan13	2,906	0,097	24,011	0,044	18,925	34,871	1,895	8,742	0,432	91,932	3,721
57aC2an1	3,286	0,191	24,36	0,011	19,559	34,821	1,888	9,152	0,384	93,653	3,779
57aC2an3	2,922	0,103	25,102	0,012	20,462	35,537	2,185	9,039	0,345	95,711	3,872
57aC2an11	2,987	0,061	22,437	0	19,763	34,952	1,915	9,474	0,351	91,953	3,743
57aC2an13	2,956	0,049	25,502	0	19,685	34,708	2,129	9,512	0,312	94,894	3,804
57aC2an15	3,143	0,076	25,412	0	20,254	34,535	2,112	9,483	0,361	95,392	3,827
57aC2an17	3,191	0,044	25,366	0	19,395	34,877	2,235	9,644	0,369	95,121	3,812
57aC2an25	3,093	0,065	24,287	0	19,582	34,45	2,23	9,617	0,321	93,645	3,768
57aC2an27	3,065	0,091	24,909	0	20,172	34,645	2,151	9,129	0,373	94,535	3,810
57aC2an32	3,04	0,092	26,428	0	19,73	34,348	1,89	9,038	0,425	94,991	3,795
57aC2an33	3,182	0,16	26,089	0,057	18,926	33,131	1,978	7,481	0,417	91,421	3,669
65can1	3,894	0,206	22,797	0	18,14	33,932	3,298	9,032	1,25	92,549	3,727
65can2	4,12	0,156	24,102	0	18,298	33,86	3,301	9,255	1,293	94,385	3,774
65can3	4,083	0,092	25,163	0	18,374	33,126	3,338	8,932	1,383	94,504	3,757
65can4	3,757	0,126	23,713	0	18,617	34,028	3,283	9,293	1,289	94,11	3,773
65can5	3,728	0,077	24,128	0	18,85	34,284	3,329	9,456	1,268	95,121	3,810

Tab. A 14: Microprobe analyses of andalusite in mass%

Analyses	Na_2O	CaO	FeO	K_2O	MgO	SiO_2	TiO_2	Al_2O_3	MnO	Total
35b2an1	0,013	0	0,212	0,01	0	37,181	0,031	62,996	0,013	100,456
35b2anpink2	0,009	0,004	0,27	0	0	37,41	0	62,579	0	100,272
35b2anpink3	0,006	0,006	0,348	0,011	0	37,073	0,055	62,53	0,019	100,048
35b2anpink4	0,014	0	0,368	0	0	37,124	0,079	62,607	0,009	100,201
35b2anpink5	0,017	0	0,441	0,008	0	38,04	0,127	62,844	0,001	101,478
35b2anpink6	0,021	0,008	0,619	0	0,003	37,585	0,13	62,244	0	100,61
35b2anwhite1	0,015	0	0,203	0,008	0	37,417	0,089	62,728	0,002	100,462
35b2anwhite2	0,007	0	0,211	0,003	0,01	37,215	0,06	63,142	0,008	100,656
35b2anwhite3	0,014	0,018	0,268	0,008	0	37,269	0,048	62,853	0	100,478
35b2anwhite4	0,015	0	0,197	0	0,005	37,429	0,029	63,021	0,002	100,698
35b2anwhite5	0,017	0,013	0,243	0,01	0,01	37,244	0,034	62,766	0,009	100,346
72cpinkan1	0	0	2,297	0,01	0,018	37,238	0,06	60,493	0	100,116
72cpinkan2	0	0	2,639	0,008	0,036	37,313	0,115	60,483	0	100,594
72cpinkan3	0,017	0,001	2,574	0,002	0,027	37,154	0,096	60,372	0,008	100,251
72cwhitean4	0,017	0,025	0,596	0,007	0,046	38,001	0	62,078	0,005	100,775
72cwhitean5	0,005	0	1,024	0	0,039	37,678	0	61,97	0	100,716
72cwhitean6	0,002	0,011	1,061	0	0,027	37,209	0,072	62,072	0,004	100,458
72cpinkan7	0,003	0,008	2,965	0,004	0,002	37,449	0,067	59,433	0	99,931
72cpinkan8	0,001	0	1,792	0,007	0,001	37,416	0,07	59,488	0,017	98,792
72cwhite9	0	0,008	1,023	0,002	0,032	36,683	0,002	60,168	0,008	97,926
72cwhite10	0	0	1,457	0,004	0,017	36,532	0,014	59,877	0	97,901
64apinkan1	0,014	0,003	1,158	0	0,062	36,364	0,285	62,227	0,019	100,132
64apinkan2	0,004	0,03	1,462	0,004	0,073	37,078	0,246	61,953	0,005	100,855
64awhite3	0,022	0,023	0,54	0,002	0	35,864	0,062	62,971	0,003	99,487
64awhite4	0,004	0,003	0,659	0	0,034	36,444	0,036	62,579	0	99,759
67epinkan1	0,019	0,019	1,981	0,012	0,041	36,546	0,065	60,857	0	99,54
67epinkan2	0,009	0,024	2,677	0,002	0,035	36,688	0,034	60,492	0,006	99,967
67ewhitean3	0	0,003	1,769	0,022	0,03	36,107	0,038	61,507	0	99,476
67ewhitean4	0	0	1,891	0,008	0,026	36,25	0,038	61,553	0	99,766
67ewhitean5	0,029	0,001	1,835	0,007	0,038	36,311	0,079	61,505	0,001	99,806
67epinkan6	0,02	0	2,657	0,005	0,046	36,159	0,101	60,875	0	99,863
67epinkan7	0,001	0,002	2,023	0,015	0,027	36,332	0,079	61,241	0,015	99,735
67epinkan8	0,008	0,007	2,252	0,002	0,045	36,844	0,108	61,183	0	100,449
25apinkan1	0	0	0,649	0,004	0,027	36,295	0,096	61,388	0	98,459
25apinkan2	0,028	0,009	0,646	0,015	0,045	36,15	0,063	62,785	0	99,741
25apinkan3	0,023	0	2,021	0,106	0,022	35,413	0,07	60,571	0,014	98,24
25awhitean4	0,028	0	0,217	0,005	0	36,343	0,046	63,302	0,013	99,954
25awhitean5	0,011	0,009	0,162	0,005	0	37,155	0,08	62,806	0	100,228
25awhitean6	0	0,014	0,201	0,011	0	36,812	0	63,092	0,021	100,151
60apinkan1	0,069	0,002	2,365	0,02	0,055	35,571	0,175	60,933	0,039	99,229
60apinkan2	0,003	0,008	2,721	0,014	0,105	35,535	0,182	60,968	0	99,536
60apinkan3	0,006	0	2,305	0,004	0,048	35,315	0,184	61,033	0	98,895
60awhitean4	0	0	1,713	0	0,024	36,259	0,017	61,019	0,002	99,034
60awhitean5	0,005	0	1,618	0	0,009	35,51	0,074	61,734	0,02	98,97
60awhitean6	0,002	0	1,545	0,002	0,025	36,268	0,007	61,508	0,016	99,373
60aan7	0	0	2,392	0,004	0,049	36,03	0,192	60,909	0,021	99,597
60aan8	0,009	0	2,392	0,001	0,055	35,651	0,115	60,985	0	99,208
60awhitean9	0	0,007	1,79	0,001	0,026	35,191	0,091	60,975	0	98,081
60apinkan10	0	0,018	2,878	0,003	0,069	35,479	0,155	59,235	0	97,837
60awhitean11	0,015	0	1,726	0,001	0,014	35,878	0,151	61,773	0,004	99,562

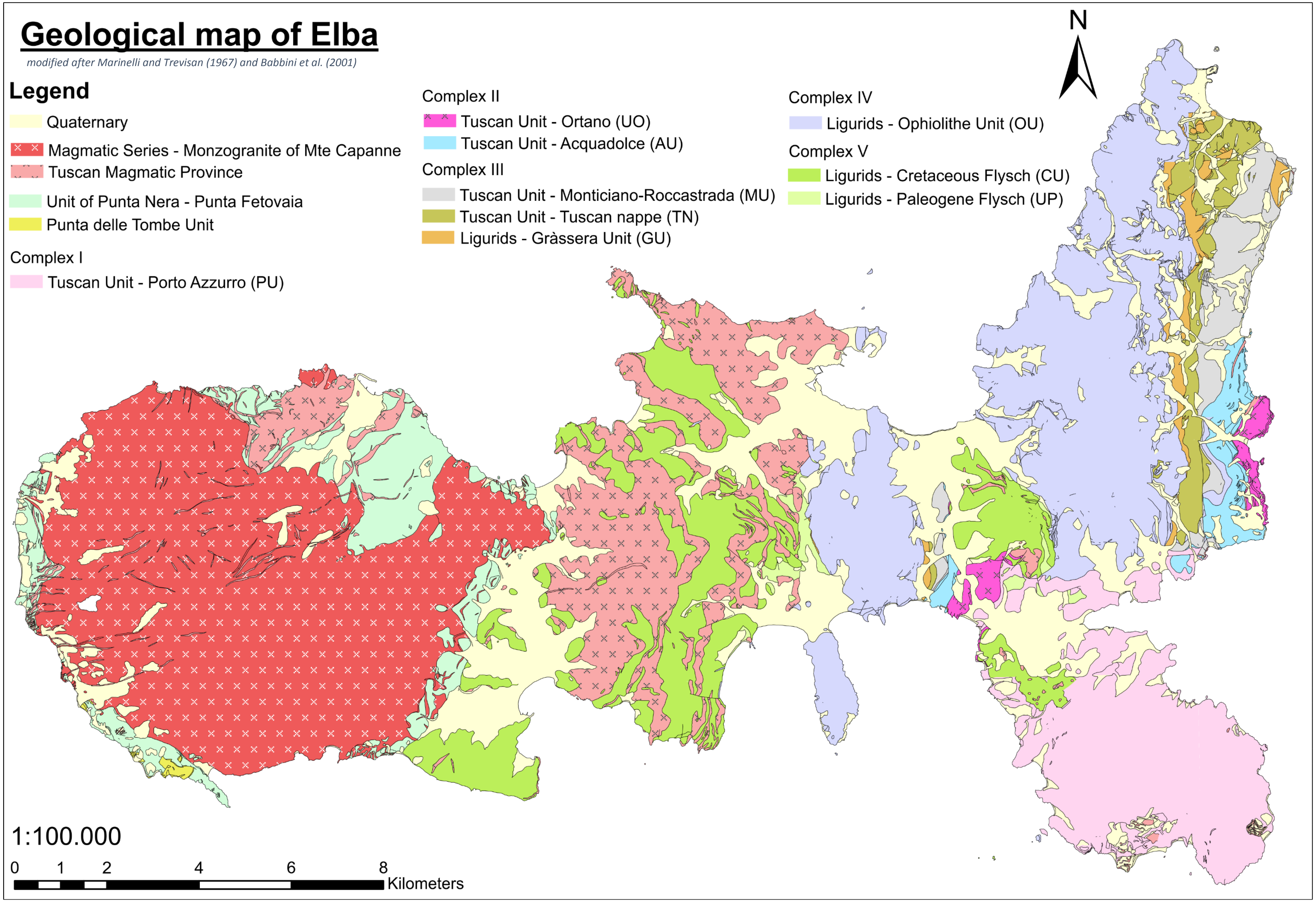

Geological map of Elba

modified after Marinelli and Trevisan (1967) and Babbini et al. (2001)